Photoluminescence of ZnO: Radioactive ion-implantation and transition metal defects

A thesis submitted to

Dublin City University

for the degree of

Doctor of Philosophy

by

Deirdre McCabe (B.Sc.)

Research Supervisor
Professor Martin Henry
School of Physical Sciences

January 2007

Declaration

I hereby certify that this material, which I now submit for assessment on the programme of study leading to the award of Doctor of Philosophy is entirely my own work and has not been taken from the work of others save and to the extent that such work has been cited and acknowledged within the text of my work.

Signed: Deirdre McCabe ID No.: 98072471

Date: 31/01/2007

Acknowledgements

I would like to thank my supervisor, Professor Martin Henry, for his support, patience and guidance. He was always available to answer questions, to discuss results, to offer advice, and to help in the lab throughout the project.

I would also like to thank Dr. Enda McGlynn for all his useful advice, and the other members of the SSL group - Brendan, Sarah, Ger, Justyna, Alan and Conor.

Without the help of Dr. Karl Johnston many of the experiments would not have been a success, and I thank him for the many hours devoted to radioactive implantations and data-taking. I must, of course, also acknowledge the Solid State Coordinators at CERN, Drs. Marc Dietrich and Thomas Agne, for ensuring the smooth running of these experiments.

I would like to express my appreciation of the efforts of the technical staff in the DCU physics department, particularly Alan Hughes, Victor Fagg, Des Lavelle and Pat Wogan for all their assistance. Thanks to all the staff and postgraduate students for the many good memories I shall have of my time here.

Special thanks should go to my parents and family for all their support, and to James for his encouragement and advice through the years.

Finally, I would like to acknowledge financial support from the Embark Initiative Postgraduate Research Scholarship Scheme (2002) under the Irish Research Council for Science, Engineering and Technology (IRCSET), funded by the National Development Plan.

Table of Contents

Title Page		**i**
Declaration		**ii**
Acknowledgements		**iii**
Table of Contents		**iv**
Abstract		**vii**
List of Abbreviations		**viii**
Chapter 1	**Introduction**	**1**
1.1	*Overview of ZnO*	1
1.2	*Doping techniques*	4
	1.2.1 Ion implantation	4
	1.2.2 Ion implantation in ZnO	5
1.3	*Radioactive ion implantation*	7
	1.3.1 Introduction to radioactive ion implantation	7
	1.3.2 Recoil energy	9
1.4	*Layout of thesis*	10
	References	11
Chapter 2	**Experimental Procedure**	**14**
2.1	*Photoluminescence*	14
2 2	*Experimental Apparatus*	16
	2.2.1 Dispersive system at DCU	16
	2.2.2 Fourier Transform System at DCU	19
	2.2.3 Dispersive System at CERN	20
2.3	*Photoluminescence of ZnO*	21
2.4	*Temperature Dependence*	23
	2.4.1 Change in intensity as a function of temperature	23
	2.4.2 Transitions between two excited states to a common ground state model	25
	2.4.3 Change in FWHM and energy positions of spectral	26

	features with temperature	
2.5	*Conclusions*	27
	References	28
Chapter 3	**Study of the optical properties of Ga in ZnO**	**29**
3.1	*Introduction*	29
3.2	*Experimental Description*	31
3.3	*Results*	32
	3.3.1 Implantation and Annealing Conditions	32
	3.3.2 Control Experiments	35
	3.3.3 Radioactive implantations	39
3.4	*Conclusions*	53
	References	54
Chapter 4	**Study of the green band in ZnO**	**56**
4.1	*Introduction*	56
4 2	*Experiment Description*	59
4 3	*Results*	60
	4.3.1 Implantation of ^{65}Ni	60
	4.3.2 Cu implantations	62
4.4	*Discussion*	63
4.5	*Conclusions*	68
	References	68
Chapter 5	**Study of signals in the near IR and Red region in the PL of ZnO**	**70**
5.1	*Introduction*	70
5.2	*Absorption features*	71
5.3	*Infra-red emission*	79
	5.3.1 Temperature dependence of L_1 lines	86
	5.3.2 Temperature dependence of A_1 lines	101
5.4	*Conclusions*	106
	References	107

Chapter 6	**Photoluminescence Experiment on the IR signals in ZnO**	**108**
6.1	*Introduction*	108
6.2	*Experiment Description*	109
6.3	*Results*	112
	6.3.1 Photoluminescence measurements	112
	6.3.2 Photoluminescence Excitation Measurements	113
	6.3.3 Phase Sensitive Detection Measurements	116
	6.3.4 Modelling the Fe^{3+} emission	122
	6.3.5 PLE of the L_i features	125
6 4	*Conclusions*	130
	References	131
Chapter 7	**Damage-related emission lines in ^{107}Cd- and ^{7}Be-implanted samples**	**132**
7.1	*Introduction*	132
7.2	*Experimental Description*	134
7.3	*Results*	134
	7.3.1 Damage-related emission lines	134
	7.3.2 Acceptor (donor) pair analysis	137
7.4	*Conclusions*	142
	References	143
Chapter 8	**Conclusions and Further Work**	**144**
8.1	*Conclusions*	144
8 2	*Further Work*	145
Appendix A	Measurement of laser heating	A1

Abstract

In this thesis, implantation of radioactive isotopes and photoluminescence studies were used to identify defects in ZnO. Implantations of stable and radioactive isotopes of gallium and zinc were performed. From photoluminescence studies of these samples, a feature at 3.3600 eV was shown to be due to recombination at a Ga donor site, while a feature at 3.3225 eV was shown to follow the concentration of the daughter product Ge. A broad red band was found to grow in samples implanted with ^{72}Zn. This is believed to be a damage related band, created by the high recoil energy of the ^{72}Ge daughter product.

Radioactive isotopes of Cu and Ni, with Cu as a decay product, were implanted into single-crystal ZnO in order to investigate the relationship between Cu and the structured green band, a common feature seen in photoluminescence spectra of ZnO. As the intensity of the green band was found to increase with the half-lives of the Cu and Ni isotopes, no correlation could be obtained between the Cu concentration in the samples and the green band. An explanation for these results was found to lie with the high recoil energy of the daughter products of the implanted isotopes, and the green band was attributed to the creation of Zn-vacancies.

The temperature dependence of new signals observed in the near IR was examined. These signals were also studied using photoluminescence excitation measurements. Attempts to decipher the excited states of the new emission features were made through manual subtraction of the contributions of the Fe^{3+} phonon replicas, and also examination of the PL intensities at various excitation energies. A possible model for the excitation mechanism of the previously reported Fe^{3+} emission is presented.

List of Abbreviations

DAP	Donor Acceptor Pair
DX	Donor Bound Exciton
EPR	Electron Paramagnetic Resonance
FT	Fourier Transform
FWHM	Full Width at Half Maximum intensity
ISOLDE	Isotope Separator On-Line
LIA	Lock in amplifier
MBE	Molecular Beam Epitaxy
PL	Photoluminescence
PLD	Pulsed Laser Deposition
PLE	Photoluminescence Excitation
PMT	Photomultiplier Tube
PSD	Phase Sensitive Detection
SVP	Seeded Vapour Phase
TES	Two Electron Satellite
ZPL	Zero Phonon Line

Chapter 1: Introduction

1.1 Overview of ZnO

ZnO is a II-VI semiconductor that has been widely studied over the past seventy years [1, 2]. The level of interest in this material has varied considerably over this period with much work being carried out in the period 1950-1980 [3-6], after which research in this material lessened somewhat. According to Klingshirn *et al.* [7], this was partly due to the lack of progress in dealing with the difficulty of producing p-type material and was also related to increased interest in other research fields such as low-dimensional structures. At the present time, on average over sixty papers on ZnO are published each week, with the present focus being principally on nanostructures [8].

ZnO crystallizes in a wurtzite structure with each Zn atom surrounded by four O atoms. It has attracted renewed interest due to the refinement of growth techniques which have led to the production of high quality, large-area substrates. The wide band-gap energy of ~3.4 eV along with a high exciton binding energy of 60 meV, makes it an ideal candidate for short wavelength optoelectronic devices. Before such devices can be manufactured, a greater knowledge of the defect physics of this material is needed.

One of the barriers to the use of this material for optoelectronic devices is the difficulty in reproducibly doping ZnO to produce p-type material. As-grown ZnO is found to be always n-type. This was long believed to be due to intrinsic defects such as O-vacancies and Zn-interstitials. The study of intrinsic defects in ZnO has been for the most part theoretical rather than experimental in nature [9-13], but significant differences have been reported between calculated energies in the band-gap and formation energies of particular defects. This is largely due to the under-estimation of the band-gap provided by theoretical means, thence leading to different values for formation energies and energy levels within the band-gap. In general, however, Zn- and O-vacancies have been shown to be deep acceptors and donors, respectively, and therefore not the source of the usual n-type conductivity. A recent paper by Janotti *et al.* [9] reported that O-vacancies, in n-type material, have a low formation energy but

were deep donors, while Zn-interstitials, though shallow, have a high formation energy, thus are unlikely to be present at high concentrations. In p-type material, both the O-vacancy and the Zn-interstitial were found to have low formation energies, so it is possible that they can compensate for acceptors in such material. O-interstitials, with a high formation energy, and Zn-vacancies, with a low formation energy, have been shown to be deep acceptors.

Positron annihilation experiments performed by Tuomisto *et al.* [13] have shown that the Zn-vacancy was present at concentrations of 2×10^{15} cm^{-3} in as-grown material obtained from Eagle-Pitcher Technologies in comparison to a total acceptor concentration, as measured through Hall Effect measurements, of 5×10^{15} cm^{-3}. Better agreement was obtained between the two measurements when the Hall data was fit to a double acceptor, leading to an acceptor concentration of $\sim 1.7 \times 10^{15}$ cm^{-3}. Both the O- and the Zn-vacancy have also been attributed to the green photoluminescence (PL) band in ZnO. This will be discussed further in Chapter 4.

Hydrogen has been shown to be an important contributor to the conductivity of the material. Theoretical studies by Van de Walle [14] first showed that it should act as a shallow donor. This was a surprising result as hydrogen in semiconductors normally acts to counteract the prevalent conductivity, acting as an acceptor in n-type material and a donor in p-type material. Experimental proof soon revealed that doping with hydrogen increases the number of conduction electrons, and that the concentration of H could be correlated with a neutral bound exciton feature in PL spectra and one of the main donor levels observed in Hall Effect measurements [15, 16]. Look *et al.* [17] pointed out that although the concentration of H could be correlated to a shallow donor in ZnO, the D1 level in Hall effect measurements and the I_4 PL signal, it was not the principal donor in this material as a deeper level, D2, with a binding energy of 60-70 meV had a greater impact on the room temperature carrier concentration. Other known donors in ZnO are Group III metals, such as Al and In when situated on a Zn site or Group VII elements, such as F, on an O-site. In contrast with the wide variety of donor impurities, there has been little progress regarding the identification of shallow impurities until recently. In the past couple of years, however, some progress has been made towards achieving p-type material.

In theory, doping with Group I or Group V elements should result in p-type material if they occupy Zn and O lattice sites, respectively. One of the problems with this is that Group V elements tend to have a low solid solubility in ZnO and doping with Group I elements leads to the formation of self-compensating defects. Dopants such as N and As have been shown to be fairly deep acceptors while elements such as Li, though shallow, tend to prefer interstitials sites, thus compensating any acceptor behaviour [18]. The first report of successful p-type doping was reported by Minegishi *et al.* [19] and was achieved through doping with NH_3. Doping using N resulted in p-type material with low hole concentration and hole mobility [20]. Theoretical calculations performed by Yamamoto [21] first indicated a way to overcome this problem. It was found that using a co-doping technique, i.e. doping with both gallium (a donor) and nitrogen (an acceptor), would increase the solid solubility of N in ZnO, thus rendering the material p-type. Joseph *et al.* [20] found that exposing films to an N_2O gas during pulsed laser deposition (PLD) growth produced p-type films of high resistivity and low carrier concentration, while doping with both gallium and nitrogen produced p-type films with low resitivity with a carrier concentration of 4×10^{19} cm^{-3}. There have also been reports of p-type doping with other Group V elements such as P [22], As [23] and Sb [24]. The large difference in atomic radius of As and Sb compared to the Zn-O bond length means that p-type doping is believed to be due to a complex with these dopants rather than a simple substitutional process [25].

Significant progress has been made on the understanding of the behaviour of defects in ZnO in recent years; in particular the successful production of p-type material has reawakened interest in this material. Yet, there still remains a lot to be learnt before the production of useful devices can become a reality. The diffusion behaviour of many of the most common dopants remains to be investigated, while the annealing treatment necessary to recover implantation damage is known for only a handful of the most common dopants. In the PL spectra of ZnO, only four of the fifteen most commonly seen bound exciton lines have been identified [26]. Normally, it is possible to base chemical identification on controlled diffusion and/or implantation of selected impurities and spectroscopic analysis. For ZnO, however, the quality and purity of the available crystals are not suitable for this approach. Instead, a study of the use of radioactive isotopes was undertaken. In this thesis, several radioactive

isotopes were implanted into ZnO, focusing on elements that could be potential donors and acceptors.

1.2 Doping techniques

1.2.1 Ion implantation

Ion implantation is a well-established technique for introducing defects in semiconductors [27]. The implanted dose can be very much greater than the chemical solubility limit of the desired dopant, and implantation can be performed at room temperature (or below), rather than the high temperatures required for diffusion doping. The distribution profile can also be controlled to a high degree and can be modelled in an ideal case as a Gaussian distribution with an average projected range of R_p and a standard distribution of ΔR_p. Different profiles can be obtained by performing a series of implantations at different energies. Figure 1 (a) shows the simulated implantation profile of ^{7}Be with an implantation energy of 60 keV, while Fig. 1 (b) shows the profile obtained using a series of implantation energies. These profiles were obtained using SRIM 2003 [28]. Experiments show that a simple Gaussian profile is not usually the case [27]; implantation profiles of light atoms are skewed towards the surface, while implantation profiles of heavy ions are skewed towards the bulk. This is because the range of light atoms is mostly controlled by electronic stopping; the ion loses kinetic energy to electrons of the target material. On the other hand, the range of heavy atoms is mostly limited by collisions with atoms of the target material.

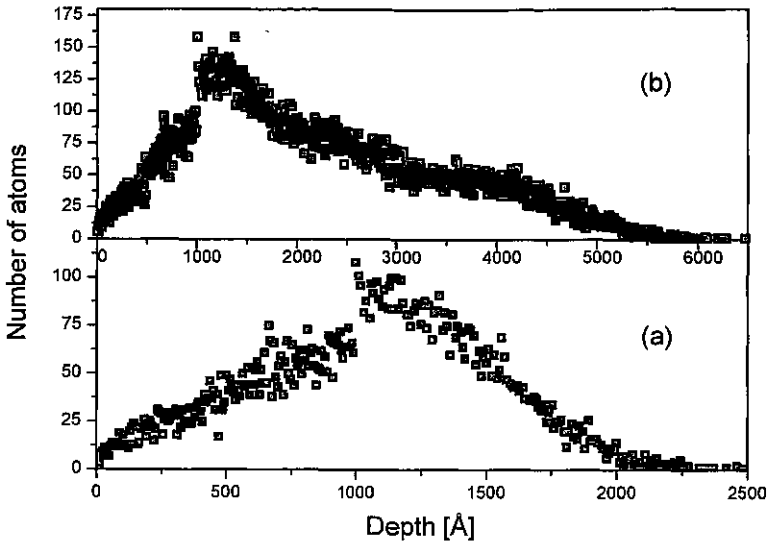

Figure 1.1. *(a) Concentration profile of implanted atoms with an implantation energy of 60 keV; (b) concentration profile with implantation energies 30, 60 and 120 keV*

The process of implantation creates damage in the crystal which must be recovered using a high temperature anneal. After implantation, the implanted isotopes are located very close to the semiconductor surface and are not generally located on normal lattice sites. The anneal process helps to move these atoms into lattice sites so that they become electrically/optically active and also helps to diffuse the implanted atoms from the implanted, near surface layer.

1.2.2 Implantation in ZnO

Relative to other semiconductors, ZnO is radiation hard [13, 29-33], with some authors reporting the annealing out of implantation damage at temperatures well below room temperature [34-36]. Table 1.1 compares the displacement energies of atoms in ZnO with Si, diamond, GaN and GaAs. As can be seen the displacement energies for the host atoms in ZnO are higher than is seen for other commonly studied semiconductors, which means that it is more difficult to remove an atom from its normal lattice site. However, this fact alone is not enough to explain the radiation hardness of ZnO when irradiated with electrons, protons and ions with

energies of the order of keV-MeV. It appears that strong self-recovery of the lattice takes place faster than the rate of damage build-up [37].

Material	ZnO [29]	Diamond [29]	Si [29]	GaN [33]	GaAs [34]
Anion displacement energy (eV)	41-57	80	13	11	9-10
Cation displacement energy (eV)	18.5			20.5	9-10

Table 1.1: Displacement energies for host atoms in a selection of semiconductors

Emission channelling results can provide much useful information on the lattice location of implanted ions, and how this changes with annealing temperature. Wahl *et al.* [38] performed a study on the lattice location of Cu and Ag ions after implantation and after various anneal stages. It was found that the concentration of Cu ions on a Zn-substitutional site varied with the concentration dose; at low doses, 2×10^{13} cm^{-2}, nearly all the Cu ions were located on Zn-sites after implantation, while at higher doses, 2×10^{14} cm^{-2}, only 55(4) % of ions were located on Zn-sites. Annealing at 700 °C increased the displacement of Cu ions from normal Zn-sites, with out-diffusion of the implanted species observed after treatment at 800 °C. Measurements of Ag-implanted samples revealed that only 30-45 % of as-implanted ions were located at or near Zn-sites, with a higher displacement from the normal Zn-site than for Cu-implanted atoms. Annealing at 800 °C again resulted in out-diffusion; approximately 30 % of the implanted ions being removed in this case.

1.3 Radioactive ion implantation

1.3.1 Introduction to radioactive ion implantation

The implantation of different isotopes of the same element can often be used to identify the chemical linked to a particular emission line. This can, usually, be seen by a shift in the zero phonon line (ZPL) line of a particular electronic transition, but is seen more readily in the phonon replicas, where the effect of the change in mass on vibrational energy comes into play. An isotope shift provides unambiguous proof of the chemical identity of a particular emission line. However, as this shift scales with the square root of the inverse mass ratio of two isotopes, such an effect is difficult to observe for high mass elements.

A common technique used to identify defects involves implanting a range of ion concentrations into a number of samples, annealing out the implantation damage and performing some analytical technique such as PL. A linear relationship between the intensity of a particular emission line and the implanted defect concentration suggests an association between the implanted ion and the signal in question [39]. One difficulty with this methodology is that a number of different samples must be used, which may have different initial impurity concentrations of various defects. Also, it can sometimes be difficult to discriminate between signals caused by implantation damage and those related to the implanted ion itself. The use of radioactive ion implantation can be used to circumvent these problems, as only one sample is needed, with the defect concentration changing at a rate determined by the half-life of the implanted species.

PL, though sensitive to low defect concentrations of the order of 10^{10} cm^{-3} [39] in very pure crystals, is a chemically blind technique. However, the use of radioactive ion implantations in conjunction with PL can be used to identify the elemental nature of a particular defect. The basic experiment involves monitoring the PL spectrum over a number of half-lives of the implanted isotope. A feature that increases/decreases in intensity with the same half-life of the isotope can usually (see Section 1.3.2 on recoil energy) be attributed to the daughter/mother isotope, respectively. The use of radioactive isotopes as a diagnostic tool in semiconductors was pioneered by Broser *et al.* in 1965 [40] with the study of neutron transmutation

doping of ZnS. In that work, the intensities of absorption and emission bands in the infrared were found to correlate with the concentration of Cu, a decay product from the radioactive isotope ^{75}Zn, in the samples.

One problem with the use of this technique is that it is often necessary to keep the implanted sample at low temperatures throughout the measurement period in order to prevent diffusion of the implanted species or diffusion of compensating centres. This effect was seen by Daly *et al.* [41]. After implanting Si with ^{111}In, which decays to ^{111}Cd with a half-life of 2.9 days, a known In-related bound exciton feature was found to disappear within thirty hours, much faster than the radioactive decay rate. As the sample temperature rose to 300 K between measurements, this was believed to be due to passivation by impurities that diffuse at this temperature. Keeping the sample at low temperature throughout the rest of the measurement period resulted in a signal that decayed at the same rate as the concentration of the implanted isotope. A similar effect was seen with a slower than expected growth of an emission line related to the daughter isotope.

One interesting possibility offered by the transmutation effect is the possibility of generating defects at a lattice location not normally seen through conventional doping techniques. Such an experiment was performed by Magerle *et al.* [42]. ^{71}As, which decays through ^{71}Ge to ^{71}Ga, was implanted into GaAs. This should lead to the creation of the anti-site Ga_{As} (Ga on an As site), which one expects to act as a double acceptor, while Ge should act as a simple acceptor in GaAs. A feature related to the Ge acceptor was found to follow the concentration of Ge over the course of the measurement period; however, no signal could be matched to the concentration of the anti-site defect.

If a particular emission feature involves a pair of atoms, this will be reflected in the rate of change of the intensity of the monitored feature in comparison to the half-life of the implanted isotope. If the feature is related to the mother isotope, the intensity of the signal should decrease at a rate equal to half the half-life; on the other hand, if the signal is related to pairs of the daughter isotope, the feature should increase in intensity at a rate equal to twice the half-life. Henry *et al.* [43] observed a feature that decayed with a half-life of 8 hours in Si implanted with ^{193}Hg, with a half-life of four

hours, which decays to ^{193}Au with a half-life of 17 hours. This signal was attributed to a complex which contained two Au atoms and a Li atom, a known impurity in the sample. Another feature at 1066 meV, previously attributed to an Fe-B complex through diffusion studies, was found to decay at a rate consistent with ^{193}Au, showing that Au must also be involved in the complex. These and other successful applications are described by Henry *et al.* [43].

1.3.2 Recoil energy

A number of factors need to be considered in order to choose a suitable isotope. Firstly, the half-life of an implanted isotope has to be high enough in order to allow sufficient data to be taken, but low enough to allow stable experimental conditions over the course of the measurements. The yield from a particular target must also be high enough to allow one to implant a sufficient number of atoms in a reasonable amount of time.

Another important factor to consider is the kinetic energy of the daughter isotope after the decay process. The magnitude of the recoil energy of the daughter product can be calculated, depending on whether the decay is by β or γ emission, by the following equations presented in [44].

$$E_R(\gamma) = \frac{E_\gamma^{\,2}}{2Mc^2} \qquad \textbf{1.1}$$

and

$$E_R(\beta) = \frac{E_\beta(E_\beta + 2mc^2)}{2Mc^2} \qquad \textbf{1.2}$$

M is the mass of the daughter isotope, while m is the mass of an electron. $E_R(\gamma)$ and $E_R(\beta)$ are the energies of the γ-ray and β particle, respectively.

If the recoil of the daughter isotope is larger than the displacement energy of the host atoms, there exists the possibility that vacancy and interstitial defects may be created. This could create competing centres for exciton capture, causing a luminescence signal to decrease with the half-life of the implanted species, without

there being any direct chemical connection. Alternatively, it could also create defect centres that increase with radioactive decay. We see examples of the latter process in Chapters 3 and 4. High recoil energy also means that it is unlikely that the daughter isotope will remain on the same lattice site as the mother isotope. In this work, we have used the maximum β energy for each implanted isotope to see whether displacement of Zn and O atoms after implantation is a significant effect.

1.4 Layout of Thesis

Following the brief overview of the thesis presented in this chapter, a detailed introduction to photoluminescence, the experimental systems used, and the photoluminescence signals typically seen in ZnO is provided in Chapter 2. In Chapter 3 the results of implantations of stable and radioactive isotopes of Zn and Ga into ZnO is described in detail. Here, a neutral donor bound exciton feature at 3.3600 eV was found to be Ga-related, while a deep donor bound exciton at 3.3225 eV was found to be due to excitonic recombination at a Ge double donor. Chapter 4 describes the effects of implantations of Cu and Ni on the structured green band, a commonly observed feature in photoluminescence spectra of ZnO. A discussion of the effects of implantation damage and recoil energy is also provided. The rate of change of the green band was found to be independent of the implanted isotopes, and was assigned to the creation of Zn-vacancies caused by the high recoil of the daughter isotopes. Chapter 5 introduces new photoluminescence signals seen in the near **IR** and shows the behaviour of these optical signals as a function of temperature. Chapter 6 presents the excitation spectra of the emission signals discussed in Chapter 5, and compares these spectra with the excitation spectra of the overlapping Fe^{3+} emission lines. Chapter 7 presents some initial results for radioactive Cd- and Be-implanted material. A series of sharp emission lines, between the bound exciton and the phonon replica regions, were observed. These emission lines appear similar to those observed in MBE grown GaAs. An attempt to categorize these lines as being due to pairs of defects at various separations was made. Finally, Chapter 8 summarises the principal results and offers some ideas for future work in the areas discussed in this thesis.

References

1. H. J. Yearian, Phys. Rev., **48**, 631 (1935).
2. Ü. Özgür, Y. I. Alivov, C. Liu, A. Teke, M. A. Reshchikov, S. Doğan, V. Avrutin, S.-J. Cho, and H. Morkoç, J. Appl. Phys., **98**, 041301 (2005).
3. A. R. Hutson, Phys. Rev., **108**, 222 (1957).
4. D. C. Reynolds, C. W. Litton, T. C. Collins, Phys. Rev., **140**, A1726 (1965).
5. H. Ibach, Phys. Rev. Lett., **24**, 1416 (1970).
6. H.-J. Schulz, M. Thiede, Phys. Rev. B, **35**, 18 (1987).
7. C. Klingshirn, R. Hauschild, H. Priller, M. Decker, J. Zeller, H. Kalt, Superlattices and Microstructures, **38**, 209 (2005).
8. Z. L. Wang, J. Phys. Condens. Matter., **16**, R829 (2004).
9. A. Janotti, C. G. Van de Walle, J. Cryst. Growth, **287**, 58 (2006).
10. A. Janotti, C. G. Van de Walle, Appl. Phys. Lett., **87**, 122102 (2005).
11. A. F. Kohan, G. Ceder, D. Morgan, C. G. Van de Walle, Phys. Rev. B, **61**, 15019 (2000).
12. J. L. Zhao, W. Zhang, X. M. Li, J. W. Feng, X. Shi, J. Phys. Condens. Mater., **18**, 1495 (2006).
13. F. Tuomisto, V. Ranki, K. Saarinen, D. C. Look, Phys. Rev. Lett., **91**, 205502 . (2003).
14. C. G. Van de Walle, Phys. Rev. Lett., **85**, 1012 (2000).
15. K. Ip *et al.*, Solid State Electronics, **47**, 2255 (2003).
16. Z. Zhou, K. Kato, T. Komaki, M. Yoshino, H. Yukawa, M. Morinaga, International Journal of Hydrogen Energy, **29**, 323 (2004).
17. D. C. Look, C. Coşkun, B. Claflin, G. C. Farlow, Physica B, **340-342**, 32 (2002).
18. C. H. Park, S. B. Zhang, Su-Huai Wei, Phys. Rev. B, **66**, 073202 (2002).
19. K. Minegishi, Y. Koiwai, K. Kikuchi, Japan. J. Appl. Phys., **36**, L1453 (1997).
20. M. Joseph, H. Tabata, T. Kawai, Jpn. J. Appl. Phys., **38**, L1205 (1999).
21. T. Yamamoto, H. Katayama, Jpn. J. Appl. Phys., **38**, L166 (1999).
22. K. K. Kim, H. S. Kim, D. K. Hwang, J. H. Lim, S. J. Park, Appl. Phys. Lett., **83**, 63 (2003).
23. Y. R. Ryu, T. S. Lee, H. W. White, Appl. Phys. Lett., **83**, 87 (2003).

24. T. Aoki, Y. Shimizu, A. Miyake, A. Nakamura, Y. Nakanishi, Y. Hatanaka, Phys. Stat. Solidi (b), **229**, 911 (2002).
25. S. Limpijumnong, S. B. Zhang, S. H. Wei, C. H. Park, Phys. Rev. Lett., **92**, 155504 (2004).
26. B. K. Meyer, H. Alves, D. M. Hofmann, W. Kriegseis, D. Forster, F. Bertram, J. Christen, A. Hoffmann, M. Straßburg, M. Dworzak, U. Haboeck, A. V. Rodina, Phys. Stat. Sol. (b), **241**, 231 (2004).
27. G. Carter, W. A. Grant, Ion implantation of Semiconductors, (Edward Arnold, London, 1976).
28. James F. Ziegler, www.srim.org , *19/07/06*.
29. D. C. Look, J. W. Hemsky, J. R. Sizelove, Phys. Rev. Lett., **82**, 2552 (1999).
30. D. C. Look, D. C. Reynolds, J. W. Hemsky, R. L. Jones, J. R. Sizelove, Appl. Phys. Lett., **75**, 811 (1999).
31. A. Y. Polyakov, N. B. Smirnov, A. V. Govorkov, E. A. Kozhukhova, V. I. Vdovin, K. IP, M. E. Overberg, Y. W. Heo, D. P. Norton, S. J. Pearton, J. M. Zavada, V. A. Dravin, J. Appl. Phys., **94**, 2895 (2003).
32. D. C. Look, D. C. Reynolds, J. W. Hemsky, J. R. Sizelove, R. L. Jones, R. J. Molnar, Phys. Rev. Lett., **79**, 2273 (1997).
33. D. Pons and J. C. Bougoin, J. Phys. C: Solid State Phys., **18**, 3839 (1985).
34. L. S. Vlasenko, G. D. Watkins, Phys. Rev. B, **71**, 125210 (2005).
35. K. Lorenz, E. Alves, E. Wendler, O. Bilani, W. Wesch, M. Hayes, Appl. Phys. Lett., **87**, 191904 (2005).
36. S. O. Kucheyev, J. S. Williams, C. Jagadish, J. Zou, C. Evans, A. J. Nelson, A. V. Hamza, Phys. Rev. B, **67**, 094115 (2003).
37. C. Coskun, D. C. Look, G. C. Farlow, J. R. Sizelove, Semicond. Sci. Tech., **19**, 752 (2004).
38. U. Wahl, E. Rita, J. G. Correia, T. Agne, E. Alves, J. C. Soares, The ISOLDE Collaboration, Superlattices and Microstructures, **39**, 229 (2006).
39. E. C. Lightowlers, Growth and Characterisation of Semiconductors, editors R. A. Stradling and P. C. Klipstein (Bristol: Hilger, 1990), 135.
40. I. Broser and H. K. Franke, J. Phys. Chem. Solids, **26**, 1013 (1965).
41. S. E. Daly, M. O. Henry, C. A. Frehill, K. Freitag, R. Vianden, G. Rohrlack, D. Forkel, Mater. Sci. Forum, **196-201**, 1497 (1996).

42. R. Magerle, Defects in Electronic Materials II, (Pittsburgh, 1997), eds. J. Michel, T. Kennedy, K. Wada, K. Thonke, MRS Symp. Proc., **442**, 3 (1997).
43. M. O. Henry, M. Deicher, R. E. Magerle, E. McGlynn, A. Stotzler, Hyperfine Interactions, **129**, 443 (2000).
44. M. A. Vesaghi, Phys. Rev. B, **25**, 5436 (1982).

Chapter 2: Experimental Procedure

2.1 Photoluminescence

Photoluminescence is a non-destructive optical technique that can be used to determine material quality, identify defects and, in favourable cases, defect concentrations. It is an extremely sensitive form of spectroscopy capable of detecting defects at concentrations as low as 10^{10} cm^{-3} [1]. In comparison, Hall measurements need a minimum defect concentration of approximately 10^{14} cm^{-3}, Raman studies require a concentration of the order of 10^{18} cm^{-3}, and the presence of unpaired electrons is a necessary condition for EPR (Electron Paramagnetic Resonance) measurements.

When light with photon energy greater than the band-gap illuminates a sample, electrons are excited to the conduction band leaving holes in the valence band. These carriers can become attracted to each other by their mutual Coulombic attraction. The resultant neutrally charged composite is known as an exciton. The simplest relaxation process is the recombination of the electron-hole pair, which results in a photon with energy lower than the band-gap energy by an amount corresponding to the binding energy of the exciton. This is the free exciton energy, E_R. The difference between the free exciton energy and the band-gap energy is just the binding energy of the electron-hole pair, E_x:

$$E_R = E_{BG} - E_X \qquad \textbf{2.1}$$

where E_{BG} is the band-gap energy. The exciton binding energy in ZnO is high-60 meV in comparison to the exciton binding energy of ~26 meV in GaN. This high binding energy ensures that excitonic recombination processes persist to well above room temperature.

Except for extremely high purity materials, recombination of the free exciton does not tend to be the most likely recombination process. The probability for this transition to occur is lower than the probability that the exciton will become trapped at a defect or impurity before it recombines.

The recombination energy, E_D, in the case of recombination at a defect is:

$$E_D = E_{BG} - E_X - E_\tau \qquad \textbf{2.2}$$

E_τ depends on the particular defect, its electronic configuration and the nature of the binding to neighbouring atoms, and is referred to as the localisation energy. It is therefore largely specific to a particular impurity or defect. Another common radiative transition is donor-acceptor pair recombination [2]. If an electron becomes trapped at an ionized donor while a hole is trapped at an ionized acceptor, the electron-hole pair can then recombine to leave the ionized donor and acceptor while also emitting a photon of light. The energy of this photon, assuming that the donor and acceptor are infinitely separated (with no interaction between the two) is simply:

$$E_{DAP} = E_{BG} - (E_A + E_D) \qquad \textbf{2.3}$$

E_A is the acceptor binding energy and E_D, the donor binding energy. If there is an overlap between the acceptor and donor wavefunctions then the recombination energy will be [3]:

$$E_{DAP} = E_{BG} - (E_A + E_D) + \frac{e^2}{\varepsilon_0 R} - f(R) \qquad \textbf{2.4}$$

The third term in equation 2.4 represents the Coulombic energy between the donor and acceptor. The fourth term in this equation is a correction term for small donor-acceptor pair separations and includes repulsive interactions between donors and holes and acceptors and electrons, and attractive interactions between the donors and acceptors and electrons and holes. At large separations these factors sum to zero.

Transitions between electrons in the conduction band to acceptors, holes in the valence band to donors, and internal transitions of particular defects can also be seen using photoluminescence. Fig. 2.1 shows, schematically, some of the possible recombination processes [4].

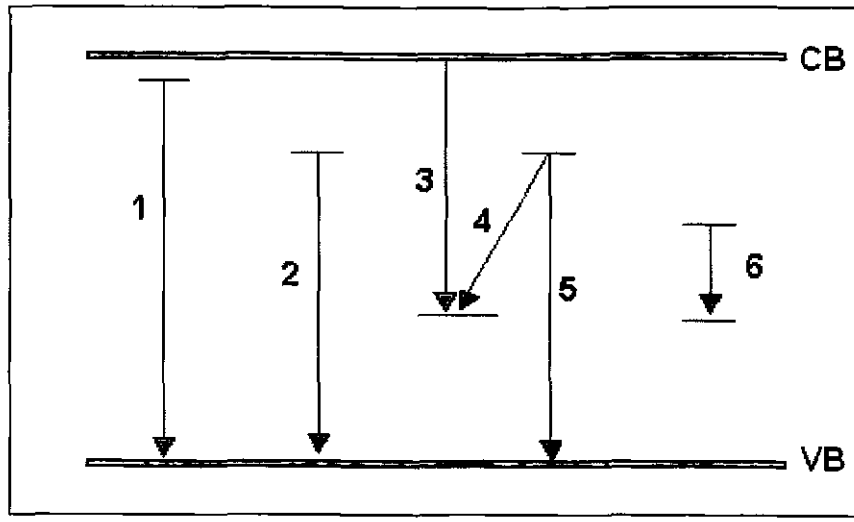

Figure 2 1: Diagram of PL processes with: 1 – free exciton, 2 – bound exciton, 3 – electron to acceptor, 4 – donor to acceptor, 5 – hole to donor, 6 – impurity or defect internal transition

2.2 Experimental Apparatus

The photoluminescence spectra presented in this thesis were obtained using three different systems; either a dispersive spectrometer or a Fourier Transform (FT) system fitted with photomultiplier tubes at DCU, and a dispersive system with a CCD camera at CERN. The systems at DCU employ closed cycle cryostats while the system at CERN uses a liquid helium cryostat. These will be described in the following sections.

2.2.1 Dispersive system at DCU

In this system luminescence is dispersed by a 1 m Czerny-Turner (Spex 1704) grating monochromator with a 1200 lines/mm grating, blazed at 330 nm. The grating position can be moved so that the wavelength reaching the exit slit varies from 0-1500 nm. The monochromator has an accuracy of ± 0.1 nm over 600 nm and a repeatability (when moving the grating over a long range and back) of ± 0.03 nm. The minimum drive step size is 0.0025 nm. Table 2.1 shows the effect of the entrance and exit slit widths on the resolution of lines, using the 325 nm line of a HeCd laser as a reference source. The linewidth of the laser is < 0.001 eV, and therefore the values given in table 2.1 are indicative of the resolution of the monochromator/grating at each slit width.

Slit Width (μm)	FWHM at 325 nm (meV)
5	0.22
10	0.29
20	0.34
50	0.50
100	0.94
200	1.81
500	4.61

Table 2.1: Effect on resolution of changing slit width

Figure 2.2 demonstrates, graphically, the change in linewidth with the change in slit width. The spectrum in blue represents the resolution achievable when the slits are set to 500 μm, while the green, red and black spectra represent the resolution obtained while the slits are set to 200, 50 and 5 μm respectively.

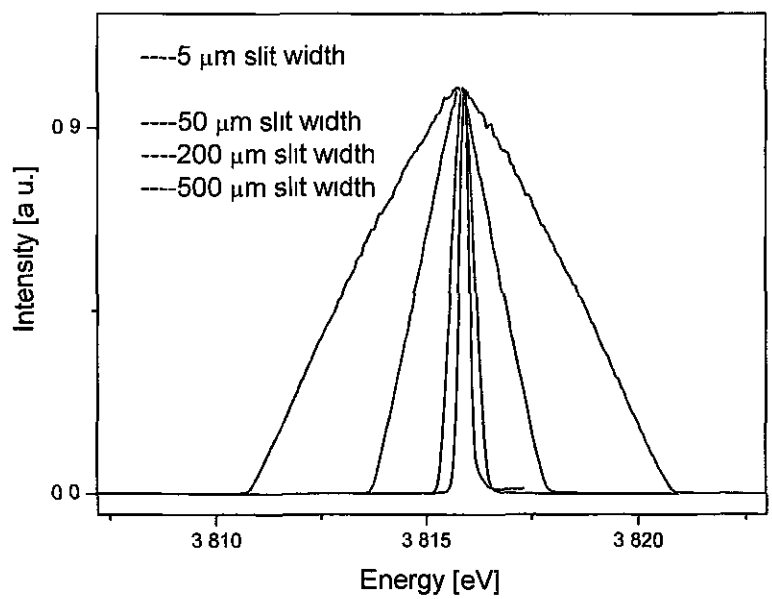

Fig 2.2: Plot showing the effect of increasing slit width on the shape of the laser line

In the following chapters, based on data from Table 2.1 and Fig. 2.2, the resolution will be indicated by a number in parenthesis following the wavelength/energy

position of a feature. For example, for a slit width of 100μm, the laser peak is found to be at 324.92(2) nm, or 3.382(1) eV. SpectraMax software from the Jobin-Yvon Corporation was used for data acquisition which controls the position of the grating via an IEEE card.

Luminescence was detected with a Hamamatsu (model R3310-02) photomultiplier tube (PMT) which is Peltier cooled to -25 °C in order to reduce dark counts. The signal from the PMT is put through a low noise pre-amp (BM302) before being interfaced to the computer. This model of PMT can be used in photon-counting, current or voltage output modes. In this work, the normal operating mode is photon-counting while the voltage mode is used for some of the experiments described in Chapter 7, where a Lock-in Amplifier was used.

The ZnO wafers were placed in a closed cycle cryostat (Janis Corporation, model SHI-950-5) and the sample space is filled with helium gas, which is inert and acts as a heat transfer between the warm sample space and the cold heat exchanger. The sample space is surrounded by a vacuum shroud which is initially pumped to about 10^{-3} bar using a rotary pump. The pressure drops further to about 10^{-5} bar due to cryo-pumping as the sample cools down. Each ZnO crystal was attached with PTFE thread onto a sample stick; PTFE was sufficiently flexible so as to prevent strain. The temperature was monitored and varied with a silicon diode sensor and a resistive heater, respectively, on the sample holder. The temperature was controlled using a Lakeshore (model 330) temperature which can control the temperature to ± 0.2 K for long periods of time. Measurements presented here were taken between ~5.5 K and room temperature.

An unfocused HeCd laser (Kimmon Corporation, model IK5625R-G) operating at 325 nm was used to excite the band-edge luminescence of ZnO. The output power at this wavelength is 40 mW. A UV band-pass filter, UG11 (labelled F1 in Fig. 2.3), is placed between the laser and the sample in order to attenuate laser plasma lines and to ensure that it is predominantly the laser line at 325 nm that reaches the sample. The luminescence was focused onto the entrance slit of the monochromator using lenses. A wide band-pass clear filter, labelled F2 in the diagram, was placed at the entrance slit to block the laser line. This laser has another line at 442 nm with an

output power of 120 mW. For the study of longer wavelength spectral features, a diode pumped Nd-YAG laser (Spectra-Physics, model Millenia IIs) with a frequency doubled continuous-wave output of 532 nm was used. The output power of this laser can be varied from 200 mW to 2 W. A wide-band pass filter (KC15) is used to attenuate the laser line for these measurements.

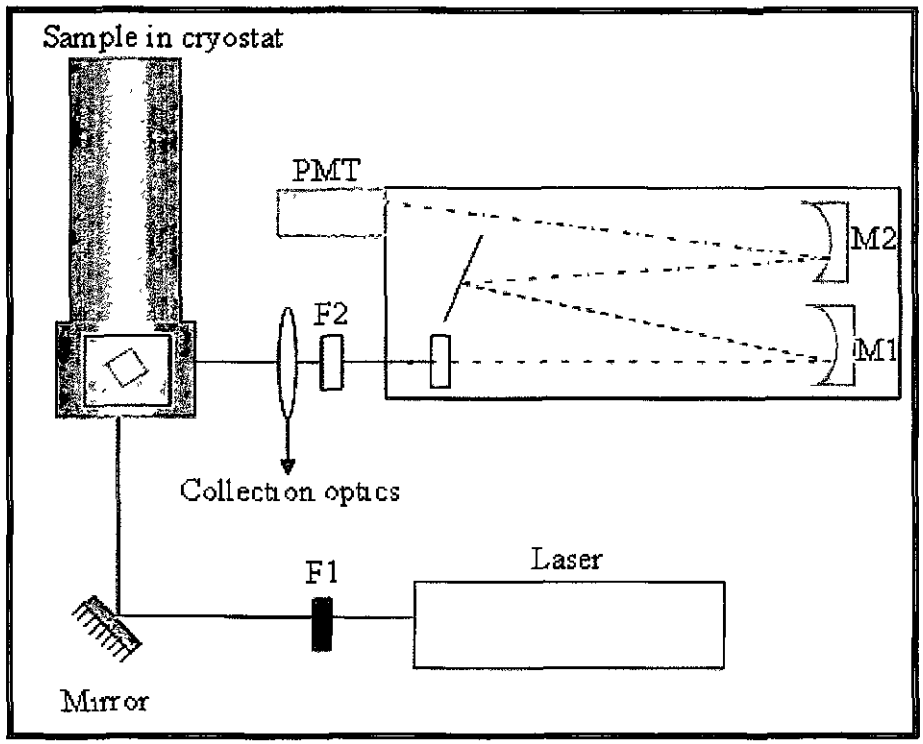

Figure 2.3. Schematic diagram of photoluminescence experimental set-up

2.2.2 Fourier Transform System at DCU

The second system used to acquire spectra is a Bomen DA8 Fourier Transform (FT) spectrometer. The sample is cooled using a Janis CCS-500 closed cycle cryostat, and the sample space can reach 20 K using this system. A 27 Ω rhodium-iron sensor and a resistive heater are placed on the sample stick and an Oxford Instruments ITC-4 controller was used to monitor and control the temperature. The excitation sources in this lab are the same models as used with the dispersive system. Luminescence is detected using a Hamamatsu R1913 PM tube. The output of the PM is inputted to a Bomen variable gain preamplifier (#IEH5700L) before being put though a vector processor which performs a Fourier Transform of the PM output to produce a PL

spectrum. The resolution of the spectra taken in this system depends on the mirror movement distance. The data presented in this work acquired using the FT system has a resolution better than 0.1 meV. A liquid helium flow cryostat can also be used in this system. For band-edge photoluminescence studies, a bandpass filter (BG25) is used, while a wide band-pass filter (KC19) is used for longer wavelength studies.

2.2.3 Dispersive System at CERN

For samples implanted with radioactive isotopes and measured on-site at CERN, a 0.75 m Spex 750 M monochromator was used to disperse the luminescence. When used with a 1200 lines/mm grating the spectral range of this monochromator is 0-1500 nm and the resolution is 0.01 nm. There are three different gratings available, which allow one to examine luminescence in different energy regions with varying resolution. Table 2.2 describes the range and peak wavelength response of each grating.

Grating (Lines/mm)	Blaze (nm)	Range (nm)
150	500	320-1000
1200	900	600-1600
1800	400	250-900

Table 2.2: Information on gratings used in CERN

The excitation source used is a HeCd laser (Kimmon, model IK3802R-G) with an output power of 82 mW. A Jobin-Yvon CCD 3000 camera is used to detect the luminescence. This camera is cooled with liquid nitrogen in order to reduce noise. A liquid helium flow cryostat (Konti IT) is used to cool the samples. The cryostat is filled with nitrogen a couple of days before measurements are taken, and topped up at regular intervals, to cool the sample space to approximately 150 K before filling with helium. This conserves the helium and is more cost-efficient. Helium is drawn into the sample space using a rotary pump to create a pressure differential, and the measurement temperature is typically 1.6 K. A Lakeshore 331 temperature controller

is used if measurements at a higher temperature are needed. Radioactivity shielding is provided by placing lead bricks around the cryostat.

2.3 Photoluminescence of ZnO

The luminescence of ZnO varies significantly from sample to sample, even in material supplied by the same manufacturer. Quite different luminescence can also be obtained depending on whether one examines the O or the Zn terminated surface of a sample. However, there are still quite a few common features.

The band-edge luminescence is dominated by a series of sharp lines in the region between 3.3595 eV to 3.364 eV. Zeeman experiments have shown that these are due to excitonic recombination at neutral donors [5]. In high purity ZnO, such as samples purchased from Cermet [6] and Eagle-Pitcher [7], free exciton related signals are seen at a higher energy. Figure 2.5 shows a typical spectrum of the band-edge region of ZnO at low temperatures.

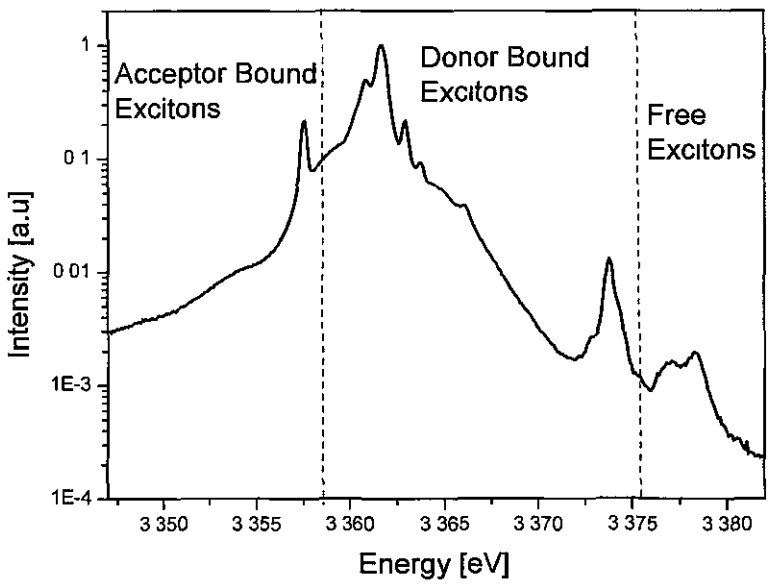

Figure 2.5: Typical low temperature photoluminescence spectrum of ZnO

At ~3.3 eV, two electron-satellites (TES) of the donor bound exciton (DX) lines can be seen. TES recombination occurs when exciton recombination at a donor leaves

the donor in an excited state. The intensity of the TES feature matches the relative intensity of its corresponding DX, although the lines are much broader. Effective mass theory (which considers the donor as a hydrogen-like atom) can be used to determine the binding energy of the donor by examining the separation between a donor and its corresponding TES [8].

$$E_D = \frac{4}{3}\left(E_{DX} - E_{TES}\right) \qquad \textbf{2.5}$$

Figure 2.6 shows an example of this effect; the upper spectrum shows the photoluminescence spectrum of the band edge region at 1.8 K, and the lower spectrum the TES region measured at the same temperature. The inset of the upper spectrum shows an energy diagram. The difference in energy between the most intense DX line and its corresponding TES is ~41.3 meV. Assuming the effective mass approximation holds true, a value for the donor binding energy of 55 meV is obtained.

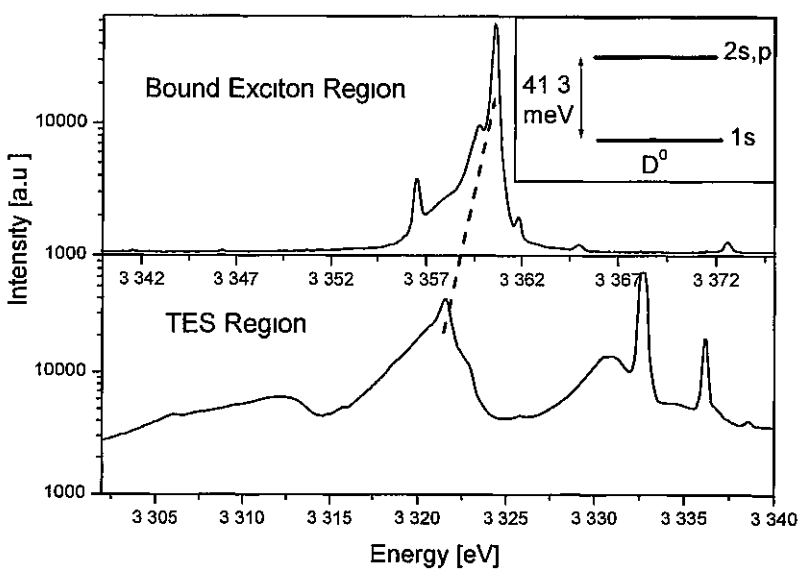

Figure 2.6: Photoluminescence spectra of ZnO measured at 1.8 K.

LO phonon replicas of free excitons and neutral donors are also observed at ~73 meV intervals lower in energy than the direct transition. Donor-acceptor pair recombination (DAP) is also seen in some cases. Figure 2.7 shows the LO phonon region with phonon replicas of the FE, DX, TES and DAP apparent. DAP transitions and TES can also be seen.

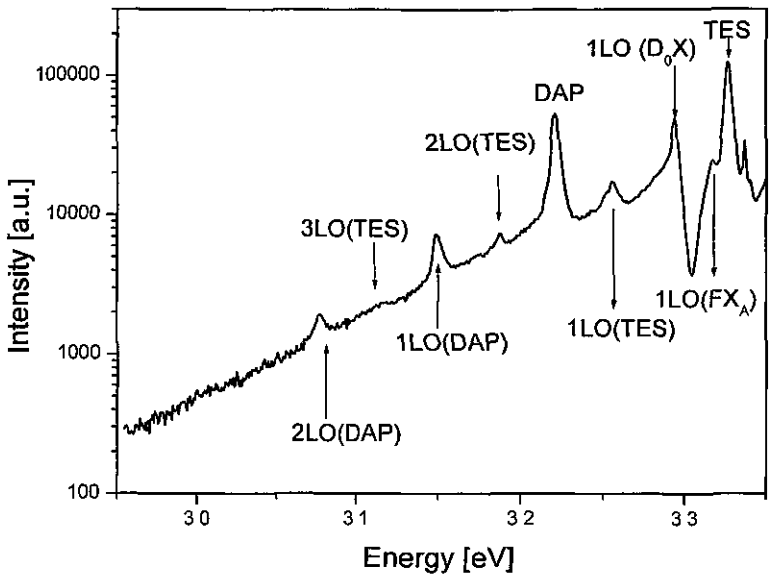

Figure 2 7: Lower energy PL spectrum of ZnO. Here the TES can be seen along with LO phonon replicas of the principal DX line and FX. A line that has been attributed to a DAP signal is also seen

2.4 Temperature Dependence

2.4.1 Change in intensity as a function of temperature

The luminescence intensity of spectral features can change significantly with temperature. As the temperature is increased from very low temperatures, the intensity of a particular feature will generally increase as excitons become released from shallower levels, and thus become available for capture. At higher temperatures, excitons become released from the defect site, and a decrease in intensity is seen. In general, the luminescence intensity can be modelled by the function [9, 10]:

$$I(T) = I(0).[C_1 \exp(-E_1 / k_B T)/(C_2 \exp(-E_2 / k_B T) + 1)] \qquad \textbf{2.6}$$

I (T) and *I (0)* are the intensities of the particular feature at temperatures T and 0 K respectively; E_1 and E_2 are deactivation energies, while *C1* and *C2* are pre-exponential factors related to transition probabilities and degeneracies of states. The numerator represents the deactivation energy of the defect losing excitons to the feature in question, causing an increase in the intensity of that feature. The

denominator represents the activation energy of the loss mechanism of the defect. This is shown in Fig. 2.8.

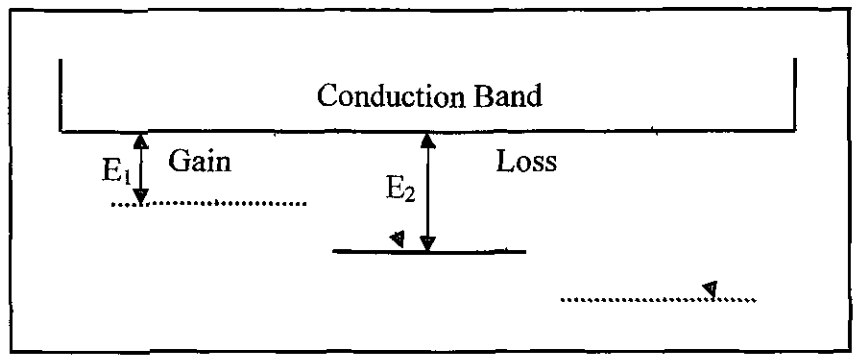

Figure 2.8: *Schematic diagram describing processes which result in changes in the intensity of spectral features as the temperature is increased. E_1 is the deactivation energy of the shallow level which loses excitons to the feature in question, resulting in an increase in intensity; E_2 is the activation energy of the loss mechanism of the defect*

In order to calculate the activation energy of a defect, only the temperature region where the PL intensity is decreasing need be considered. To model this, only part of equation 2.6 is necessary. Here, the maximum intensity, I_{max} is used rather than the intensity at 0 K.

$$I(T) = [I_{\max} / (C_2 \exp(-E_2 / k_B T) + 1)] \qquad \textbf{2.7}$$

Taking the above equation, rearranging and taking the natural log of both sides of the equation results in the following:

$$\ln\left(\frac{I_{\max}}{I(T)} - 1\right) = \ln C_2 - \frac{E_2}{k_B T} \qquad \textbf{2.8}$$

A plot with $\ln\left(\frac{I_{\max}}{I(T)} - 1\right)$ on the y-axis against $\frac{1}{T}$ on the x-axis should be a straight line with a slope of $-\frac{E_2}{k_B}$ and an intercept of $\ln C_2$.

If, on the other hand, we only consider the region in which the PL signal is increasing, information can be obtained on the deactivation energy of the trap losing excitons to the feature. This region corresponds to the

$$I(T) = I(0).C_1 \exp(-E_1 / k_B T) \qquad \textbf{2.9}$$

Again, taking the natural log of both sides of equation 2.9, the following is obtained

$$\ln\left(\frac{I(T)}{I(0)}\right) = \ln C_1 - \frac{E_1}{k_B T} \qquad \textbf{2.10}$$

2.4.2 Transitions between two excited states to a common ground state model

In PL studies of transition metals and other defects/impurities, transitions between different excited states to a common ground state are often seen [10]. The simplest system is that of transitions between two excited states and a common ground state; such a system is depicted in Fig. 2.9.

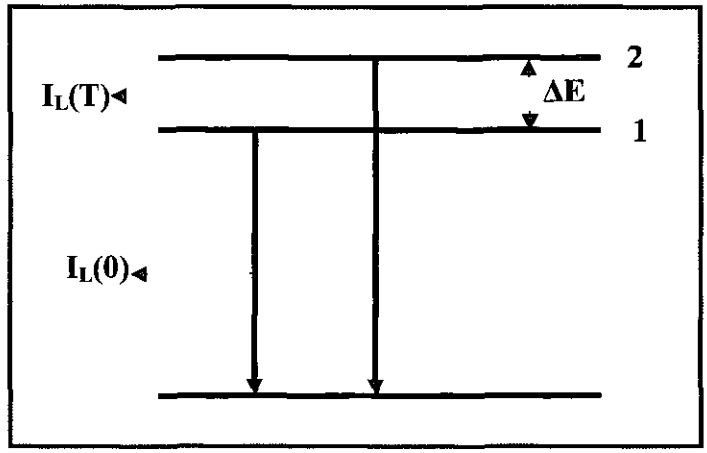

Figure 2.9: Diagram of a two-level system, separated by an energy ΔE

At T = 0 K, only the lower level (1) is populated, but as the temperature is increased, the upper level (2) becomes thermally populated. This causes a decrease in the intensity of the lower energy emission line, which coincides with the appearance and subsequent increase of a higher energy line, associated with the higher energy level. The population of the upper level follows a Boltzmann distribution, and is shown below.

$$N_2 = N_1 g_{21} \exp(-\Delta E / k_B T) \qquad \textbf{2.9}$$

where N_i is the population of the i^{th} level, ΔE is the energy gap between the two levels, and g_{21} is the ratio of the degeneracy between the upper and lower states. The intensity of each transition is proportional to the product of the population of the level and the probability for that transition to occur. Therefore, the intensity of the transition from level 1 to the ground state is

$$I_1 = N_1 f_1 \qquad \textbf{2.10}$$

and the intensity of transition 2 to the ground state is

$$I_2 = N_2 f_2 = N_1 g_{21} \exp(-\Delta E / k_B T) f_2 \qquad \textbf{2.11}$$

Therefore, the intensity ratio for the two transitions will be

$$\frac{I_2}{I_1} = \frac{g_{21} \exp(-\Delta E / k_B T) f_2}{f_1} \qquad \textbf{2.12}$$

Taking the natural log of both sides of the equation, results in the following relationship between the relative intensities of the two lines.

$$\ln\left(\frac{I_2}{I_1}\right) = -\frac{\Delta E}{k_B T} + \ln g_{21} + \ln f_2 - \ln f_1 \qquad \textbf{2.13}$$

The energy separation, ΔE, between the two levels can then be obtained from the slope of an Arrhenius plot, with the intercept giving the value ln ($g_{21}f_2/f_1$).

2.4.3 Change in FWHM and energy positions of spectral features with temperature

The model used to describe the behaviour of the line position and the linewidths of spectral features as a function of temperature is based on the model developed by Imbusch *et al.* [11] to describe the behaviour of PL signals from particular transition metals in MgO. In this model, the line broadening, Γ (T), and the shift in energy, Δω (T), as a function of temperature are described by the following equations,

$$\Delta\omega = \alpha \int_0^\infty \frac{d\omega}{2\pi} \rho(\omega) n(\omega) \qquad \textbf{2.14}$$

and

$$\Gamma(T) = \bar{\alpha} \int_0^\infty \frac{d\omega}{2\pi} [\rho(\omega)]^2 n(\omega)[1 + n(\omega)] \qquad \textbf{2.15}$$

where

$$n(\omega) = [\exp(\omega\hbar / kT) - 1]^{-1} \qquad \textbf{2.16}$$

and α and $\bar{\alpha}$ are constants proportional to the strength of the phonon-impurity interaction and $\rho(\omega)$ is an effective density of phonon states.

$$\rho(\omega) = \sum_k |s_k|^2 \, 2\pi\delta(\omega - \omega_k) \qquad \textbf{2.17}$$

The first part of the summation in equation 2.17, $|s_k|^2$, represents the phonon coupling parameter for each k-value, while the remainder is the phonon density of states.

Imbusch *et al* calculated values for $\rho(\omega)$ by relating the intensity of the phonon sidebands, as observed experimentally, to the following equation;

$$I(\omega) = |C|^2 \rho(\omega)/(\hbar\omega)^2 + \text{multiphonon terms} \qquad \textbf{2.18}$$

where ω is the separation from the ZPL and C is a constant. This model was found to fit the shift in energy of the ZPL as a function of temperature very well, but was found to fit the line broadening at low temperatures fairly weakly.

In the model used in this work, only one phonon, with an energy of $\hbar\omega$, is assumed to interact strongly with each emission line. Thus, equation 2.17 reduces to $|s_k|^2 2\pi$ and equations 2.14 and 2.15 become

$$\Delta\omega = \frac{\alpha |s_k|^2}{\exp(\hbar\omega/kT)-1} \qquad \textbf{2.19}$$

and

$$\Gamma(T) = \frac{\bar{\alpha} |s_k|^2 \exp(\hbar\omega/kT)}{[\exp(\hbar\omega/kT)-1]^2} \qquad \textbf{2.20}$$

2.5 Conclusions

In this Chapter, a general review of the PL equipment and of the PL spectrum of ZnO is provided. The fine structure in the PL, which forms the subject of the remainder of the thesis, has not been addressed. Such detail will be provided in the following chapters, in addition to technical details pertaining to the measurements.

References

1. E. C. Lightowlers, Growth and Characterisation of Semiconductors, editors R. A. Stradling and P. C. Klipstein (Bristol: Hilger, 1991), 135.
2. W. Hayes, A. M. Stoneham, Defects and defect processes in non-metallic solids (John-Wiley and Sons, New York, 1985), Chapter 5, 266-272.
3. R. K. Watts, Point Defects in Crystals (John Wiley and Sons, New York, 1977), Chapter 2.
4. P. K. Basu, Theory of optical processes in semiconductors: bulk and microstructures (Oxford University Press, New York, 1997), Chapter 5.
5. M. Strassburg, A. Rodina, M. Dworzak, U. Haboeck, I. L. Krestnikov, A. Hoffmann, O. Gelhausen, M. R. Phillips, H. R. Alves, A. Zeuner, D. M. Hoffmann, B. K. Meyer, Phys. Stat. Sol. (b), **241**, 607 (2004).
6. A. Teke, Ü. Özgür, S. Doğan, X. Gu, H. Morkoç, B. Nemeth, J. Nause, H. O. Everitt, Phys. Rev. B, **70**, 195207 (2004).
7. D. C. Reynolds, D. C. Look, B. Jogai, C. W. Litton, G. Cantwell, W. C. Harsch, Phys. Rev. B, **60**, 2340 (1999).
8. K. Thonke, Th. Gruber, N. Teofilov, R. Schönfelder, A. Waag, R. Sauer, Physica B, **340-342**, 945 (2001).
9. T. Monteiro, C. Boemare, M. J. Soares, E. Rita, E. Alves, J. Appl. Phys., **93**, 8995 (2003).
10. K. McGuigan, PhD thesis: Luminescence studies of transition metal related defects in crystalline silicon, 1989.
11. G. F. Imbusch, W. M. Yen, A. L. Schawlow, D. E. McCumber, M. D. Sturge, Phys. Rev., **133**, A1029 (1964).

Chapter 3: Study of the optical properties of Ga in ZnO

3.1 Introduction

The search for a reliable technique to grow p-type material is very much at the forefront of research in ZnO at the moment, and the presence of unintentionally incorporated donors is a major barrier to realising this goal. For this reason it is important to have a reliable method of identifying the presence of donors in order to try and prevent their introduction during ZnO film/single-crystal growth processes.

Ga in ZnO has been shown to act as an effective donor [1-4]. Ataev *et al.* [1] have produced Ga-doped films with a resistivity as low as 1.2×10^{-4} Ωcm that remained stable for at least a year. With regard to photoluminescence studies of ZnO, there have been many assignations of donor bound excitons to Ga. Kato *et al.* [5] have assigned a PL emission line at 3.362 eV to Ga after doping ZnO thin films, grown by molecular beam epitaxy (MBE), with that element. Ko *et al.* [6] attributed a feature at 3.358 eV to Ga, while no emission was observed at this energy before doping. Reuss *et al.* [7] observed a line at 3.359 eV after annealing a Ga-implanted sample. The energy of the relevant feature in each of these studies corresponds closely to the I_8 line as measured and named by Reynolds *et al.* during the 1960s [8], and thus a review paper by Meyer *et al.* [9] concludes that the I_8 line, at 3.3598 eV, involves Ga while a related paper by Strassburg *et al.* [10] demonstrates the donor nature of Ga in ZnO through Zeeman measurements.

Much of the previous work undertaken on the study of Ga-doped ZnO has relied heavily on Ga-diffusion as a doping technique but diffusion can have several disadvantages compared to ion implantation. Misidentification of the defect causing a particular optical (or other) signal can occur if there are contaminants in the diffusion source that have a higher diffusivity and/or solubility in the material than the desired dopant. Since the diffusivity of Ga in ZnO is quite low [11], unintentional contamination could be a particular problem with the use of diffusion as a doping method for this element. On the other hand, the implantation of stable ions does not always provide definitive proof of the chemical/elemental origin of a defect as the

process of ion implantation can create many different optical signals in the PL spectrum. Although the occurrence of an isotope shift can strongly confirm the identity of a particular defect, such shifts become increasingly small as the mass of the isotope increases [12]. Slight changes in sample temperature or the presence of strain could account for similar shifts in energy.

The bound exciton region of ZnO spans a relatively narrow energy range of approximately 25 meV, with as many as sixteen PL lines having been observed [8]. In some cases the separation between distinct bound exciton features is less than 1 meV [8, 10]. The discrepancy of 4 meV between the reported energies of lines assigned to Ga-related donor bound excitons in the literature suggests the possibility that bound exciton emission lines in this spectral region along with, or other than, I_8 may be Ga-related.

For these reasons implantation with radioactive isotopes is an attractive method for defect identification in ZnO and it was decided to implant radioactive isotopes of Ga or some suitable isotope that decays to Ga. ^{73}Ga and ^{72}Zn were chosen as they have half-lives that suit the measurement requirements, being short enough to allow one to keep the experimental conditions stable over the course of the measurements and long enough in order to allow a high enough concentration to be implanted.

Preliminary control experiments with implantations of stable isotopes of Ga and Zn were first undertaken. The Zn-implantation enabled identification of defects caused by implantation damage and intrinsic defects, while the Ga-implantation allowed investigation of the implantation and annealing conditions required to produce a Ga-related signal. Non-implanted samples were also annealed so that the effects of the annealing conditions on the luminescence spectrum could be determined.

3.2 Experiment Description

Implantations of ^{72}Zn and ^{73}Ga were performed at the ISOLDE (Isotope Separator On-Line) facility at CERN, Switzerland. The respective decay series of each isotope is shown below.

$$^{73}Ga \xrightarrow{4.87\,hrs} {}^{73}Ge$$

$$^{72}Zn \xrightarrow{1.93\,days} {}^{72}Ga \xrightarrow{14.1\,hrs} {}^{72}Ge$$

After implantation, the crystals were annealed at 800 °C for 30 minutes in an oxygen atmosphere of 0.5 bar in order to remove implantation damage. Spectra were taken on-site at CERN with the system described in Chapter 2. Measurements were made over the course of six half-lives of the implanted species. The samples were kept below 77 K between scans in order to prevent diffusion of the dopant atoms and spectra were taken with the samples at 1.6 K.

Stable isotopes of Zn and Ga were implanted at the Instituto Tecnológico e Nuclear in Portugal. These samples were annealed under the same conditions as above, but were examined using the FT system in DCU. A liquid helium flow cryostat was used and the samples were measured at 6 K. As a further control experiment, an un-treated wafer was annealed in an O_2 environment to ascertain what effect the anneal process would have on the PL spectra. PL measurements of this sample were made using the FT system at DCU at 6.5 K.

Hydrothermally grown ZnO crystals purchased from Rubicon Technology, USA were used as the starting material for the samples discussed in this chapter. In untreated ZnO from this supplier there is already some Ga in the material. Ga appears to be a common impurity in ZnO as the I_8 line is apparent in samples purchased from a number of different suppliers. Ideally, one would like to perform either diffusion or implantation studies with samples that did not originally contain the impurity of interest. However, as will be demonstrated below, the use of radioactive isotopes can provide strong evidence for defect identification even with a background impurity concentration.

3.3 Results

3.31 Implantation and Annealing Conditions

The implantation energy for the radioactive experiments was 250 keV for the Zn-implanted sample and 280 keV for the Ga-implanted sample with an implantation dose of approximately 10^{12} atoms in both cases. A slightly higher dose ~ 10^{13} cm^{-2} was used for the stable implantations. The surface concentration profile was 4×10^{12} atoms/cm^2 as a 5×5 mm^2 collimator was used. TRIM calculations were performed in order to estimate the implantation depth and concentration profile of the implanted isotopes. Figure 3.1 shows a histogram of the implantation depths for ^{73}Ga ions into ZnO based on these calculations. An implantation dose of 10000 atoms was chosen and the bin size of the depth was 10 nm. As can be seen, most of the atoms are in the 70 to 150 nm range and TRIM gives the longitudinal range as 107.1 nm, with a straggle of 42 nm. An approximation for the average concentration can be obtained by dividing the surface concentration by the longitudinal ion range. This gives us a concentration of 3.7×10^{17} cm^{-3} for the Ga implanted sample.

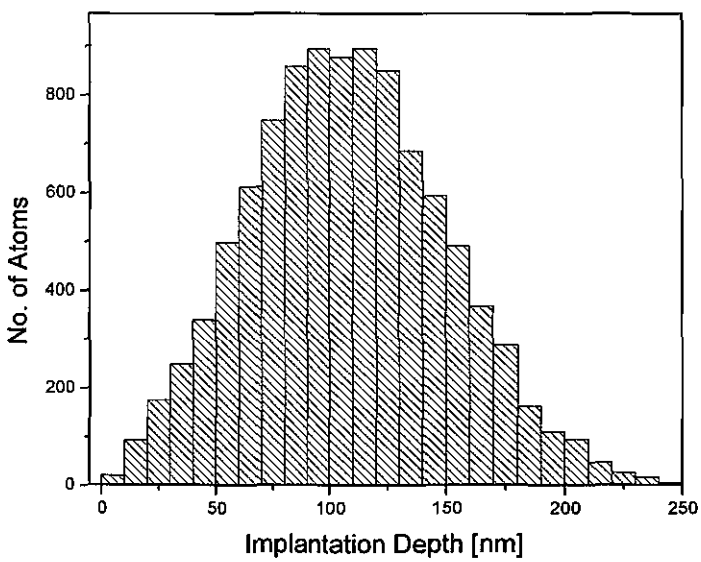

Figure 3.1: Histogram showing the calculated concentration profile for ^{73}Ga ions implanted at 280 keV

The results are similar for the ^{72}Zn implantation at 250 keV. The longitudinal ion range is 92.2 nm, with a straggle of 39.4 nm. Figure 2 shows the histogram representing the longitudinal range for the Zn implantation. The concentration

density of Zn atoms is, calculated in a manner analogous to the case of Ga above, found to be approximately 4.3×10^{17} ions/cm^{-3}.

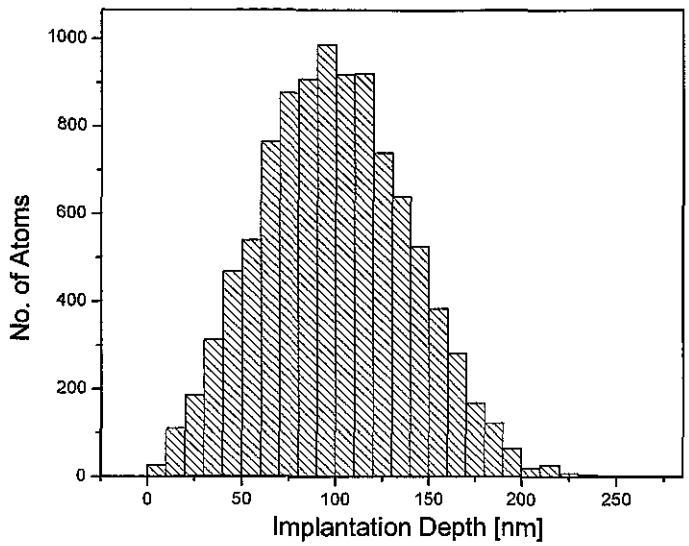

Figure 3.2: Histogram showing the calculated concentration profile for ^{72}Zn ions implanted at 250 keV

Although the above data give an approximate concentration profile for the implanted atoms, subsequent annealing can change this significantly. Annealing an implanted sample has two effects; it recovers crystalline structure but it also causes diffusion of the implanted ions.

In order to see what the likely concentration profile of the implanted atoms is after annealing, a number of simple calculations were performed. Using Fick's law of diffusion [13]:

$$D = D_0 \exp^{-\frac{E}{kT}} \qquad \textbf{3.1}$$

where D_0 is related to the jump frequency of the diffusing element and E is the activation energy, one gets a diffusivity of 1.373×10^{-15} cm^{2}s^{-1} for Zn and 6.126×10^{-18} cm^{2}s^{-1} for Ga after annealing at 973 K. Values for D_0 and E were taken from [11].

Sze [13] gives the formula for calculating the concentration profile obtained when doping, using a diffusion technique, with a finite source as:

$$C(x,t) = \frac{S}{\sqrt{\pi Dt}} \exp\left(\frac{-x^2}{4Dt}\right) \qquad 3.2$$

where S is the concentration per unit area, t is the annealing time, x is the depth and D is the diffusivity. Using equations 3.1 and 3.2 the concentration profile after annealing can be calculated. Below are plots of the calculated concentration profile of Zn and Ga after annealing at 973 K for 30 mins. As can be seen, Zn diffuses more easily than Ga in ZnO.

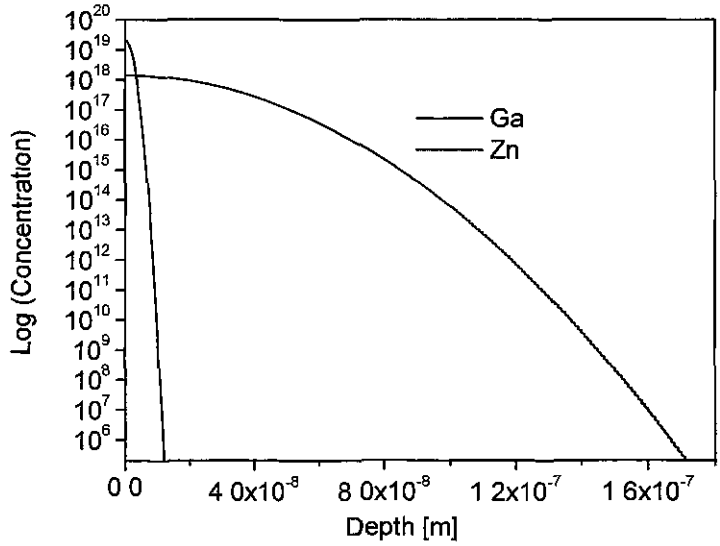

Figure 3.3: Plot of concentration vs. depth for Zn and Ga after annealing at 973 K

The laser penetration depth is of the order of 50 nm, therefore as can be seen from Fig. 3.3, the implanted atoms are distributed over a deeper distance than the laser light penetration depth.

3.3.2 Control Experiments

Implantation and annealing can cause many changes to the PL spectrum. In order to ensure that features found to correlate with the concentration of the mother/daughter isotope are not affected by either of these processes, a number of control experiments were undertaken. The first experiment performed involved annealing an untreated sample in order to see what effect this had on the PL spectrum; the second experiment involved implantation of stable isotopes of Zn and Ga in order to distinguish between features related to Ga and those due to implantation damage.

3.3.2.1 Annealing in an O_2 environment

An untreated sample was annealed at 800 °C for 30 minutes in an O_2 environment. Photoluminescence measurements were performed using the dispersive system at DCU. In Fig. 3.4 we see the band-edge luminescence spectra measured at 6.5 K. The upper spectrum, *A*, shows the luminescence before annealing while spectrum *B* shows the luminescence after annealing. As can be seen the effects of annealing are quite striking, resulting in a change in the relative intensity between several band-edge features. Annealing causes the disappearance of the broad feature at 3.3673(5) eV (labelled BX) and also the appearance of a feature at 3.3333(5) eV (labelled DD). The latter of these has been attributed to a deep donor and termed DD by Schildknecht *et al.* [14], in ZnO supplied by Eagle-Pitcher. Two-electron satellites (TES) of the donor bound excitons can be seen in both spectra. As we saw in Chapter 2, TES occur when recombination at a donor excites the donor from the 1s ground state to an excited state such as 2s or 2p. Because the linewidths of the donor bound excitons (DX) in these samples are broad, which leads to even broader TES, it isn't possible to relate each DX to its corresponding TES. However, this can be done in other samples were the DX lines are sharper and has been shown in Chapter 2. The energy separation of TES from their related DX is typically of the order of 30 meV. Assuming that the effective-mass model applies for the donor, the ionisation energy, E_D, for these donors should be $\sim 4\Delta E/3$, where ΔE is the energy difference between the energy of the DX and its corresponding TES. This gives ionisation energies of the order of 40 meV. The luminescence after annealing is approximately a factor of seven less than for the untreated sample.

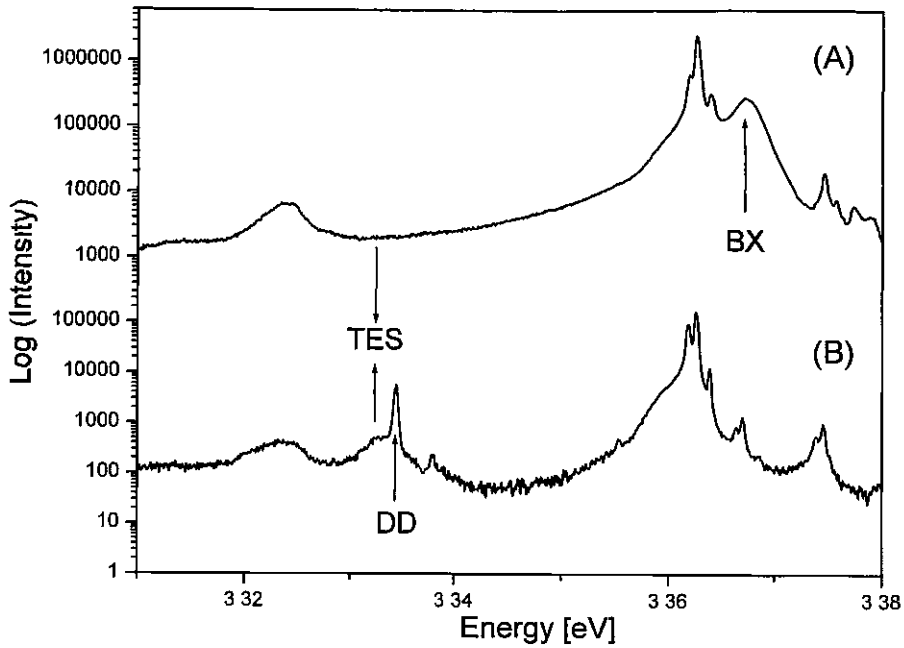

Figure 3.4. (A)-As-received Rubicon material; (B)-Annealed at 800 °C for 30 mins in 0.5 bar O_2. Both spectra are plotted on a log scale

PL spectra over a wider energy region, before and after annealing, are presented in Fig. 3.5. Annealing in an O_2 environment creates a structured green band, with an increase in the relative intensity of the green band in relation to band-edge luminescence. PL measurements, taken several days after the first measurement and anneal, show roughly the same results, implying that although the anneal does affect the intensities of PL features, the PL spectra remain the same whether measured directly after the anneal process or at a later date. During the measurements with radioactive isotopes, samples were kept below 77 K between scans which ensures that centres created by the annealing or the implantation process do not diffuse through the crystal between measurements.

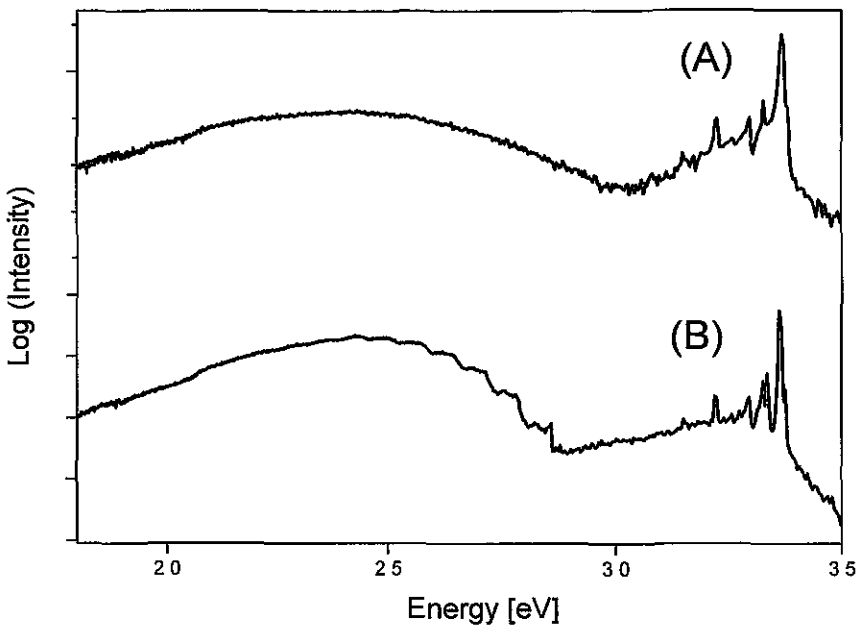

Figure 3 5· (A)-As-received Rubicon material; (B)-Annealed at 800 °C for 30 mins in 0.5 Bar O_2. Both spectra are plotted on a log scale

3.3.2.2 Stable implantations

Samples were implanted with stable isotopes of Zn and Ga in order to investigate both the implantation damage that results and the effects of annealing. The samples were annealed using the conditions described previously and were examined with the FT system in DCU. A liquid helium flow cryostat was used and the measurement temperature was 6 K. The implantation of Zn allows one to identify PL signals caused by implantation damage, whereas the Ga-implantation allowed us to decide on a suitable implantation dose for the radioactive implantations. The Zn-implanted sample has a feature at 3.3603(1) eV as its main peak, while the Ga-implanted sample has a peak at 3.3600(1) eV. The DD feature, mentioned above, is also seen in the Zn-implanted sample and the TES of the bound excitons can also be seen.

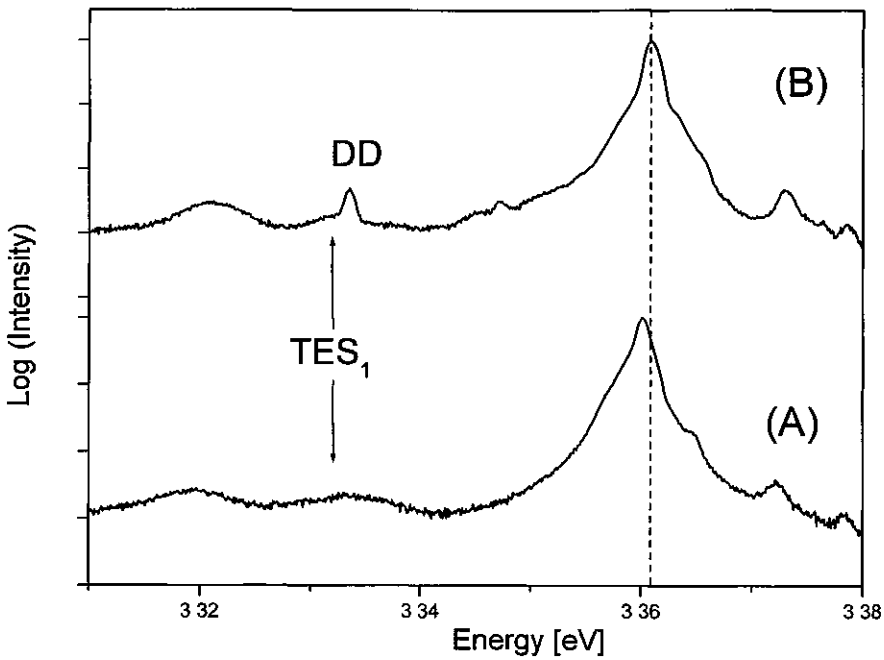

Figure 3.6: *Spectrum (A) shows a plot of Ga-implanted ZnO, Spectrum (B) is of Zn-implanted ZnO. Both spectra are plotted on a log scale*

3.3.3 Radioactive implantations

Radioactive isotopes of Zn and Ga were implanted into single crystal ZnO. The results of the ^{73}Ga implantation will be discussed first as the analysis of the PL spectra obtained in this case were easier to analyse than those obtained for the ^{72}Zn implantation due to significant levels of isobaric contamination in the ^{72}Zn beam.

^{73} Ga implantations

For the first experiment, ^{73}Ga was implanted into ZnO at the ISOLDE facility at CERN. Figure 3.7 shows the first photoluminescence spectrum obtained after annealing. The figure has a log-scale on the y-axis, with the upper spectrum, A, showing a magnified view of some of the lower intensity features, ranging in energy from 3.26 to 3.4 eV, while the lower spectrum, B, shows the donor bound exciton region.

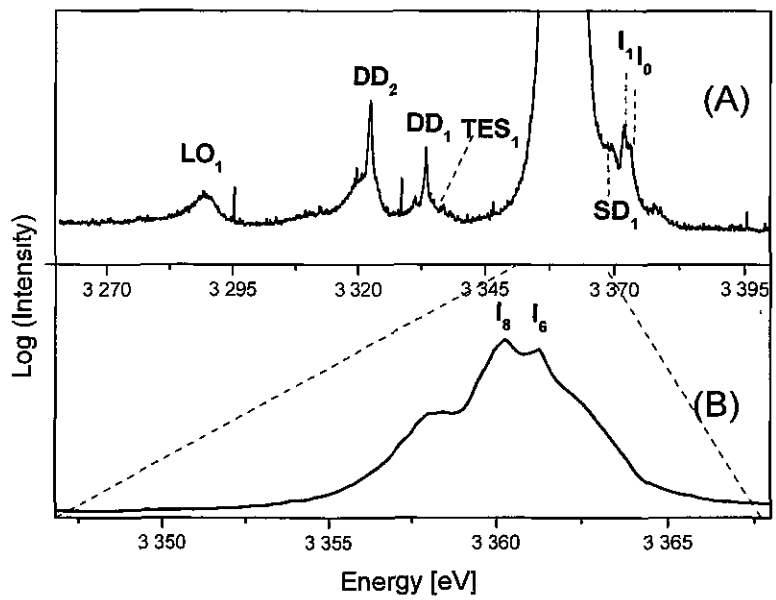

Figure 3.7: First scan after annealing ^{73}Ga implanted sample. Spectrum (A) shows some of the weaker emission signals observed in the near band-edge region, while spectrum (B) shows the most intense DX features

A summary of the features, observed in the photoluminescence spectra discussed in this chapter, is presented in table 3.1. A comparison of the features presented here and features reported in the literature is included in table 3.1.

Energy (eV)	Label	Identity	Reference
3.3783	A_L	Longitudinal A-free exciton state	TW, 9
3.3731	I_0	?	TW, 9
3.3718	I_1	Ga?	TW, 8, 9
3.3699	SD_1	?	TW
3.3628	I_4 (D^0_{1a})	H	TW, 8, 9, 14
3.3610	I_6	Al	TW, 8, 9
3.3600	I_8 (D^0_{2a})	Ga	TW, 9, 14
3.3580	SD_2	?	TW
3.3333	DD_1	?	TW, 14
3.3225	DD_2	Ge	TW

Table 3.1: Table listing some of the features observed in the Ga- and Zn-implanted samples. The label TW stands for "this work"

The intensity of all the PL features may change from scan to scan for a number of reasons; the integration time chosen for the CCD detection time can be changed, slight movements of the sample can occur as helium flows into the sample space and the background light over the course of the measurement may vary. For these reasons it is not always possible to analyse or show the effects of radioactive decay without some normalisation of the data. A baseline needs to be fitted, to remove the effect of dark counts readings from the CCD or changes in the ambient light intensity, and the data require normalisation to some stable sample signal [15]. Often, a phonon replica or the free exciton can be used to do this, provided the features of interest lie some distance in energy away from the reference peak.

As can be seen in Fig. 3.8, there is considerable variation in the intensity of all the band-edge features over the course of five half-lives; the y-axis scale is an indication of this. In Fig. 3.8 we see that as the implanted ^{73}Ga decays, there is a large change in the relative intensities of the I_6 and I_8 lines.

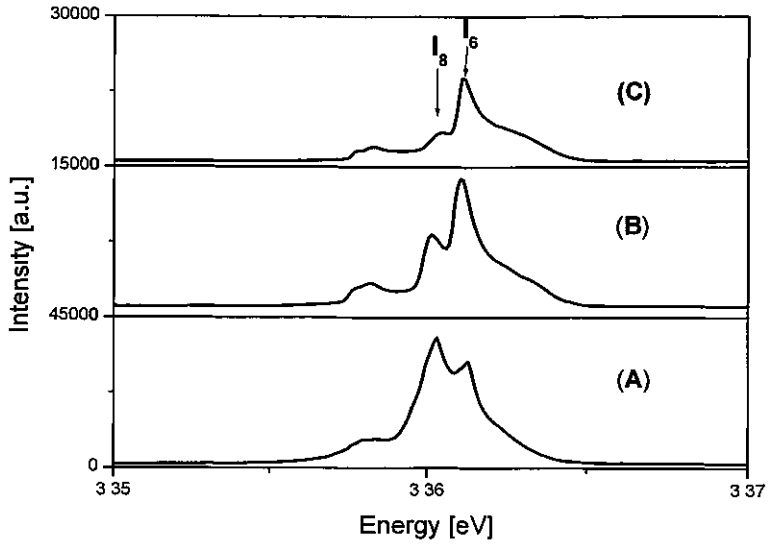

Figure 3.8: *Band-edge PL at 3.2 (A), 13.9 (B) and 24.3 (C) hours after annealing. These times correspond to 0.6, 3 and 5 times the half-life of ^{73}Ga*

Figure 3.9 shows the high energy side of the band-edge emission. Here, three features are highlighted; I_0, I_1 and a feature termed SD_1, indicating shallow donor. The first two features have been previously reported but the position of the last one does not correspond to any of the I_1 features reported previously.

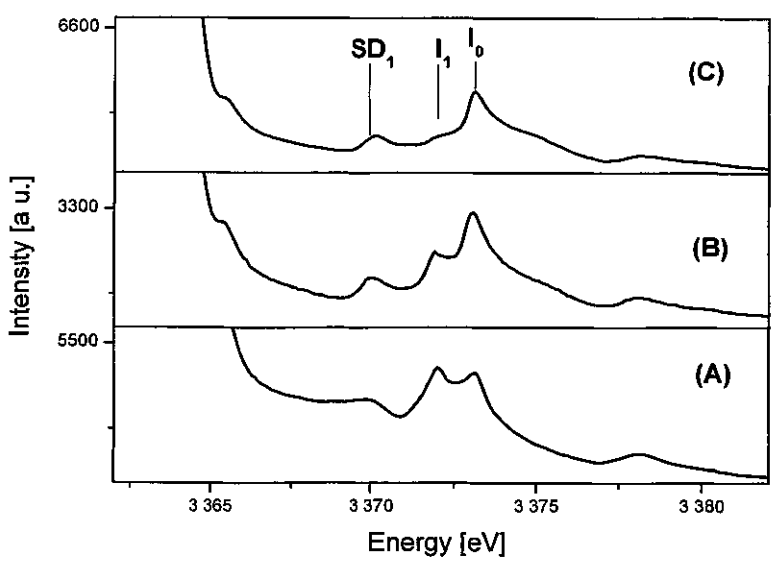

Figure 3.9: *High energy side of the DBE region at 5 (A), 13.9 (B) and 24.3 (C) hours after annealing*

Similar behaviour in Fig. 3.10 is seen between the ratio of the DD line at 3.3333(3) eV and the DD_2 line at 3.3225(3) eV. The DD_1 line appears to be the deep donor feature (DD), as mentioned previously [14], but the DD_2 appears to be a new feature. The DD_1 line lies on top of the TES (two-electron satellites) of the donor bound excitons. In Fig. 3.10 we see that for the DD_1 feature there is a maximum variation in the peak height of approximately 12%, while for the DD_2 feature the change in intensity is of the order of 40%.

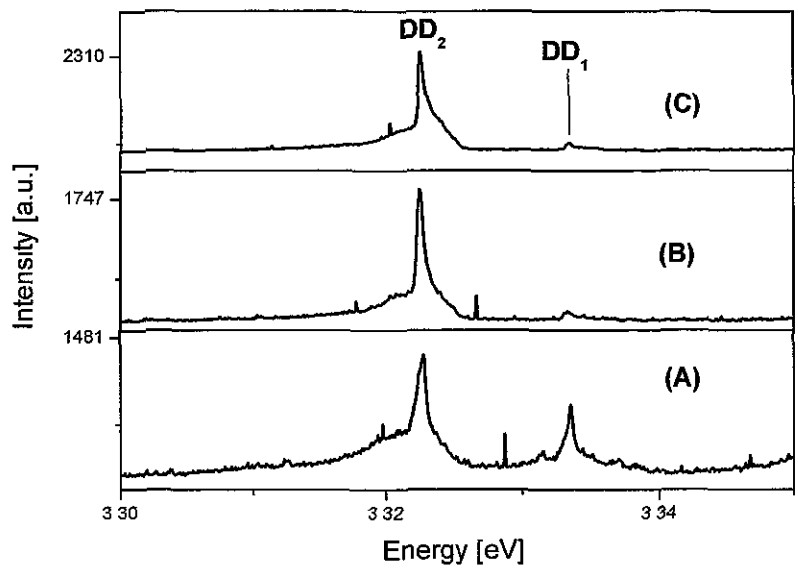

Figure 3.10: Deep donor PL region at 3.2 (A), 13.9 (B) and 24.3 (C) hours after annealing. The sharp peaks are caused by γ-rays created during the decay process

In order to check whether any of these changes correspond to the implanted radioactive atoms or the daughter product ^{73}Ge, it is necessary to see whether these change in intensity follow the half-life of the implanted isotope. Before this can be done, it is necessary to determine which signals remain constant and which are changing over five half-lives of the implanted species, i.e. to find a suitable normalisation. The integrated intensity of the DD_1 line was chosen to normalise the data as it lies away from the main features of interest and was found to remain fairly stable over the course of the measurements.

I_8 emission line

As the I_8 line is very close to the other band-edge features, the band-edge was fit as a composite of four Lorentzian lines, and the area was obtained using the formula:

$$y = y_0 + (\frac{2A}{\pi})(\frac{w}{4(x-x_c)^2 + w^2}) \qquad \textbf{3.3}$$

where y_0 is the offset, x_c is the peak, A is the area and w is the width of the line. Figure 3.11 shows the fit of four Lorentzian lines to the band-edge emission; the intensity of the I_8 line is then normalised by dividing the area, obtained from the fit, by the area of the DD_1 line.

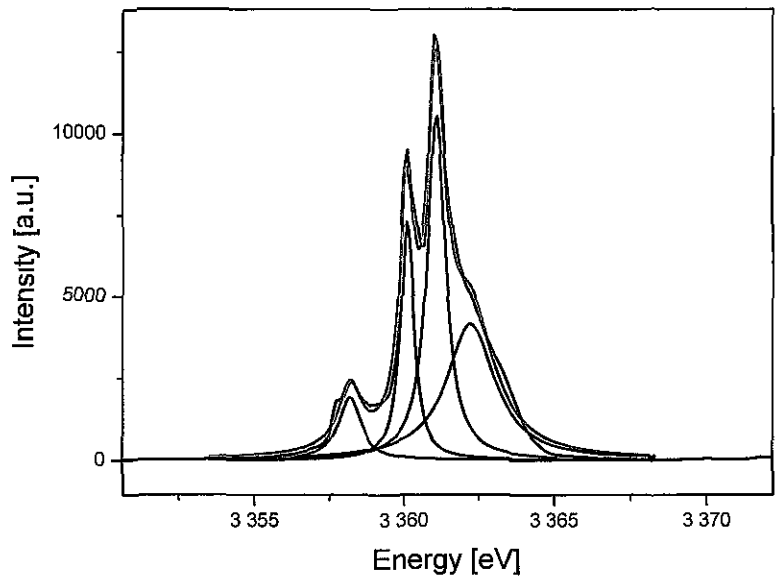

Figure 3.11: Fit of four Lorentzian lines to band-edge emission

Figure 3.12 shows the normalised intensity of the I_8 line measured as the ^{73}Ga decays. The intensity of the I_8 line is fit to the concentration of Ga using the equation:

$$N_{Ga} = y_0 + N_0 \exp^{-\lambda t} \qquad \textbf{3.4}$$

and

$$\lambda = \ln 2 / t_{1/2}$$

An offset, y_0, was included to account for the initial pre-implantation presence of Ga in the samples. A $t_{1/2}$ value of 4.88 ± 0.66 hours was obtained which compares favourably to the half-life of the Ga isotope of 4.87 hours.

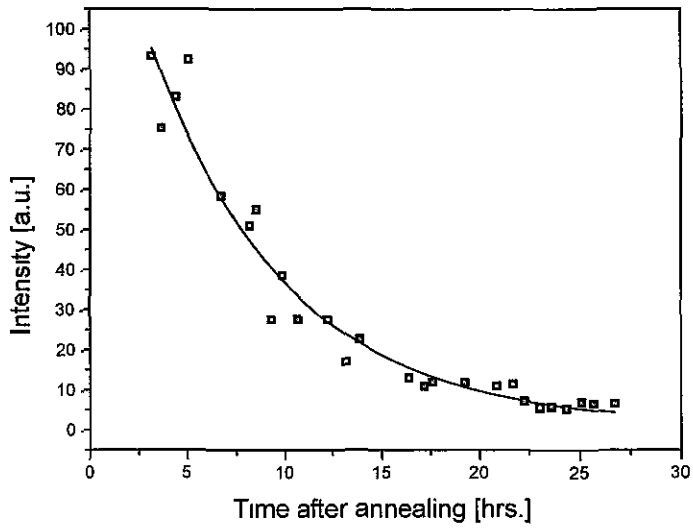

Figure 3.12: Plot of area under I_8 against time after annealing with an off-set included to account for some initial Ga concentration. The fit gives a value of 4.88 ± 0.66 hours for the half-life

DD_2 emission line

At the low energy side of the DX region, there appears to be a feature, termed the DD_2, line that increases in intensity as the concentration of Ga decreases in the sample. Figure 3.13 shows the change in the intensity of the DD_2 emission line measured against time after annealing. As the intensity of this feature increases with time, the involvement of the daughter isotope Ge is a strong possibility. The intensity of the DD_2 line, normalised by the integrated area of the DD_1 line, is fit to the concentration of Ge which is described by the following equation:

$$N_{Ge} = N_0(1-\exp^{-\lambda t}) \qquad \textbf{3.5}$$

$$\lambda = \ln 2 / t_{1/2}$$

Although there is a good deal of scatter in the data, a value of 5.76 ± 0.75 hours was obtained for the $t_{1/2}$ value in the fit, which compares reasonably well with the half-

life of ^{73}Ga (4.87 hours) and indicates that Ge is involved in the identity of this feature.

As discussed in Chapter 1, after decay the daughter isotope has a certain amount of recoil energy due to the mass difference between it and the mother isotope. If we assume that Ga substitutes for a Zn lattice site, it is reasonable to expect that Ge will also occupy a Zn site, due to the low recoil energy of the Ge isotope. With a valency of four, Ge substituting for Zn should act as a double donor. If this is the case, it would be the first incidence of a double donor reported for ZnO. However, other measurements are needed to support this hypothesis, for example electrical measurements such as Hall effect or DLTS.

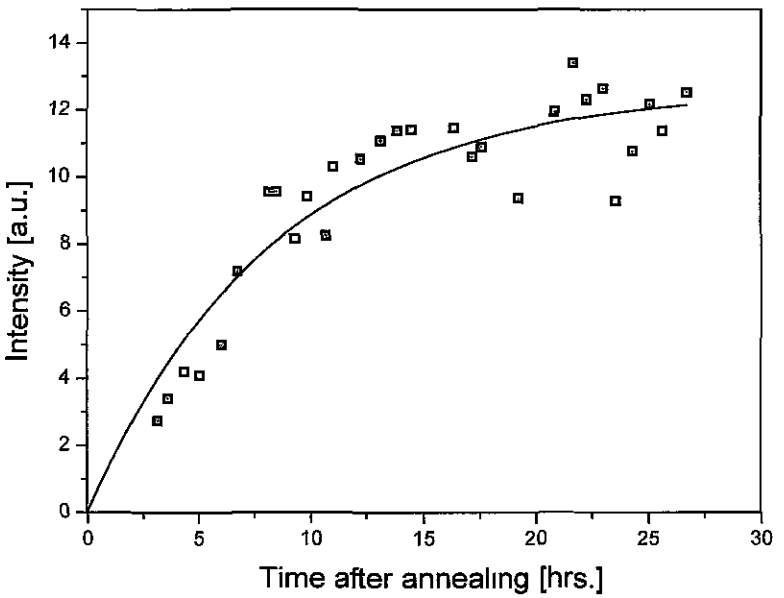

Figure 3.13: Plot of area under DD_2 against time after annealing. The fit gives a value of $t_{1/2}$ of 5.76 ± 0.75 hours

I_1 emission line

We now consider weaker lines in the PL spectrum which lie above the main DX lines. The intensity of the I_1 emission line was normalised with respect to the I_0 feature, which lies in the same spectral region. This normalised intensity was plotted against time after annealing, as shown in Fig. 3.14. This, along with the fit to equation 3.4, is shown in Fig. 3.14. A value of 4.78 ± 0.77 hours for $t_{1/2}$ was obtained. The range of values used to obtain this fit was less than was used for the I_8 emission line as it became more difficult to distinguish between the I_0 and I_1 features as the intensity of I_1 decreased.

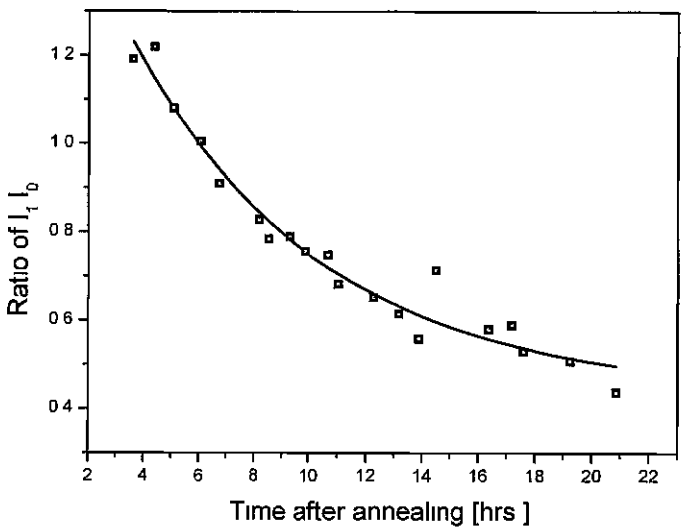

Figure 3.14. Ratio of heights of I_1:I_0. The entire data set could not be shown as it proved too difficult to separate out the two lines as the intensity of the I_1 feature dropped

The results above appear to suggest that I_1 is also Ga-related. The I_1 line could be due to recombination at an ionized Ga site. The energy position of this feature lies in a region where one expects to find ionized donor emission [16]. The I_2 and I_3 lines, at 3.3680 and 3.3671 eV, have been shown to be due to recombination at ionized donors through their behaviour in a magnetic field [8], and also, good correlation in terms of decay rates between I_1 and I_8 is observed. Ionized donors generally occur where there is a high concentration of acceptors. Annealing in an O_2 atmosphere creates Zn vacancies which act as acceptors in ZnO [17] and there is, even before annealing, a high concentration of acceptors in hydrothermally grown material due to

the presence of alkali metals such as Na, K and Li in the growth process [18-20]. Look *et al.* [21] measured an acceptor concentration of 1×10^{15} cm^{-3} and a donor concentration of 7×10^{15} cm^{-3} in hydrothermally grown ZnO in comparison to an acceptor concentration of 2×10^{15} cm^{-3} and 1×10^{17} cm^{-3} in SVP (Seeded Vapour Phase) grown material.

The identification of both I_8 and I_1 with Ga can be checked by studying their relative intensities; if both are due to Ga then we would expect their relative intensity to be constant. As can be seen in Fig. 3.15, normalising the intensity of the I_8 emission line to the I_1 line resulted in an almost linear decrease of intensity with respect to time after annealing. This casts doubt on the assignment of I_1 to Ga. It is possible, however, that the I_1 feature arises from excitonic recombination at some unidentified ionized donor. The decrease in intensity of I_1 could be related to a decrease in the acceptor concentration in the sample.

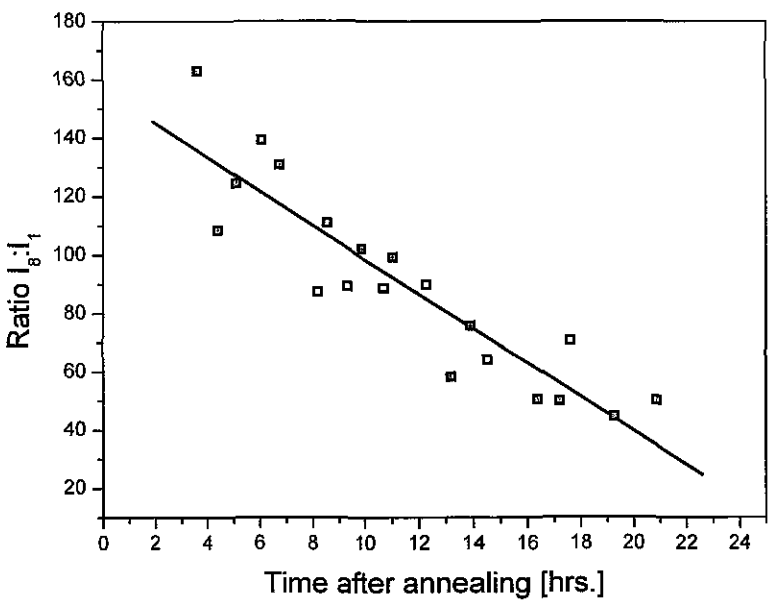

Figure 3.15: The ratio of I_8:I_1 is plotted against time after annealing.

As a further check, the intensity of the I_8 Ga-related bound exciton was normalised by the integrated intensity of the I_0 feature. This resulted in a spectrum showing an exponential decrease in intensity which could be correlated to the changing concentration of Ga in the sample. This is further confirmation that the exponentially decreasing signal for the I_8 feature seen in Fig. 3.12 is not due to the choice of normalisation. This is shown in Fig. 3.17, with a fit of 5.1 ± 0.34 hours obtained in comparison to the half-life of ^{73}Ga of 4.87 hours.

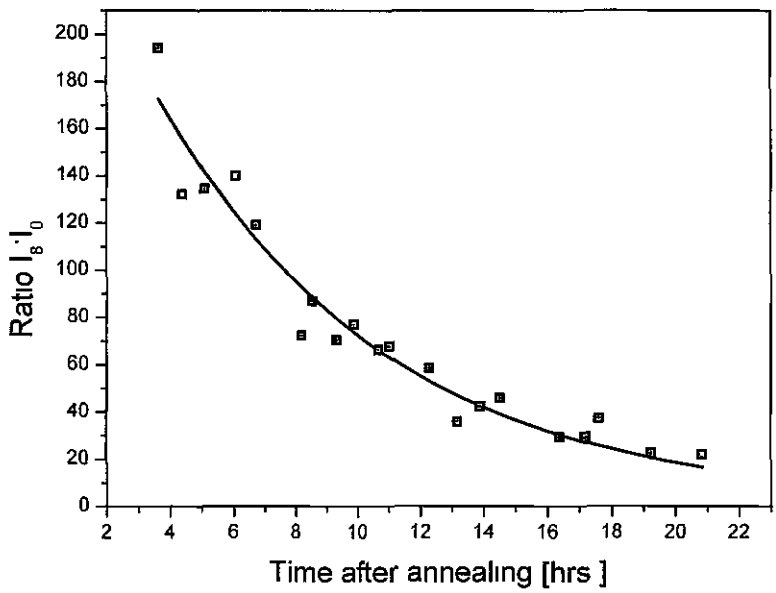

Figure 3.16: The ratio of $I_8 \cdot I_0$ is plotted against time after annealing. This produces a half-life value of 5.1± 0.34 hours in comparison to the ^{73}Ga half-life of 4.87 hours

^{72}Zn implantations

Further implantations with another radioactive isotope, ^{72}Zn, were performed at the ISOLDE facility to study the involvement of Ga in the DX lines. Figure 3.17 shows the PL features recorded at different stages of the decay of Zn→Ga→Ge. As can be seen the line marked *A* shows a clear decrease in intensity with time after annealing. The spectra have been offset for clarity.

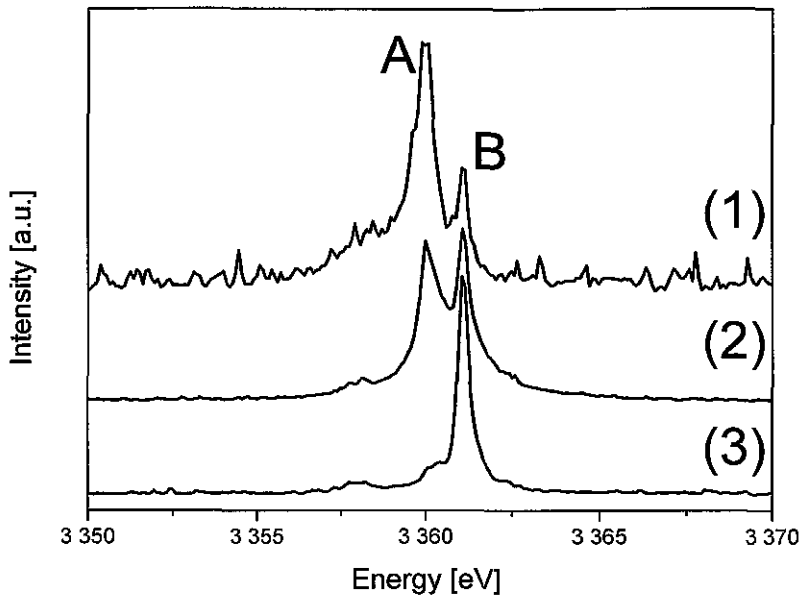

Figure 3.17: Spectra taken of the ^{72}Zn implanted sample (1) is 5.25 hours after implantation, (2) is 93 hours and (3) is 218.75 hours after implantation. The feature, labelled A, shows a clear decrease in intensity as the Ga concentration in the sample decreases

The ^{72}Zn implantations proved to be slightly more complicated to analyse as the daughter product ^{72}Ga is also unstable, and also as γ-spectroscopy measurements indicated that there was isobaric contamination of ^{72}Ga in the beam, with the ratio of Zn:Ga being 3.2:1 immediately after implantation. The relative concentrations, allowing for the beam contamination, of Ga, Zn and Ge are shown in Fig. 3.18.

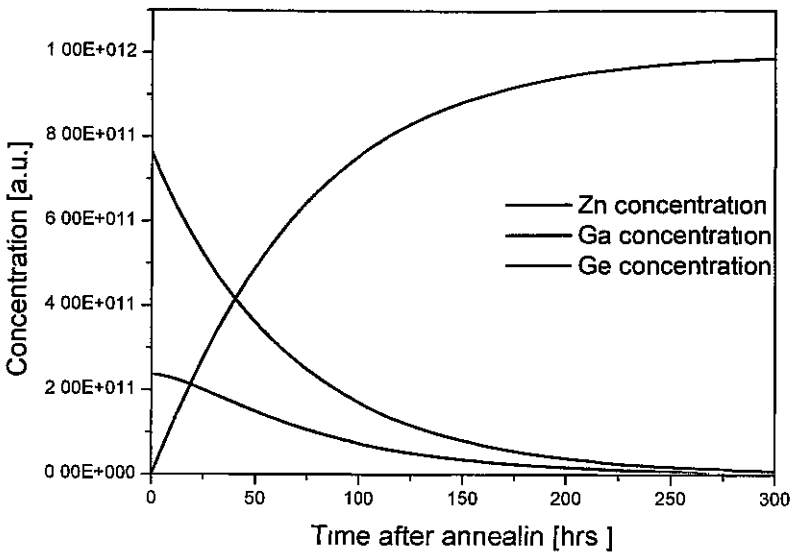

Figure 3.18: Concentrations of Zn, Ga and Ge atoms as a function of time, accounting for isobaric contamination in the beam.

The intensity of the I_8 line was fit using the equation:

$$Ga(t) = Ga(0)\exp^{-\lambda Ga t} + \frac{Zn(0)\lambda_{Zn}(\exp^{-\lambda Zn t} - \exp^{-\lambda Ga t})}{\lambda_{Ga} - \lambda_{Zn}} \qquad \textbf{3.6}$$

where Ga(t) is the concentration of ^{72}Ga at time t, Ga(0) and Zn(0) are zinc and gallium concentrations just after annealing, λ_{Ga} and λ_{Zn} are the decay constants of gallium and zinc. The fit constrained the initial concentrations of Zn and Ga so they were in the ratio of 3.2:1 and the value for λ_{Zn} was fixed at 0.015 hr^{-1}.

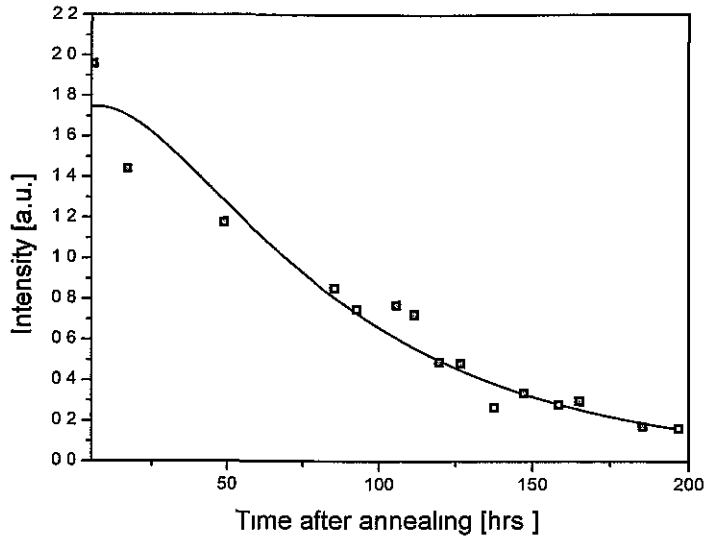

Figure 3.19: Fit to concentration of Ga including the effects of beam contamination. This gives a half-life of 19 9 ± 1.45 hours, in comparison to the half-life of the ^{72}Ga isotope of 14.1 hours

The fit to equation 3.6 gives a half-life of 19.9 ± 1.45 hours, in comparison to the half-life of the ^{72}Ga isotope of 14.1 hours. The contamination in the ^{72}Zn beam, along with the relatively poor signal to noise of the data taken, does lead to problems when fitting the data. This can be seen in the relatively poor fit to the half-life of ^{72}Ga. The data shown above in Fig. 3.19, however, support the association of the I_8 line with Ga, the conclusion drawn from the experiment with the ^{73}Ga-implanted sample.

Broad band luminescence from ^{72}Zn-implanted sample

The data and analysis described above focused on sharp line signals observed in the PL spectra. Another interesting feature in the luminescence spectrum of the sample implanted with ^{72}Zn is the appearance of a red band which grows throughout the measurements. If the recoil energy of the daughter product is comparable to, or greater than, the displacement energies of the host atoms, it is possible to see the effects of this damage. The creation of damage centres could lead to PL centres for which the changing intensity can match the radioactive decay rate of the radioactive isotope. The creation of a vacancy or an interstitial host atom could give an exponentially increasing signal (this can be seen here and also in the next chapter). On the other hand, the creation of such a defect could act as a luminescence killer,

compensating for a luminescence centre and resulting in an exponentially decaying signal. Table 3.2 shows recoil energies for the daughter products associated with the radioactive implantations discussed in this thesis.

Decay	Half-life ($t_{1/2}$)	Recoil energies (eV)		
		Average	Maximum	Q
$^{73}Ga \rightarrow {}^{73}Ge$, β-	4.87 hrs.	4.85	28.61	18.65
$^{72}Ga \rightarrow {}^{72}Ge$, β-	14.1 hrs.	5.72	98.80	118.72
$^{72}Zn \rightarrow {}^{72}Ga$, β-	1.93 days	0.71	2.92	1.56
$^{64}Cu \rightarrow {}^{64}Ni$, ec/ β+ $^{64}Cu \rightarrow {}^{64}Zn$, β-	12.7 hrs.	0.44	9.18	23.53
$^{67}Cu \rightarrow {}^{67}Zn$, β-	2.57 days	0.69	7.77	2.81
$^{65}Ni \rightarrow {}^{65}Cu$, β-	2.52 hrs.	1.33	7.40	2.67
$^{107}Cd \rightarrow {}^{107}Ag$, ec/ β+	6.5 hrs.	8.59	55.76	37.71
$^{7}Be \rightarrow {}^{7}Li$, ec/ β+	53.2 days	0.00	2.01	10.07

Table 3.2: Recoil energies for radioactive isotopes implanted in this work

The recoil energies for the isotopes of interest are as follows; 17.2 eV for the ^{73}Ge isotope, 1.6 eV for ^{72}Ga and 118.7 eV for ^{72}Ge. The displacement energies for ZnO are between 41 and 57 eV for an O-atom and 18.5 eV for a Zn-atom [22, 23]. Therefore, while signals caused by lattice damage are not expected in the sample implanted with ^{73}Ga, it is highly probable that such effects will be seen in the ^{72}Zn-implanted sample. As mentioned above, an increasing red band (peaking at 1.78 eV) is seen in the ^{72}Zn-implanted sample but not in the ^{73}Ga-implanted sample. This band is similar to one of the bands reported by Vlasenko *et al.* [24] after annealing electron-irradiated samples at 140 K. This band was attributed to some form of oxygen vacancy as it remains stable up to room temperature. Figure 3.20 shows the PL spectra obtained over a large energy range at (A) 5.25 hours, (B) 131.5 hours and (C) 218.75 hours after annealing. The data have been normalised to the most prominent DX emission line. The absorption features at 1.880 and 1.884 eV are believed to be Ni related [25].

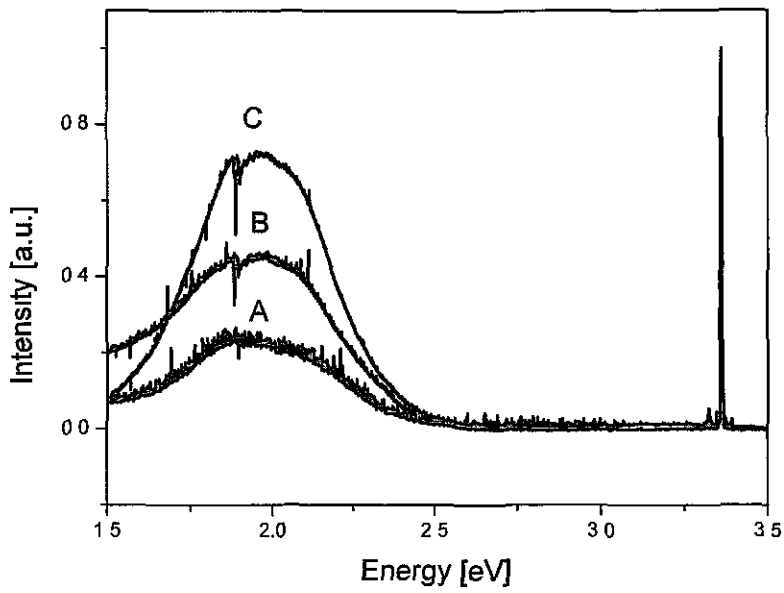

Figure 3.20: A-spectrum 5.25 hours after annealing; B-spectrum measured 131.5 hours after annealing and C-measured 218.75 hours after annealing. The absorption features at 1.880 and 1.884 eV are believed to be Ni related [26].

3.4 Conclusions

The I_8 line has been shown to be Ga-related due to the good correlation observed between the intensity of this feature and the concentration of Ga in the samples. The I_8 line is attributed to recombination at a neutral Ga centre as previous studies have shown that the I_8 is a neutral donor bound exciton [10]. The intensity of the I_1 feature was found to vary at a rate consistent with the changing concentration of Ga in the sample. However, as the intensity ratio I_8:I_1 was not constant as a function of time after annealing, there is some doubt whether this feature is also Ga-related. It is perhaps more likely that this emission line is due to recombination at some unidentified ionized donor.

A feature at 3.3225 (3) eV has been shown to follow the concentration of Ge in our samples. Due to the low recoil energy of the ^{73}Ge isotope, it is believed that the daughter product Ge should also take a Zn substitutional site. If this occurs, Ge should act as a double donor, donating two electrons to the conductivity. Further

measurements such as electrical measurements would be required to confirm this. If this is found to be true, the DD_2 line would be the first optical identifier of a double donor in ZnO.

A broad red band is found to grow in samples implanted with ^{72}Zn. This is believed to be a damage related band, created by the high recoil energy of the ^{72}Ge daughter product. This band appears to be the same as that reported by Vlasenko *et al.* [24].

References

1. B. M. Ataev, A. M. Bagamadova, A. M. Djabrailov, V. V. Mamedo, R. A. Rabadanov, Thin Solid Films, **260**, 19 (1995).
2. G. A. Hirata, J. McKittrick, T. Cheeks, J. M. Siqueiros, J. A. Diaz, O. Contreras, Thin Solid Films, **288**, 29 (1996).
3. Y. Imai, A. Watanabe, *J. Material Science: Materials in Electronics*, **15**, 743 (2004).
4. X. Yu, J. Ma, J. Feng, Y. Wang, X. Zhang, H. Ma, Appl. Surf. Sci., **239**, 222 (2005).
5. Hiroyuki Kato, Michihiro Sanoa, Kazuhiro Miyamotoa and Takafumi Yao, J.Cryst. Gr., **237-238,** 538 (2002).
6. H. J. Ko, Y. F. Chen, S. K. Hong, H. Wenisch, T. Yao and D. C. Look, Appl. Phys. Lett., **77**, 3761 (2000).
7. F. Reuss, C. Kirchner, Th. Gruber, R. Kling, S. Mascheck, G. Prinz, W. Limmer, A. Waag and P. Ziemann, J. Appl. Phys., **95**, 3385 (2004).
8. D. C. Reynolds, C. W. Litton and T. C. Collins, Phys. Rev., **140**, A1726 (1965).
9. B. K. Meyer, H. Alves, D. M. Hofmann, W. Kriegesis, D. Forster, F. Bertram, J. Christen, A. Hoffmann, M. Strassburg, M. Dworzak, U. Haboeck, A. V. Rodina, Phys. Stat. Sol. (b), **241**, 231 (2004).
10. M. Strassburg, A. Rodina, M. Dworzak, U. Haboeck, I. L. Krestnikov, A. Hoffmann, I. Gelhausen, M. R. Phillips, H. R. Alves, A. Zeuner, Phys. Stat. Sol. (b), **241**, 607 (2004).
11. U. Rössler, Landolt-Börstein Numerical Data and Functional Relationships in Science and Technology Group III: Condensed Matter B:II-VI and I-VII Compounds; Semimagnetic Compounds, (Springer Verlag, 1999, Berlin).

12. G. Davies, Semiconductors and Semimetals (Academic Press, 1999) Vol. 51B, Chapter Optical Measurements of Point Defects, 1-92.
13. S. M. Sze, Semiconductor devices, physics and technology, 2nd edition (Wiley, New York, 2002), chapter 13.
14. A. Schildknecht, R. Sauer, K. Thonke, Physica B, **340-342**, 205 (2003).
15. Th. Agne, M. Dietrich, J. Hamann, S. Lany, H. Wolf, Th. Wichert, and the ISOLDE Colloboration, Appl. Phys. Lett., **82**, 3448 (2003).
16. C. F. Klingshirn, Semiconductor Optics, 2nd edition (Springer, London, Berlin, 2005), Chapter 9.
17. A. F. Kohan, G. Ceder, D. Morgan, Chris G. Van de Walle, Phys. Rev. B, **61**, 15019 (2000).
18. T. Sekiguchi, S. Miyashita, K. Obaro, T. Shishido, N. Sakagami, J. Crys. Gr., **214/215**, 72 (2000).
19. M. Suscavage, M. Harris, D. Bliss, P. Yip, S. –Q. Wang, D. Schwall, L. Bouthillette, J. Bailey, M. Callahan, D. C. Look, D. C. Reynolds, R. L. Jones, C. W. Litton, MRS Internet J. Nitride Semicond. Res., 4S1, G3.40 (1999).
20. I. Sakaguchi, S. Hishita, Surf. Interface Anal., **36**, 645 (2004).
21. D. C. Look, Mat. Sci. and Eng. B, **80**, 383 (2001).
22. D. C. Look, J. W. Hemsky and J. R. Sizelove, Phys. Rev. Lett., **82**, 2552 (1999).
23. J. A. V. Vechten, Handbook on semiconductors (North-Holland, Amsterdam, 1980), Chapter 1.
24. L. S. Vlasenko, G. D. Watkins, Phys. Rev. B, **71**, 125210 (2005).
25. R. S. Anderson, Phys. Rev., **164**, 398 (1967).

Chapter 4: Study of the green band in ZnO

4.1 Introduction

One of the most common features in the PL spectra of ZnO is the "so-called" green band. It occurs so frequently that the ratio between the UV emission and the green band luminescence is often used as an indicator of sample quality. Although it is not always clarified in the literature, there are at least two broad bands in this region that are designated "green" bands. One of the reasons for this may be due to the fact that low temperatures, i.e. below 140 K, are needed to see the structured band clearly [1-3], and many studies of the green band involve room temperature measurements. One of these bands is highly structured, consisting of broad peaks separated by the ZnO LO phonon energy of ~73 meV, with the band peaking at 510 nm (2.43 eV); the other is unstructured and peaks at ~ 500 nm (2.48 eV). Each of these bands could have quite different origins; however, some authors believe that they are related and are caused by different charge states of the same defect [1]. Figure 4.1 illustrates the two different bands.

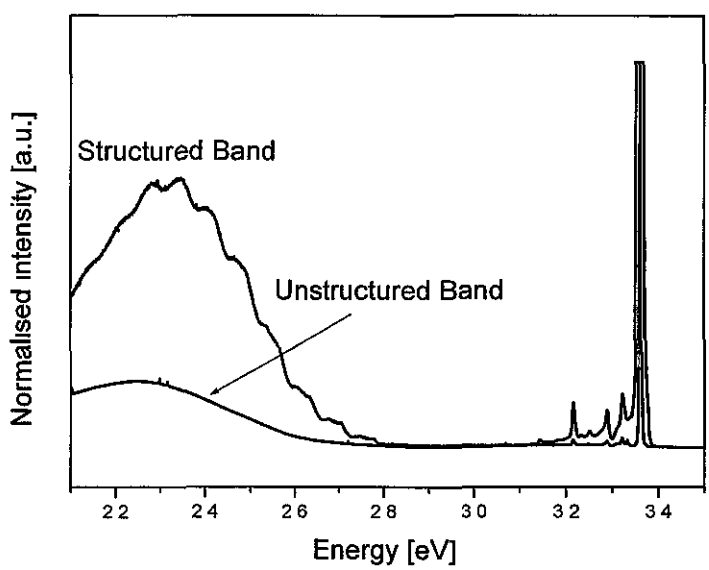

Figure 4.1: PL spectra showing two different green bands. The structured band is observed in a sample that has been implanted and annealed. The other spectrum is from an untreated sample

The first in-depth study of the structured green band was performed by Dingle [4]. In that work, a feature close to the band at ~2.859 eV was found to consist of two

distinct lines, separated by approximately 0.11 meV. The intensity ratio between the two lines was 2.25 ± 0.05. This ratio remained constant as the temperature was raised from 1.6 K to 20.4 K. Zeeman measurements on each emission feature demonstrated matching splitting patterns, with the intensity ratio remaining constant as the magnetic field was increased. The samples measured by Dingle were known to contain 4 ± 2 ppm of Cu impurities, and as the natural abundance of ^{63}Cu:^{65}Cu closely matches this ratio (2.24:1); the band was attributed to Cu^{2+}. The EPR signals obtained were similar, but not identical, to those obtained through EPR measurements for Cu^{2+}. From this evidence the doublet was believed to be caused by different isotopes of Cu. Three lines were found in the photoluminescence excitation measurements on the green band in ZnO [5]. One of these features, known as the α line, was found to coincide with the ZPL line seen in PL spectra. This line and another were found to consist of doublets, separated by 0.15 ± 0.01 meV; the other peak was much broader, with a FWHM of 0.67 meV, thus obscuring any possible observation of isotope splitting.

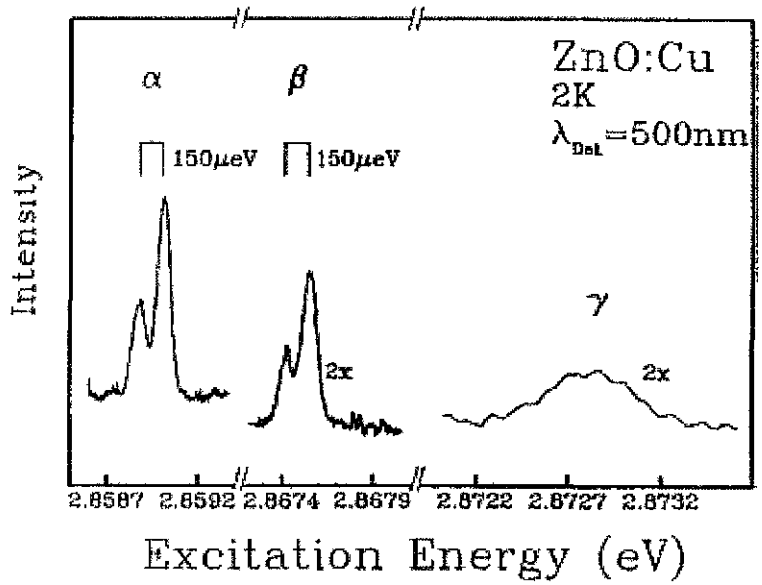

Figure 4.2: Excitation spectrum of green band as presented in [5]

Later studies of the structured green band favoured intrinsic defects due to the prevalence of this feature in ZnO, and also because this band was observed in ZnO that did not have an intentional or significant Cu concentration [6]. Studies of the stoichiometry of ZnO always show that Zn is in excess, independent of growth technique, leading to the belief that there is likely to be an appreciable concentration

of O-vacancies. The persistent n-type conductivity of ZnO was also believed to be caused by a shallow O-vacancy. For these reasons, the O-vacancy became widely considered to be the cause of the green band. Experimental measurements confirmed that good correlation could be obtained between PL measurements of the intensity of the band and an EPR signal of g = 1.96 [7] which was mistakenly attributed to a singly ionized O-vacancy. (The oxygen vacancy has the following EPR signals: $g_{\perp}$ is 1.9960 and $g_{//}$ is 1.9945, while the EPR signal of g = 1.96 is due to shallow donors.) Studeniken *et al.* [8] observed green band luminescence in oxygen deficient samples after annealing in a forming gas reducing atmosphere. The intensity of the band could be correlated with the annealing temperature, and therefore the band was attributed to oxygen vacancies. However, as the PL measurements in that work were taken at high temperature, it is unclear which of the green bands that work refers to.

The Zn-vacancy was also proposed as a candidate for the origin of the green band by several workers. LDA calculations performed by Kohan *et al.* [9] showed that a transition between the -1 and -2 charge states of the Zn vacancy occurs at 0.8 eV. A transition from an electron in the conduction band to this level should result in transition around 2.6 eV. Reynolds *et al.* [6] developed a model involving transitions between two shallow donors and a deep acceptor which could successfully model the structure of the band in the range 2.3 to 2.9 eV. The energies of the shallow donors were found to match the D1 and D2 donors which are observed in Hall-effect measurements. These donors have energies 30 and 60 meV below the conduction band edge. As the green band is similar to the yellow band seen in GaN, which has been shown to be transitions between a Ga-vacancy (acceptor) and Cl (donor), the acceptor in the model was suggested to be some form of Zn-vacancy.

In order to resolve the question as to whether Cu is involved in the green band, it was decided to undertake a study using radioactive isotopes. Two isotopes were implanted: ^{67}Cu which decays to ^{67}Zn, and ^{65}Ni which decays to ^{65}Cu. Colleagues at Saarbrucken implanted ^{64}Cu which decays by electron capture and β+ decay to ^{64}Ni and by β- decay to ^{64}Zn. (This work was performed as part of the ISOLDE Collaboration.) This selection would allow for both increasing and decreasing Cu concentration and should in principal provide conclusive evidence on the matter.

4.2 Experiment Description

Implantations of ^{65}Ni and ^{67}Cu were performed at the ISOLDE (Isotope Separator On-Line) facility at CERN, Switzerland. Approximately 1×10^{12} atoms were implanted for the two experiments. The samples were annealed in an oxygen atmosphere of 0.5 bar at 700°C for 30 minutes in order to remove implantation damage and spectra were taken on-site at CERN with the system described in Chapter 2. Measurements were made over the course of five or six half-lives of the implanted species. The samples were kept below 77 K between scans in order to prevent diffusion of the dopant atoms and spectra were taken with the samples at 1.6 K.

For the implantations, a 2×2 mm^2 collimator was used. TRIM calculations show an implantation range of approximately 70 Å leading to a concentration of approximately 3.6×10^{18} cm^{-3}. Using the diffusion coefficients of Cu [10], the diffusion coefficients of Ni in ZnO being as yet undetermined, the concentration profile of the implanted Cu ions after annealing was calculated and is shown in Fig. 4.3.

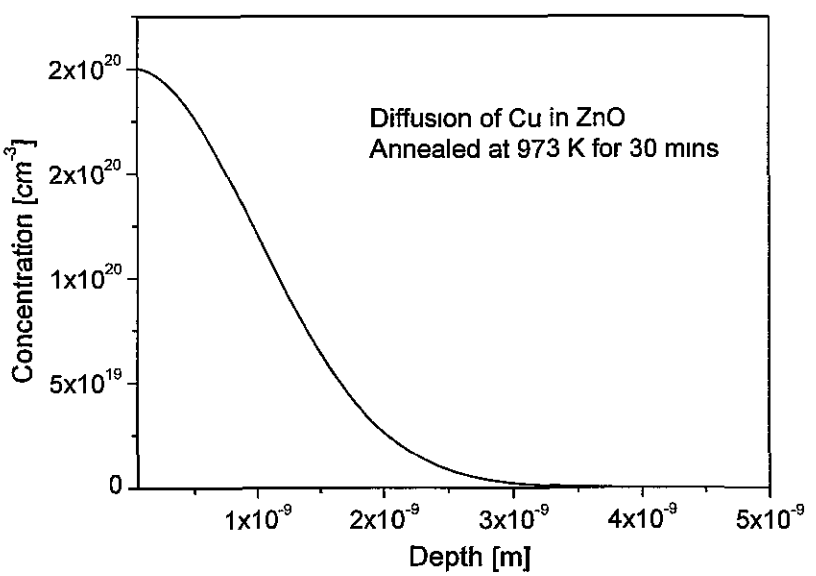

Figure 4.3: Plot of concentration vs. depth for Cu-implanted sample annealed at 973 K

4.3 Results

4.3.1 Implantation of ^{65}Ni

^{65}Ni, which decays to ^{65}Cu with a half-life of 2.52 hours, was implanted into ZnO and PL spectra were recorded at regular intervals for a number of half-lives of the implanted species. In order to correct for slight changes in sample alignment over the course of the measurements, each PL spectrum was normalised by dividing the data by the intensity of an LO-phonon replica of the band-edge. Figure 4.4 shows the spectra obtained after this normalisation process.

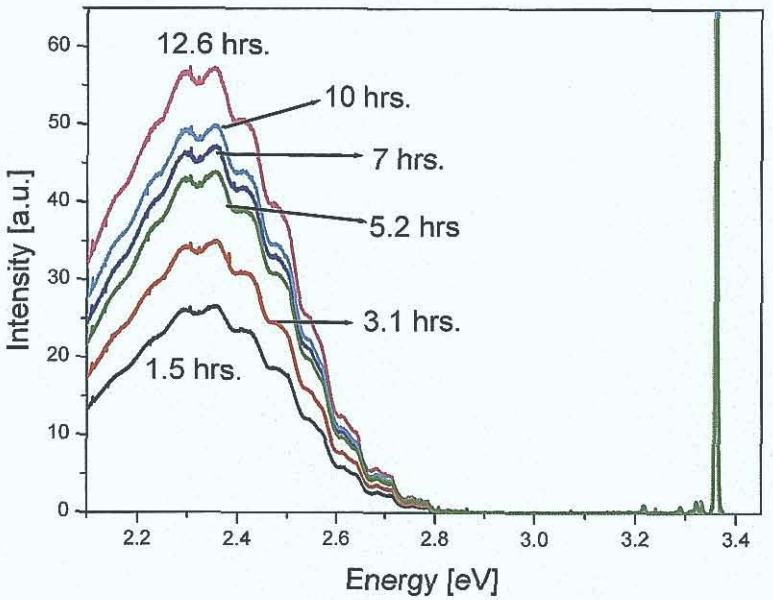

Figure 4.4: PL spectra of ^{65}Ni-implanted ZnO measured 1.5, 3.1, 5.2, 7, 10 and 12.6 hours after annealing

The intensity of the green band was then calculated by integration over a range from 2.883 to 2.294 eV. This intensity was plotted against time after annealing and a first-order exponential increase function was used to fit the data;

$$y = y_0 + A(1 - \exp^{-\lambda t}) \qquad \lambda = \ln 2 / t_{1/2} \qquad \textbf{4.1}$$

The fit to the data is plotted in Fig. 4.5 and produced a half-life value of 3.4 ± 1.5 hours in comparison to the half-life of ^{65}Ni of 2.5 hours. It was necessary to include

an off-set to the fitting function as there was a green unstructured band present in the PL spectrum of the samples prior to the implantation.

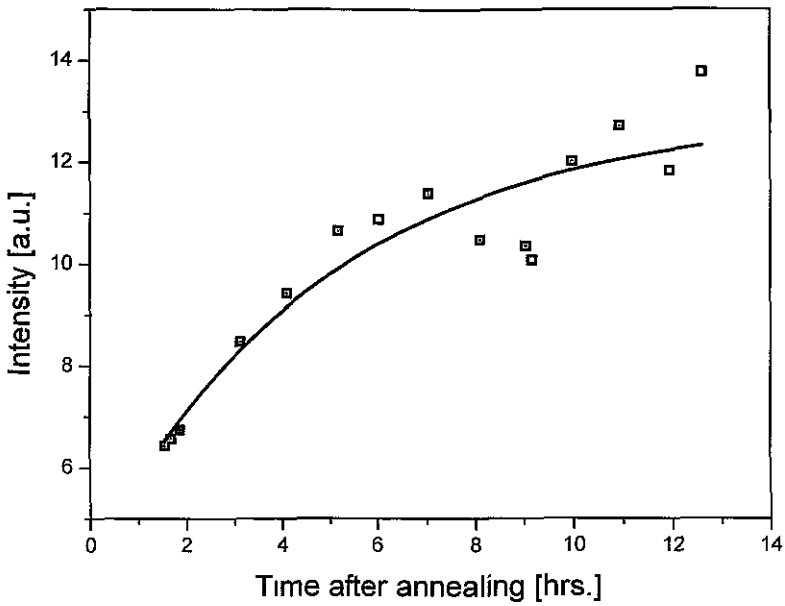

Figure 4.5: Fit to the exponential growth of the green band for the sample implanted with ^{65}Ni. This gives a fit of 3.4 ± 1.5 hours in comparison to the half-life of ^{65}Ni of 2.5 hours

These data point to the involvement of Cu as the cause of the green band. However, the results of the Cu implantations, discussed in the following two sections, lend doubt to this assignment.

4.3.2 Cu implantations

^{67}Cu, which decays to ^{67}Zn with a half-life of 2.57 days, was implanted into ZnO. No structured green band was found in this sample after implantation as is shown in Fig. 4.6. The intensity of the band did not change as the concentration of Cu decreased, suggesting that Cu is not involved in the green band.

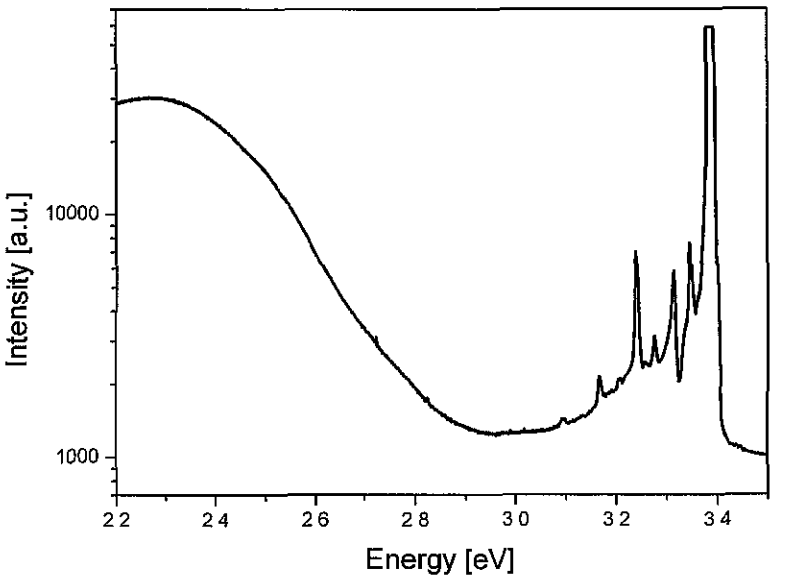

Figure 4.6: PL spectrum of ZnO implanted with ^{67}Cu. No structured green band is observed in this sample

As part of the ISOLDE Collaboration, implantations of ^{64}Cu, which decays by electron capture and β+ decay to ^{64}Ni and β- decay to ^{64}Zn with a half-life of 12.7 hours, were performed by Dr. T. Agne of Saarbrucken. His results showed an increasing green band that matched the half-life of ^{64}Cu decay [11]. Figure 4.7 shows the PL spectra obtained at various times after annealing, while the inset shows the fit obtained to equation 4.1.

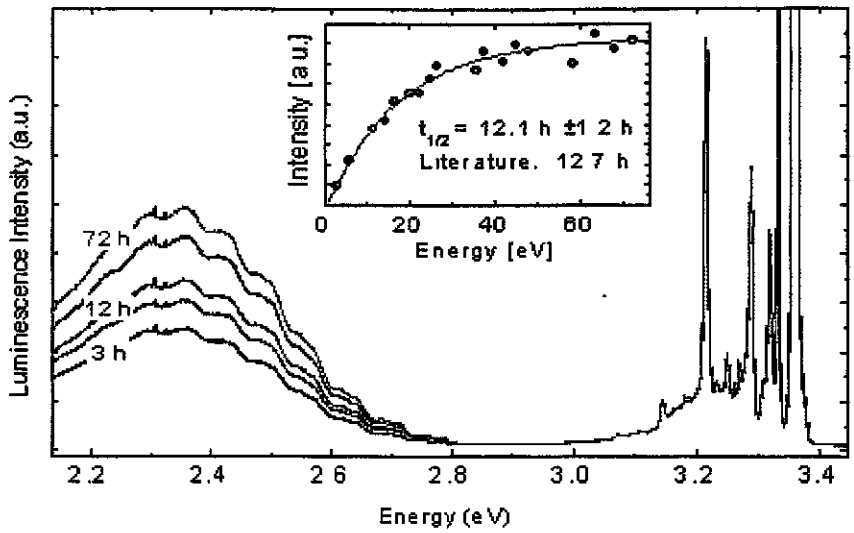

Figure 4 7: *PL spectra of ^{64}Cu-implanted sample measured at various times after annealing. The inset shows the fit to an exponential increase leading to a value of 12.1 ± 1.2 hours, in comparison to the $t_{1/2}$ of the Cu isotope of 12.7 hours [11]*

4.4 Discussion

As we have seen from the results presented above the green band does not appear to be related to either Cu or Ni. One of the possible explanations for the observation of a feature that increases with the half-life of the implanted isotopes that cannot be attributed to any of the daughter products is the creation of damage as a result of the decay process. The maximum recoil energies of the daughter products are 2.7, 37.7 and 23.5 eV for the decay of ^{67}Cu, ^{65}Ni and ^{64}Cu respectively. As the displacement energies for the host atoms in ZnO are 45 eV for an O-atom and 18 eV for a Zn-atom [12, 13], it can be seen that the cases where we see a structured green band involve the implantation of an isotope whose decay process causes a high recoil energy which is sufficient to displace a Zn-atom but not an O-atom. Therefore, these results support the conclusion that the green band is related to the creation of Zn-vacancies rather than oxygen vacancies.

Theoretical studies have shown that Zn-vacancies are easily formed in an O_2 rich environment [9]. Therefore, annealing in an O_2 environment should create Zn-vacancies. As can be seen in Fig. 4.8, annealing in an O_2 environment does produce

a structured green band, which also supports the assignment of the band to Zn-vacancies.

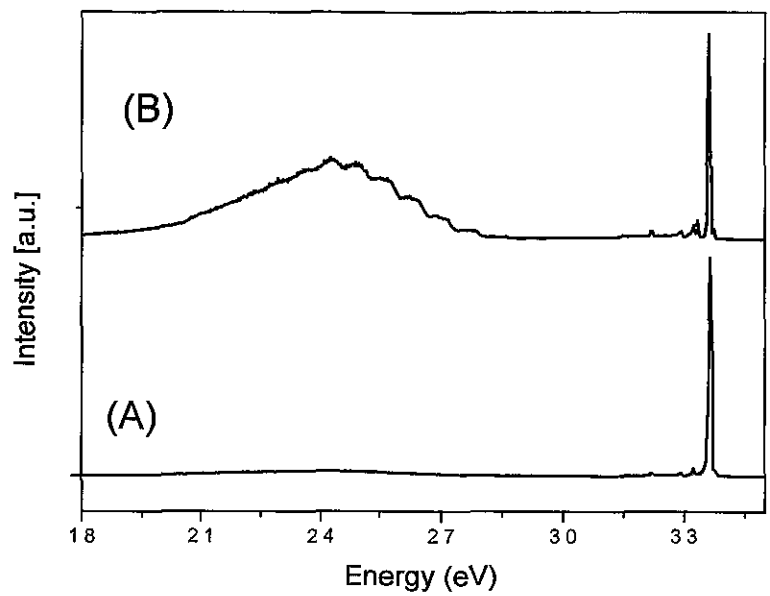

Figure 4.8: *(A) As received material, (B) Annealed at 800 °C for 30 mins. in an O_2 atmosphere*

The appearance of an isotope effect in the ZPL region of the green band in [4] is very strong evidence for the involvement of Cu in the structured band. Our data, however, do not agree with this work. The resolution of the spectra presented in this work was insufficient to resolve the ZPL, and therefore any isotope effect was impossible to detect. This can be seen in Fig. 4.9 with spectrum (1) showing the ZPL region, and spectrum (2) showing an enlarged section of spectrum (1). The energy positions where Dingle [4] observed the two ZPL lines are indicated with arrows in spectrum (2).

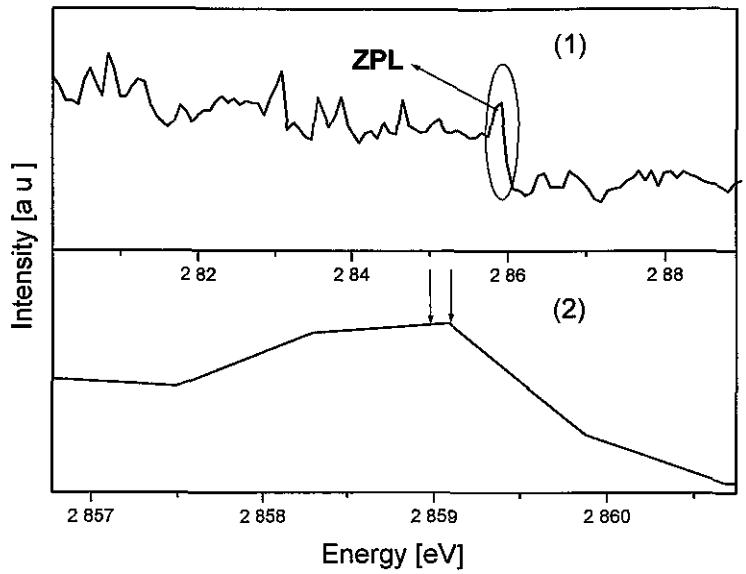

Figure 4.9: *Spectra showing the ZPL region. Spectrum (2) shows the magnified area indicated with a black circle in spectrum (1). The arrows in spectrum (2) represent the energies at which Dingle observed two emission lines which he attributed to recombination at different isotopes of Cu*

One of the possibilities which could reconcile our work with [4] is the existence of some underlying band, perhaps the unstructured band depicted in Fig. 4.1, which is affected by displacement of Zn-atoms.

A number of checks were performed in order to examine whether it is the structured green band that is increasing with the half-life of the implanted species, or some underlying band. Firstly, it was necessary to determine whether the change from one scan to the next consisted of a structured band or not. To do this, each plot was subtracted from the one preceding it and the result is shown in Fig. 4.10. This was done only for the ^{65}Ni data. As can be seen, all except one plot show a structured green band. Some of the plots are negative, indicating a decrease in green band intensity with increasing time after annealing. These are also seen as outliers in Fig. 4.4. In general, however, the green band appears to be increasing and structured, showing that the creation of Zn-vacancies lead to an increase in this structured band.

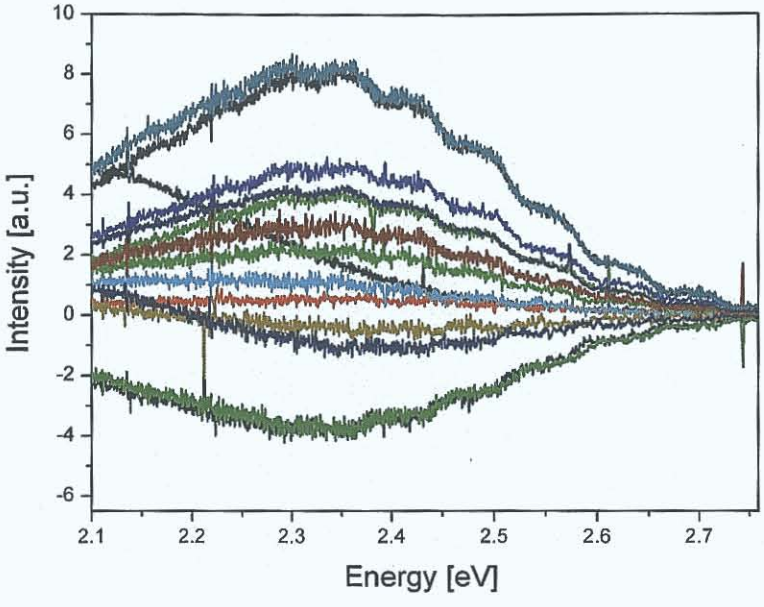

Figure 4.10: Effect of subtracting each spectrum from the previous one for the spectra obtained for the ^{65}Ni-implanted sample

The intensities of several of the phonon replicas were recorded for each spectrum. These were then plotted against time after annealing and the data were fit using the same function as used in Fig. 4.4. The variation of each phonon height as a function of time after annealing is shown in Fig. 4.11, while the half-life values obtained for each is shown in Table 4.1. Although the half-life values are increasing as one moves to lower energy, all the data show half-life values that lie within the uncertainty of the highest value. This trend of increasing half-life is not seen with the ^{64}Cu-implanted sample. Therefore, from this data it looks like the entire band is changing at the same rate, indicating that it is the structured band as a whole that is changing.

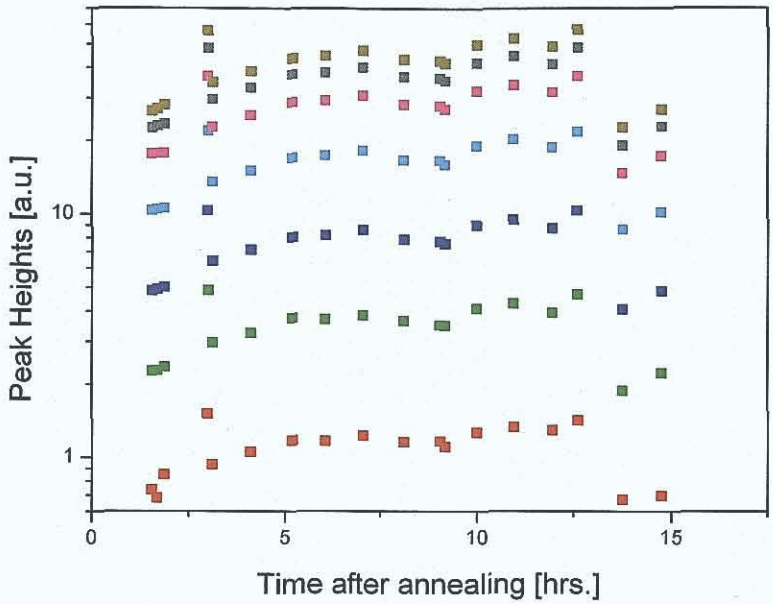

Figure 4.11: Plot of change in phonon height against time after annealing

Peak Position (eV)	$t_{1/2}$	uncertainty	R^2
2.776	2.66	0.95	0.9
2.715	2.86	1.2	0.87
2.641	2.95	1.26	0.87
2.569	3.06	1.29	0.88
2.501	3.15	1.37	0.87
2.434	3.29	1.46	0.87
2.359	3.78	1.83	0.88

Table 4.1: Fit to exponential increase for each phonon height

4.5 Conclusions

Radioactive implantations of ^{65}Ni, ^{67}Cu and ^{64}Cu were performed. It was found that while no change was observed in the green band intensity in the sample implanted with ^{67}Cu, a structured green band was found to increase in the other two samples. These results can be explained by the large recoil energies of the daughter isotopes in the cases where the green band was found to increase. The range of recoil energies of the daughter products suggest that it is the Zn-vacancy rather than the O-vacancy that is the cause of the green band.

From our data, it appears likely that it is the structured green band that is changing rather than some underlying band. This experiment will be repeated and high resolution spectra of the ZPL will be taken in order to check whether this feature follows the concentration of Cu and/or the intensity of the rest of the band.

References

1. N. Y. Garces, L. Wang, L. Bai, N. C. Giles, L. E. Halliburton, Appl. Phys. Lett., **81**, 622 (2002).
2. T. Monteiro, C. Boemare, M. J. Soares, E. Rita, E. Alves, J . Appl. Phys., **93**, 8995 (2003).
3. S. L. Shi, G. Q. Li, S. J. Xu, Y. Zhao, G. H. Chen, J. Phys. Chem. B, **110**, 10475 (2006).
4. R. Dingle, Phys. Rev. Lett., **23**, 579 (1969).
5. P. Dahan , V. Fleurov, P. Thurian, R. Heitz, A. Hoffmann, I. Broser, Phys. Rev. B, **57**, 9690 (1998).
6. D. C. Reynolds, D. C. Look, B. Jogai, J. Appl. Phys., **89**, 6189 (2001).
7. K. Vanheusden, W. L. Warren, C. H. Seager, D. R. Tallant, J. A. Voigt, J. Appl. Phys., **79**, 7983 (1996).
8. S. A. Studeniken, N. Golego, M. Cocivera, J. Appl. Phys., **84**, 2287 (1998).
9. A. F. Kohan, G. Ceder, D. Morgan, C. G. Van de Walle, Phys. Rev. B, **61**, 15019 (2000).
10. G. Müller, R. Helbig, J. Phys. Chem. Solids, **32**, 1971 (1971).
11. T. Agne, private communication.

12. J. A. V. Vechten, Handbook on semiconductors (North-Holland, Amsterdam, 1980), Chapter 1.
13. D. C. Look, J. W. Hemsky and J. R. Sizelove, Phys. Rev. Lett., **82**, 2552 (1999).

Chapter 5: Study of signals in the near IR and Red region in the PL of ZnO

5.1 Introduction

Doping semiconductors with transition metals leads to the creation of deep levels, which can act as lifetime killers for devices and compensate shallower levels. Transition metals can take on different charge states, and therefore, they can have many different levels within the band-gap between which there can be a variety of transitions. In the range 1.6 to 1.9 eV, PL studies of ZnO show at least three signatures of transition metals. Figure 5.1 shows a typical PL spectrum of Li-doped Rubicon samples using the 532 nm line of a frequency-doubled Nd:YAG as an excitation source. The spectrum consists of a broad band with sharp lines superimposed on this band. There is also a characteristic absorption feature in the region of 1.88 eV, attributed to a transition from a Ni^{2+} ion, which appears in all the Rubicon samples. An emission line related to the zero phonon line (ZPL) of an Fe^{3+} defect can be observed as well as sharp ZPLs that have not, as yet, been reported in the literature. These are labelled L1 and L3 in Fig. 7.1. We now consider these various spectral features in greater detail.

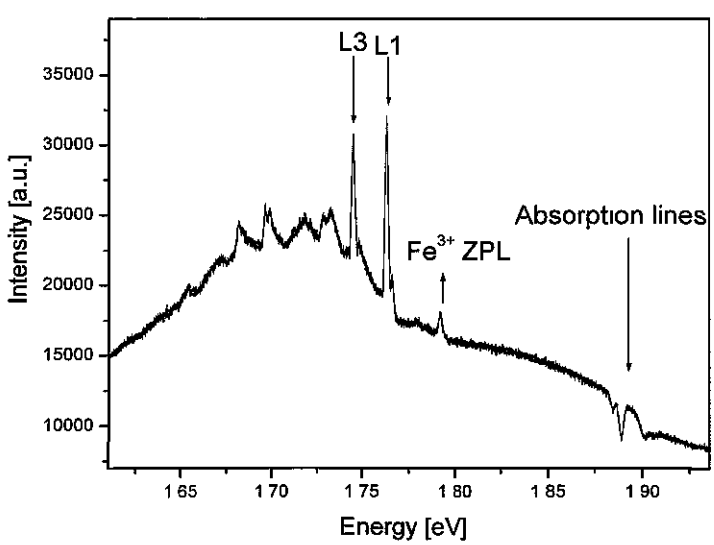

Figure 5.1: PL excited by 532 nm line of Nd:YAG laser

5.2 Absorption features

Absorption lines in the red, at 1.880 and 1.884 eV, are observed in the PL spectrum. The absorption lines are similar to those reported by Anderson [1]; however the transmission spectra in [1] show a different sideband structure, and the absorption features reported in that case reveal a much higher absorbance than is evident in the luminescence and transmission spectra presented in this work, i.e. transmission measurements on Rubicon samples, measured at the same temperature as Fig. 3 in [1], show an absorption of ~ 45 % at the higher energy feature relative to the background light intensity, while Anderson's sample appears to be nearly opaque at this energy. This could be due to some normalisation process in the spectra presented in [1], as the intensity axes of spectra in this work have arbitrary units. Figure 5.2 compares the transmission spectra observed in this work with Fig.3 in [1]. The data from [1] was obtained using a data digitizer (Windig 2.5, [2]). Also, as Anderson found that the intensity of the absorption features depended on the concentration of Ni in the samples, a relatively low concentration of Ni (~10^{-4} %, [3]) in the Rubicon samples in comparison to 0.76 % in Anderson's samples might explain the differences in absorbance.

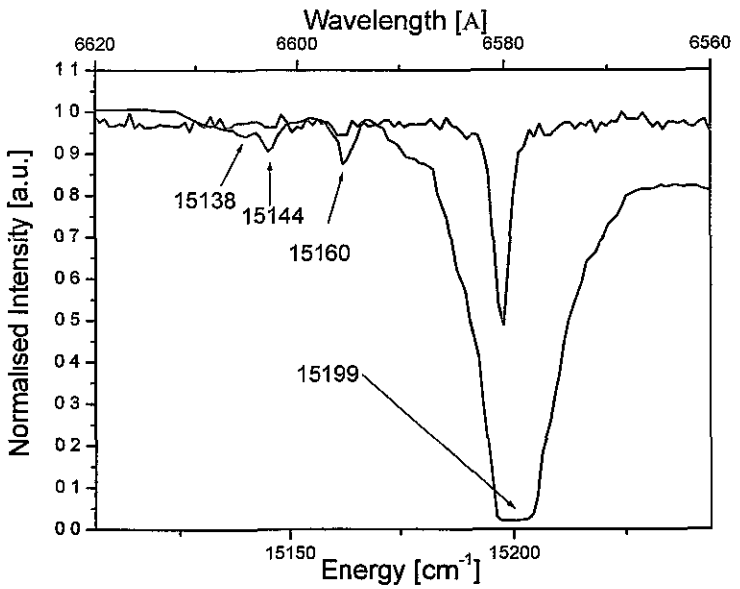

Figure 5.2: Comparison between absorption features observed by Anderson [1] (in black) and those presented in this work (in red). The spectrum in [1] has arbitrary units on the intensity scale, while the spectrum from this work has been normalised by the background light intensity

Transmission measurements were performed using a tungsten light source and show a strong polarisation effect connected with these absorption features; only the higher energy line is seen at normal incidence transmission, with the second line appearing as the sample is rotated from normal incidence. This polarisation behaviour could suggest that the absorption features originate from a defect in two different environments, with one aligned along the c-axis of the crystal and the other perpendicular to this axis, or that strong selection rules are at play.

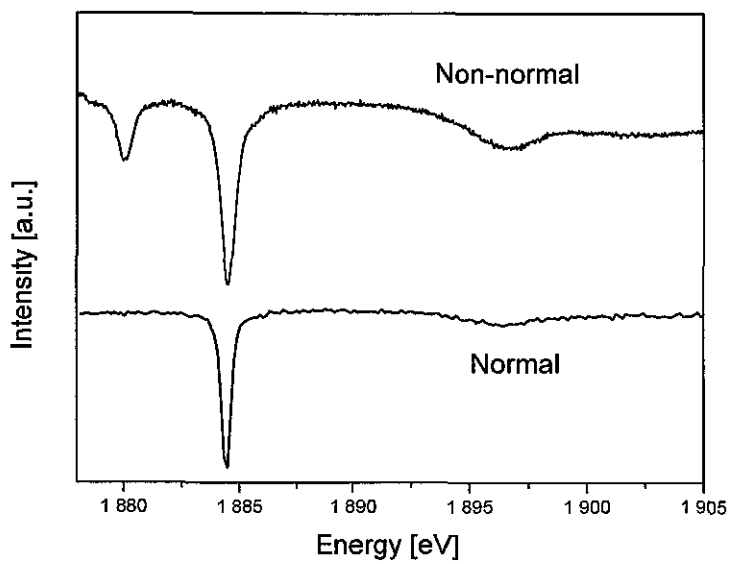

Figure 5 3: Transmission measurements on the absorption features. At normal incidence only the higher energy line is seen. As the sample is rotated, the other feature increases in intensity

Figure 5.4 shows the spectra obtained as the sample is rotated from normal incidence; the quoted angles are approximations, with an estimated error of about 10% and are included to indicate a greater/lesser angle between the excitation source and the sample. The spectra do show, however, that the relative ratio between the high energy absorption feature and the lower energy feature reduces in intensity as the sample is rotated from the typical absorption measurement experimental layout.

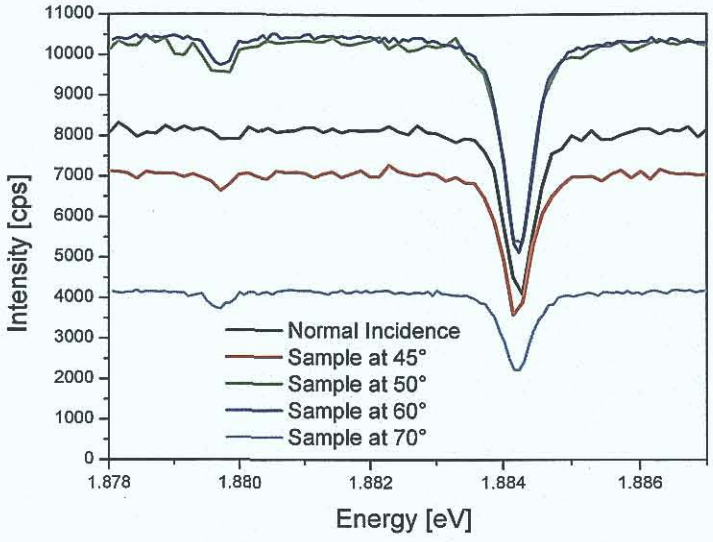

Figure 5.4: Spectra obtained as the sample is rotated from normal incidence. There is considerable error in the measurement of the angle

The absorption features at 1.880 and 1.884 eV broaden and decrease in intensity as the temperature increases, suggesting that they are zero phonon lines (ZPL). The features seen at higher energy appear to be phonon replicas of the higher energy ZPL. The temperature dependence of these signals is shown in Fig. 5.5; the data have been off-set for clarity. The behaviour of these features as a function of temperature will be discussed in the next section.

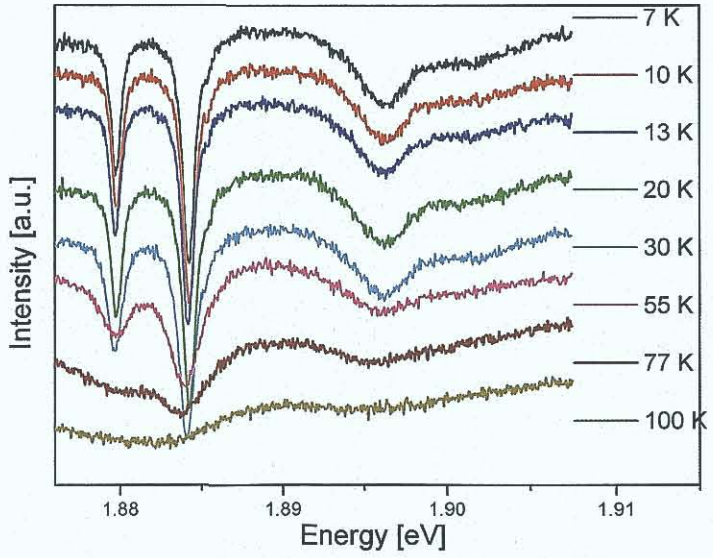

Figure 5.5: Temperature dependence of absorption features

5.2.1 Temperature dependence of Absorption lines

The strength of the absorption features were calculated by fitting a baseline, to nullify the effects of the broad band, inverting the resultant spectra, and fitting the zero phonon lines (ZPLs) to a Lorentzian curve. Figure 5.6 shows the appearance of the spectrum obtained when this is done. The details of the sidebands will be discussed later.

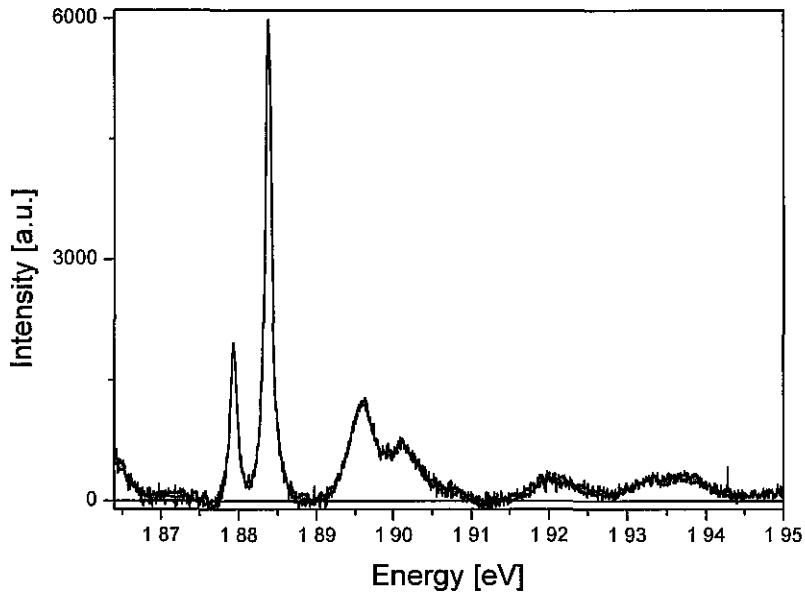

Figure 5.6: Spectrum obtained after fitting a baseline, to remove the broad band, and inverting the resultant intensity values

Figure 5.7 shows the variation in intensity of these signals as a function of temperature. After an initial increase in intensity between 2 and 15 K, the intensity of both features decreases as the temperature is raised.

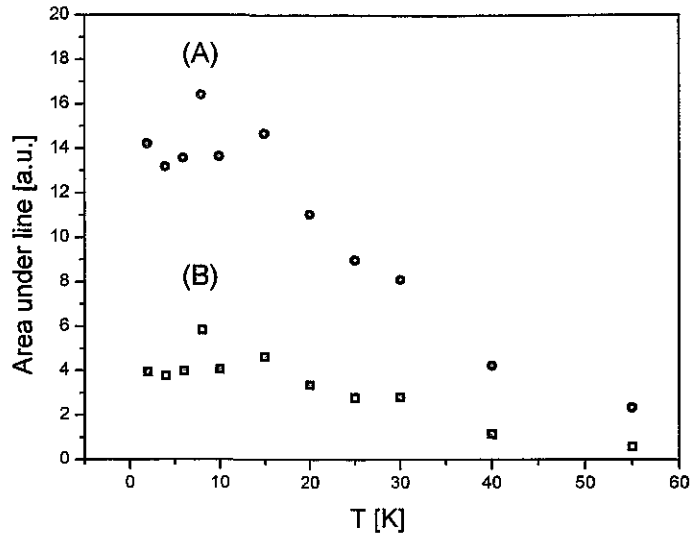

Figure 5 7: Intensity of absorption features as a function of temperature, (A) feature at 1.884 eV and (B) feature at 1.880 eV The maximum intensity for both absorption lines was observed at a measurement temperature of 8 K.

Using only the data where the intensity of the absorption lines is decreasing, the deactivation energy for these signals was determined using the model described in Chapter 2, which is based on the change with temperature being driven by the capture and emission of excitons only.

$$\ln\left(\frac{I_{\max}}{I(T)}-1\right)=\ln C_2-\frac{E_2}{k_B T} \qquad \textbf{5.1}$$

The result of this fitting process is shown in Figs. 5.8 and 5.9. With this model, a deactivation energy of 6.6 ± 0.5 meV was found for the higher energy ZPL, while a value of 5.9 ± 0.9 meV was found for the lower energy ZPL. Within experimental error, these values are the same.

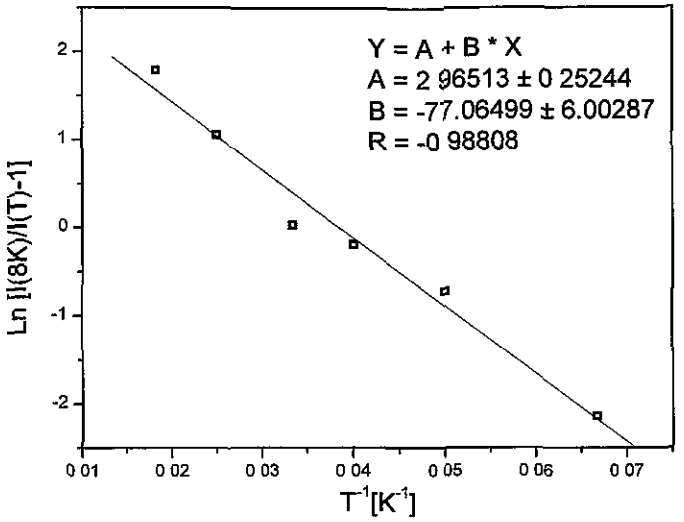

Figure 5.8: *Fit to the equation 5.1 for the relative change in intensity of the higher energy absorption ZPL as a function of inverse temperature.*

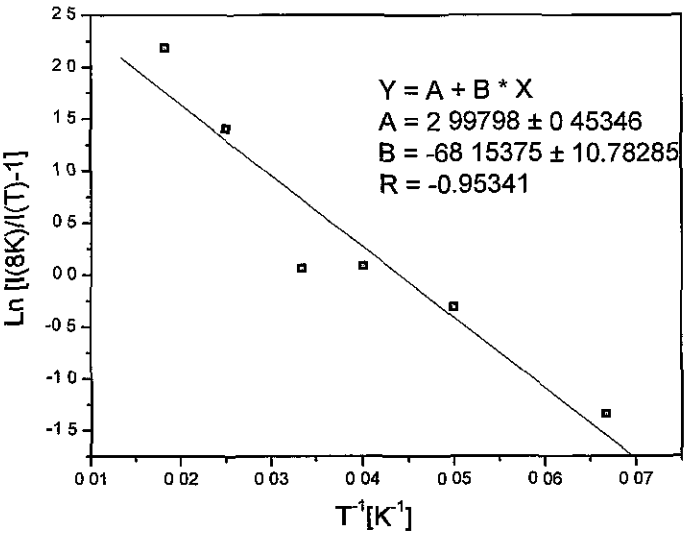

Figure 5.9: *Fit to the equation 5.1 for the relative change in intensity of the lower energy absorption ZPL as a function of inverse temperature*

Figure 5.10 shows the full width at half maximum height (FWHM) of both ZPLS, as determined from the Lorentzian fits, as a function of temperature. The error bars, most easily apparent at high temperature for the low energy ZPL, are due to the range of possible values for the linewidths obtained from the Lorentzian fits. These

features are quite broad in comparison to the linewidths observed for the L_1 emission features; at 2 K the linewidths are 0.6 and 0.7 meV for the absorption features at 1.880 and 1.884 eV, respectively, in comparison to 0.3 meV for the L_1 features at the same temperature.

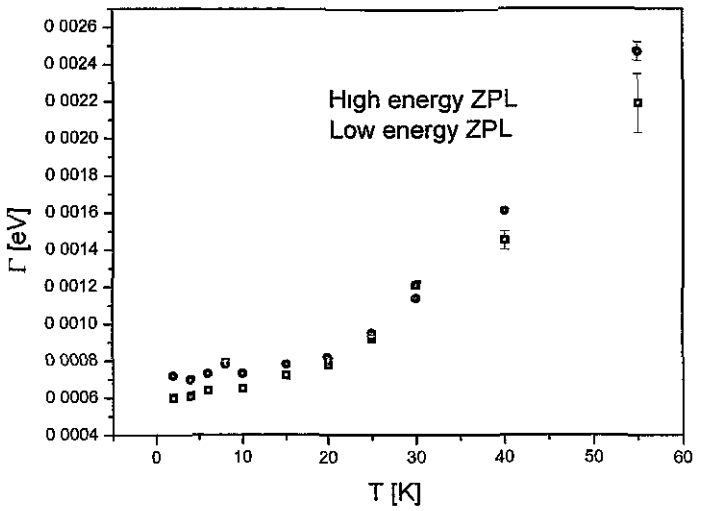

Figure 5.10: FWHM of absorption lines as a function of temperature

The data from Fig. 5.10 were used to fit the line broadening to equation 5.2.

$$\Gamma(T) = \frac{\bar{\alpha} \mid s_k \mid^2 \exp(\hbar\omega / kT)}{[\exp(\hbar\omega / kT) - 1]^2} \qquad \textbf{5.2}$$

with $\hbar\omega$ equal to the energy of the phonon interacting with the system, $|s_k|^2$ is the phonon coupling parameter and $\bar{\alpha}$ is a constant proportional to the strength of the phonon-impurity interaction.

Figure 5.11 shows the fit obtained for the absorption line at 1.880 eV, while Fig. 5.12 shows the results of the analysis for the feature at 1.884 eV. A value of 4.3 ± 0.7 meV was found for the lower energy feature. A phonon energy of 7.0 ± 0.3 meV was found for the higher energy absorption line. The phonon replica at 1.896 eV is the most intense phonon replica related to the ZPL at 1.884 eV, thus a separation of 12 meV is seen rather than the fitted value of 7 meV.

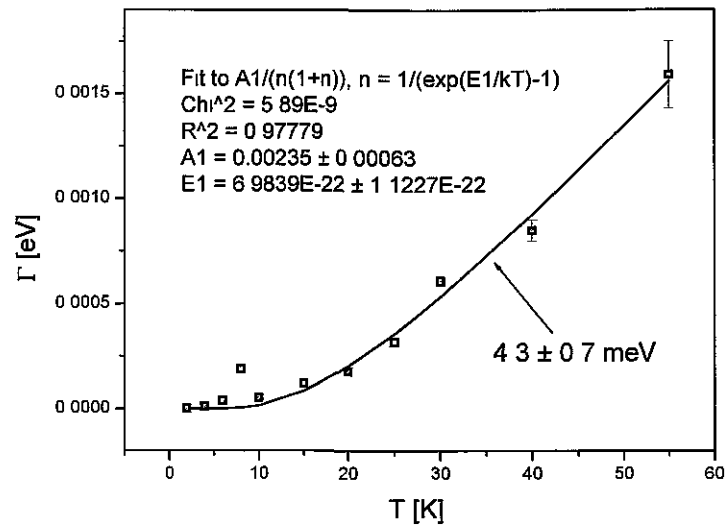

Figure 5.11: Plot of FWHM as a function of temperature for the feature at 1.880 eV. A value of 4.3 ± 0.7 meV was found to fit the data using equation 5.2

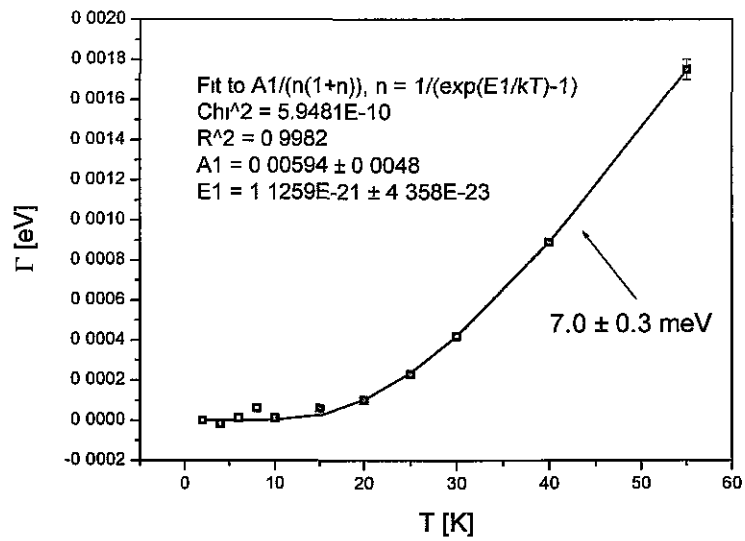

Figure 5.12: Plot of FWHM as a function of temperature for the feature at 1.884 eV. A value of 7.0 ± 0.3 meV was found to fit the data using equation 5.2

The fit of 4.3 meV for the relevant phonon energy from the line broadening of the lower energy doublet suggests that the high energy ZPL at 1.884 eV could consist of a ZPL and an overlapping phonon replica. There is some evidence for this in the PL spectrum shown below in Figure 5.13. The slope of the high energy side of the feature appears to be greater than the low energy side, and there appears to be a shoulder on the high energy side at 1.885 eV. The line P1 indicates this region. The line labelled P2 indicates the position of the phonon replica of the 1.884 eV absorption line at 1.896 eV.

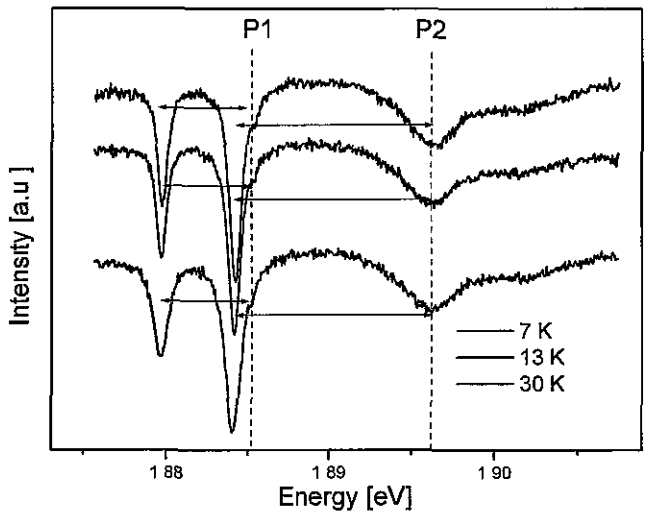

Figure 5.13: Spectra indicating positions of phonon replicas. The assignment of P1 as a phonon replica overlapping with the absorption line at 1.884 eV is tentative; however, it is close in energy to the phonon energies obtained from the temperature dependence

The reasonable agreement between the observed phonon energies and those obtained from the temperature dependence of the line broadening mechanism is consistent with the absorption lines being due to transitions on transition metal impurities in the material.

5.3 Infra-red emission

Figure 5.14 shows the spectra obtained at 20 K, using the PL system at CERN, over a large energy range. Overlapping spectra were normalised in order to construct a

full spectrum and then off-set for clarity. This is shown in Fig. 5.15 for spectra obtained at temperatures ranging from 2 to 55 K.

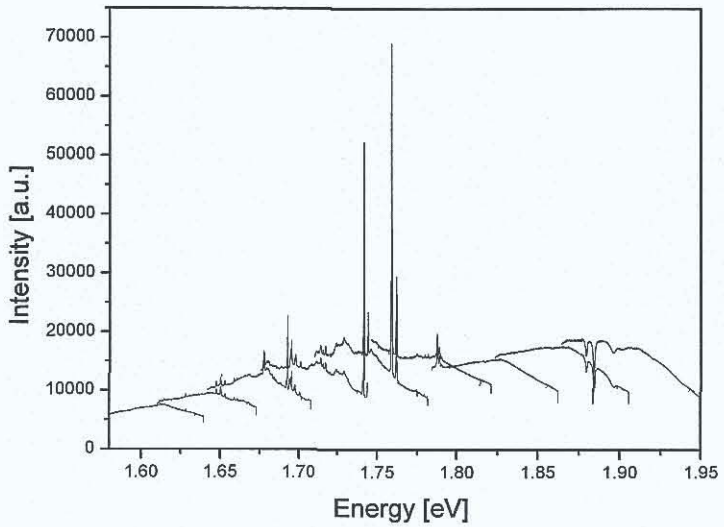

Figure 5.14: PL spectra at 20 K as-obtained, apart from wavelength calibration

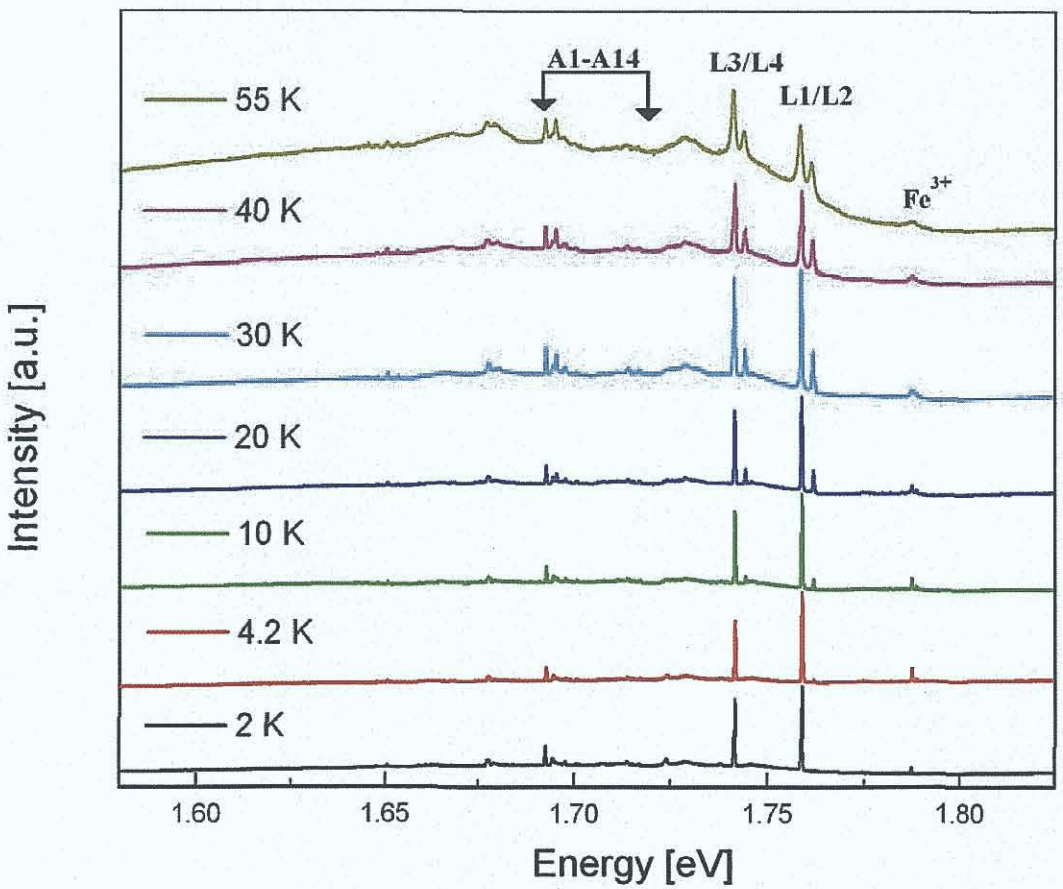

Figure 5.15: Spectra obtained at various measurement temperatures, with an offset included in order to see the detail in the spectra

The low energy IR emission consists of a superposition of emission lines that appear to be related to different defects. Heitz *et al.* [4] observed a line at 1.78742 eV at 1.6 K, with five higher energy lines appearing as the temperature was increased, and attributed these features to the $^4T_1(G)$-$^6A_1(S)$ transition of an isolated Fe^{3+} ion. Good agreement was also found between the zero-field splitting observed in Zeeman measurements and that calculated from ESR measurements for Fe^{3+}. Intense phonon replicas were also reported with this emission. Along with the Fe^{3+}-related emission, there is also a series of sharp lines and corresponding phonon replicas that have not been reported in the literature. The dominant features related to this series of PL signals are labelled L1 and L3 in Fig. 5.15. One of the difficulties in analysing these spectra is that it is difficult to separate out features related to the Fe^{3+} emission and the other overlapping signals. This is particularly a problem with the identification of the phonon replicas. Figure 5.16 shows the PL spectra, measured at 10 K, obtained under excitation from (A) 415 nm light from a Xenon lamp and monochromator, and (B) 532 nm light from a frequency doubled Nd:YAG laser. Spectrum (A) appears to be the same as the spectra of the Fe^{3+} emission reported in [4, 5], while spectrum (B) consists of a superposition of the Fe^{3+} emission and the emission from the unknown defect.

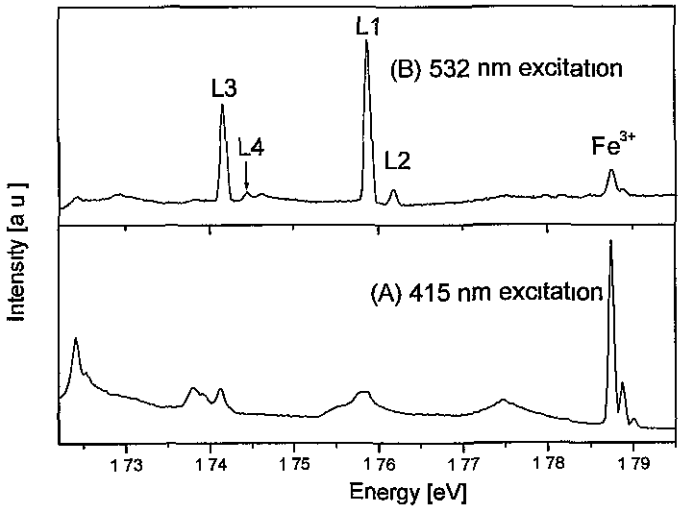

Figure 5.16: PL spectra at 10 K obtained under excitation with light at 415 nm (A) and 532 nm (B)

In order to check whether the luminescence features in Spectrum (A) in Fig. 5.16 are the same features as seen in [4, 5], a spectrum was scanned using a data digitizer

(Windig 2.5) from [5], and compared to a spectrum in this work. The spectrum from [5] was measured at 14 K with the luminescence excited by light of photon energy 3.18 eV. The spectrum measured in this work was measured at 20 K and excited with light of photon energy 3.02 eV. This spectrum was chosen as the resolution (approximately 2 meV) appears to be similar to that in [5]. As can be seen in Fig. 5.17, the two spectra are very similar, showing that luminescence from an Fe^{3+} defect is observed in these samples.

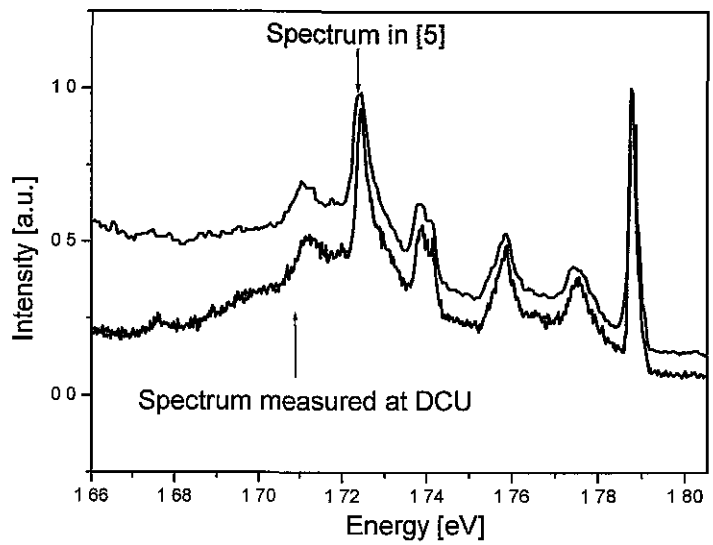

Figure 5.17: The upper spectrum in blue, scanned from [5], was measured at 14 K under excitation with light of photon energy 3.18 eV, while the spectrum in black (this work) was measured at 20 K under excitation with light of photon energy 3.02 eV

The samples were annealed in a variety of atmospheres at different temperatures in order to see whether the unknown emission could be increased. It was found that annealing reduced the intensity of this emission in nearly all cases. However, annealing in vacuum increased the intensity of the Fe^{3+} emission relative to the other sharp line signals. In Fig. 5.18, spectrum (1) shows the photoluminescence spectrum obtained after annealing in vacuum, while (2) shows the PL spectrum of an as-received wafer. A baseline has been subtracted and the data have been normalised to the Fe^{3+} ZPL. The intensity ratio between the Fe^{3+}-related signals and the other features present in spectrum (1) are greater than the corresponding ratio in spectrum (2). The difference between the behaviour of the features with annealing, suggests that two different defects are responsible for the emission seen in this energy region. The emission lines not related to the reported Fe^{3+} emission are shaded in grey.

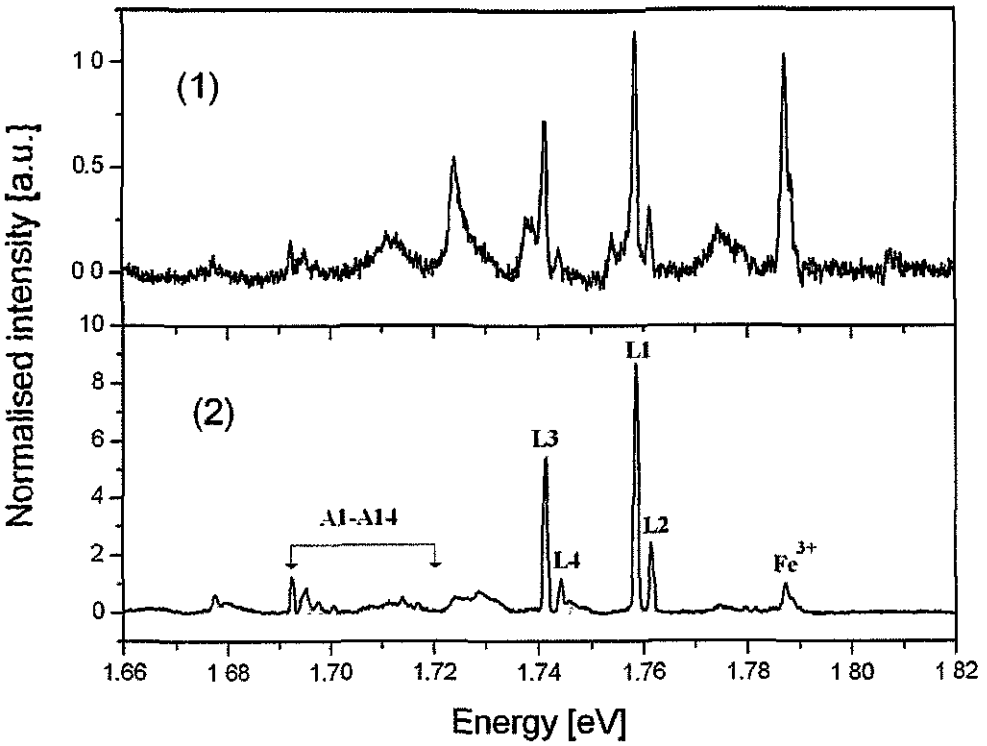

Figure 5.18: Spectrum (a) shows the PL spectrum obtained after annealing in vacuum, while spectrum (2) is from an untreated sample. The emission lines not related to the Fe^{3+} emission are shaded in grey

There are also a series of weak closely spaced lines at the low energy side of the Fe^{3+} ZPL, that were not reported in [4, 5] but are possibly related to the recombination at an Fe^{3+} defect. This region is shown in detail in Fig. 5.19 with the unreported features indicated with black arrows. Blue arrows indicate features reported in the literature as being related to an Fe^{3+} defect.

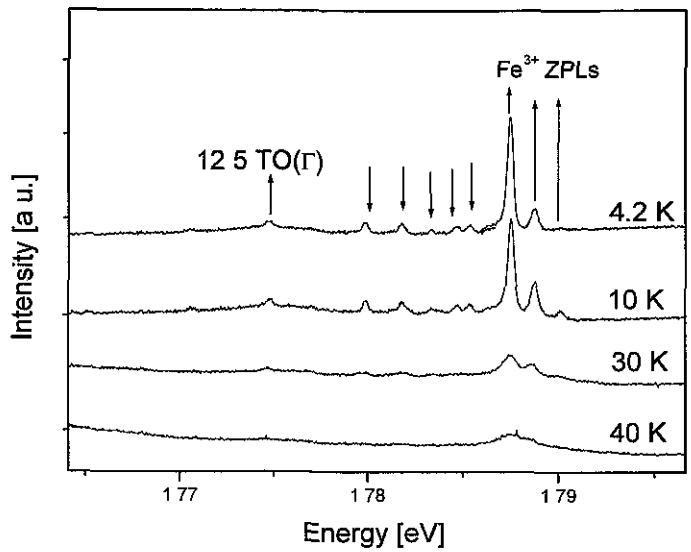

Figure 5.19: *Fe^{3+} ZPL region at 4.2, 10, 30 and 55 K. The low energy lines marked with arrows do not appear to have been reported in the literature. The other low energy feature marked with a blue arrow appears to be the 12.5 TO(T) phonon replica, reported by Heitz et al. [4]*

The principal lines in the, as yet, unidentified emission, labelled L1 and L3, are at 1.7587 and 1.7415 eV, respectively. Weak lines, ~3 meV higher in energy than these features, labelled L2 and L4, appear as the temperature is increased. The energies of some of the unreported features and their identifications are listed in Table 5.1. The phonon energy ranges listed in the table are as reported in [6]. Identifications were made by comparing the data obtained under different excitation conditions, by examining the data as a function of temperature, by an anneal study and by comparison with the literature spectra of the Fe^{3+} lines. By a process of elimination, the "unknown emission" was separated from the Fe^{3+} signals.

Energy [eV]	Label	ΔE [meV]	Identification	Heitz (Fe^{3+})	Heitz (V^{3+})
1.7587	L1	ZPL	ZPL		
1.7617	L2		ZPL		
1.7460	P1	12.7	TO(Γ)[E_2]	12.74	12.6
1.7415	L3	17.2	ZPL		
1.7442	L4	14.5			
1.7291	P2	12.7	TO(Γ)[E_2]		
1.7430	L1 Phonon	15.7			
1.7398	Phonon	18.9			
1.7360	Phonon	22.7	22.3 LA(A), LO(A)	22.26	22.0
1.7267	Phonon	32		32.28	31.9
1.7254	Phonon	33.3		33.71	33.6
1.7185	Phonon	40.2			
1.7171	A12				
1.7155	A11				
1.7143	A10				
1.7139	A9				
1.7117	Phonon	47.0	46.9 TO(Γ)	46.15	47.2
1.7079	Phonon	50.8	50.8 TO(Γ)	49.5	49.4
1.7061	Phonon	52.6			
1.7035	Phonon	55.2	54.6 TO(Γ)	56.76	58.1
1.7008	A7				
1.6979	A6				
1.6959	Phonon/A4	62.8		63.25	62.7
1.6954	A3				
1.6946	A2				
1.6927	A1				
1.6887	Phonon	70	71.4 LO(Γ)	74.55	74.5

Table5.1: Table listing some of the features observed in the IR emission.

The temperature dependence of the L_1 lines is discussed first, followed by a discussion of features in the region 1.67 to 1.72 eV which have been termed the A_1

lines. It is possible that these two sets of lines are related; the annealing study suggests this but it is not conclusive that this is the case.

5.3.1 Temperature dependence of L_i lines

The temperature dependence of the L_i features is shown in Fig. 5.20. As can be seen, the ratios L1:L2 and L3:L4 decrease with increasing temperature.

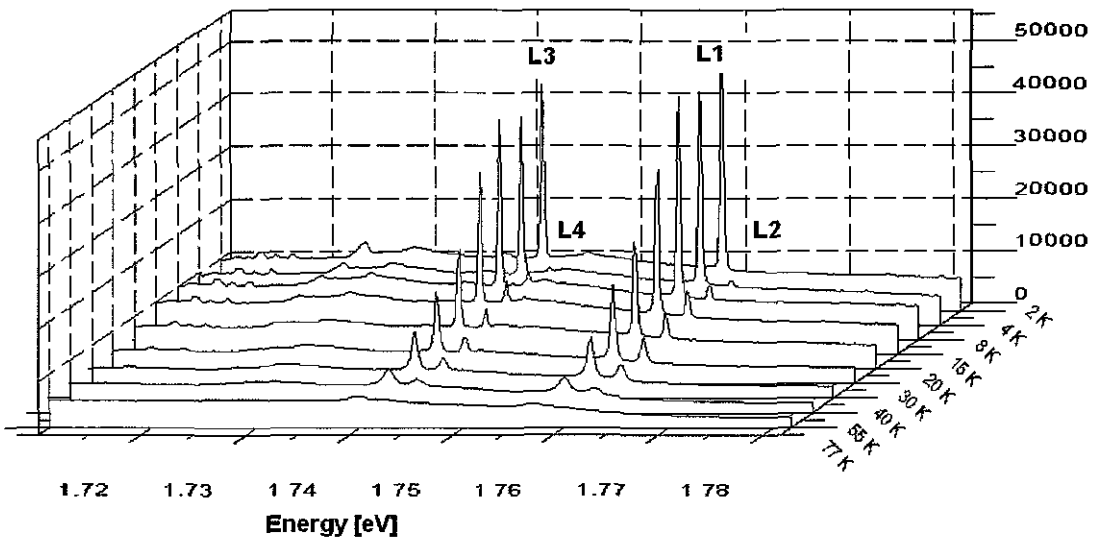

Figure 5.20: Temperature dependence of the IR emission from 2 to 77 K

This behaviour is typical of transitions from a split excited state to a common ground level, as depicted in Fig. 5.21.

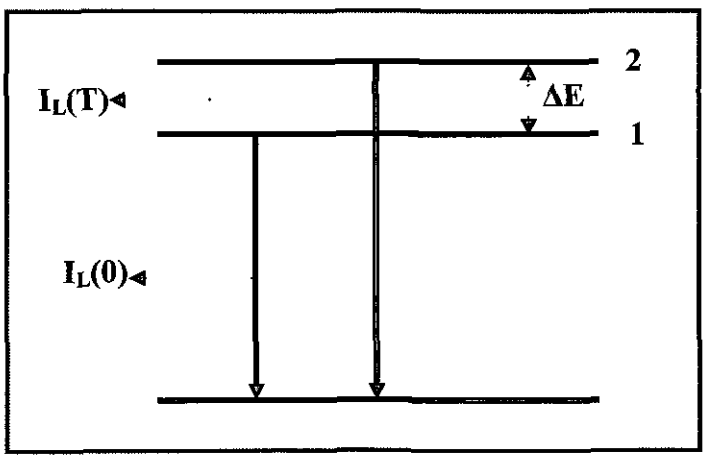

Figure 5.21: Diagram of a two-level system, separated by an energy ΔE

An attempt was made to fit these data using the model described in Chapter 2 which discusses transitions between two different excited states to a common ground level.

$$\ln\left(\frac{I_2}{I_1}\right) = -\frac{\Delta E}{k_B T} + \ln g_{21} + \ln f_2 - \ln f_1 \qquad \textbf{5.3}$$

Here, ΔE represents the energy separation between the two excited state 1 and 2 in Fig. 5.21, g_{21} is the ratio of the degeneracy between the upper and lower states, and f_i are the transition probabilities. As the separation between each component of the two doublets L1/L2 and L3/L4 is small, it is important to know the sample temperature accurately. Due to the dependence of the energy splitting on inverse temperature, even small errors at low temperature will lead to significant errors in the results obtained. Perfect accuracy in the temperature measurement is difficult to achieve in practice as the temperature sensor is not in thermal contact with the sample. Laser heating of the sample can result in a significant difference in temperature between the sample and the sensor reading. This can be accounted for if there is some other signal in the PL spectrum that has a known thermal behaviour. Alternatively, as described by Davies [7], spectra can be taken as the excitation power is varied. The intensity of a particular feature can then be plotted as a function of laser power, and assuming that the relationship between laser heating and the output power of the excitation source is linear, the intercept will provide the intensity of the emission signal with no laser heating. Fig. 5.22 shows the change in the intensity ratio L2:L1 as the laser excitation power is varied between 200 and 500 mW at a temperature set point of 10 K, with the data normalised to the height of L1. The increase in this ratio, along with line broadening and red-shifts of the features suggests that there is some laser heating.

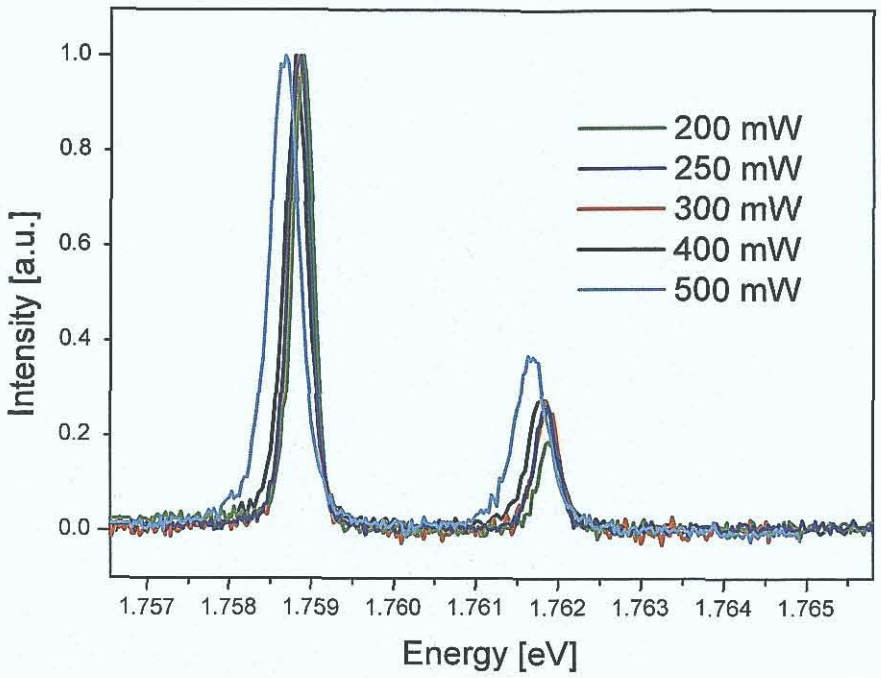

Figure 5.22: Effects of changing the laser excitation power on the PL spectrum. Line broadening and a shift to lower energy is observed as well as a change in the relative intensities of L1 and L2 suggesting that there is some laser heating of the samples

Following Davies [7], the ratios L2:L1 and L4:L3 were examined at various laser powers at different temperatures. This is shown below in Fig. 5.23 for the ratio L2:L1 with the temperature sensor reading 10 K; Fig. 5.24 shows the corresponding plot for the intensity ratio of the lower energy doublet, L4:L3. Spectra measured at other temperatures are shown in Appendix A. The slopes of the linear fits applied to each data-set are different and tend to become smaller as the temperature is increased, suggesting that the laser heating effect is itself a function of temperature.

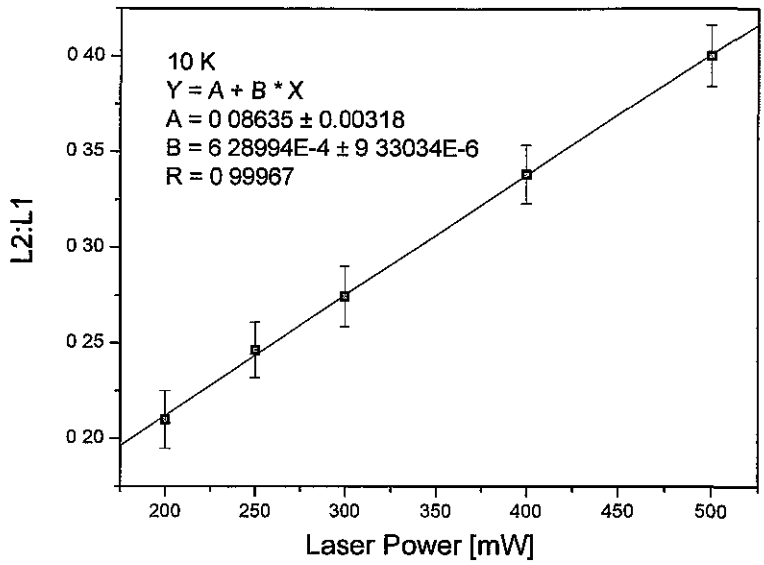

Figure 5.23: Ratio between L2 and L1 as a function of excitation power. As can be seen, the intensity of L2 relative to L1 increases as a function of laser power. The intercept gives the ratio between the two emission lines at a sample temperature of 10 K

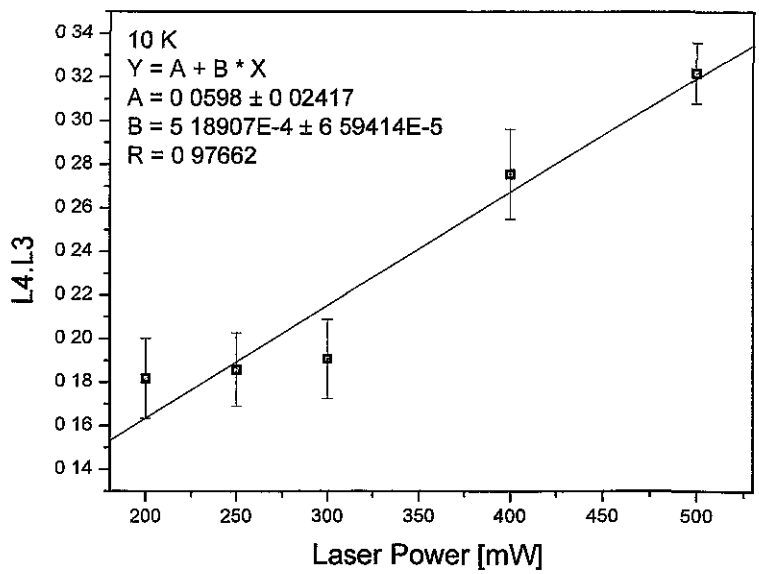

Figure 5.24: Ratio between L4 and L3 as a function of excitation power. Again, the ratio L4:L3 increases as a function of laser power. The intercept gives the ratio between the two emission lines at a sample temperature of 10 K

As discussed previously, the natural log of each intercept plotted as a function of inverse temperature is expected to yield linear plots with slopes equal to the energy

separation between the excited states of the two transitions, ΔE in Fig. 5.21. These are shown in Figs. 5.25 and 5.26 for L2/L1 and L4/L3, respectively. For L2/L1, the activation energy for L2 relative to L1 was found to be 2.1 ± 0.2 meV in comparison to a spectral separation of 3 meV. The intercept of -0.2 ± 0.1 gives a value of 0.8 ± 0.1 for $g_{21}f_2/f_1$. For L4/L3, the slope corresponded to an energy separation of 2.0 ± 0.2 meV in comparison to the observed separation of 2.7 meV. The intercept, in this case, results in a value of 0.6 ± 0.1.

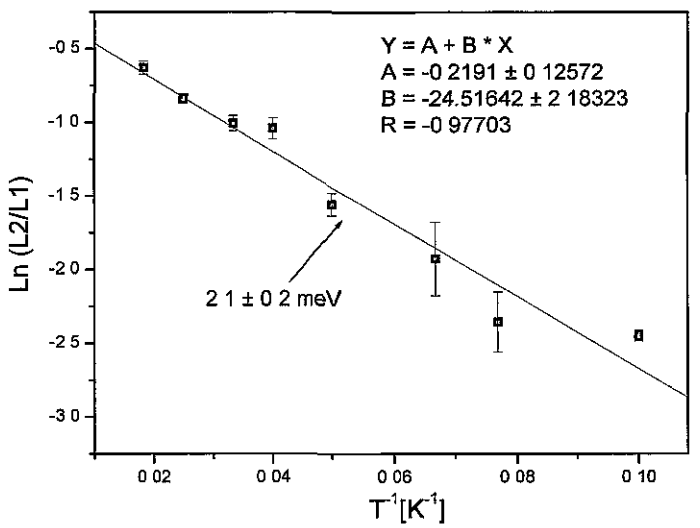

Figure 5.25: Arrhenius plot of the natural log of the ratio between the features L2 and L1 plotted versus inverse temperature.

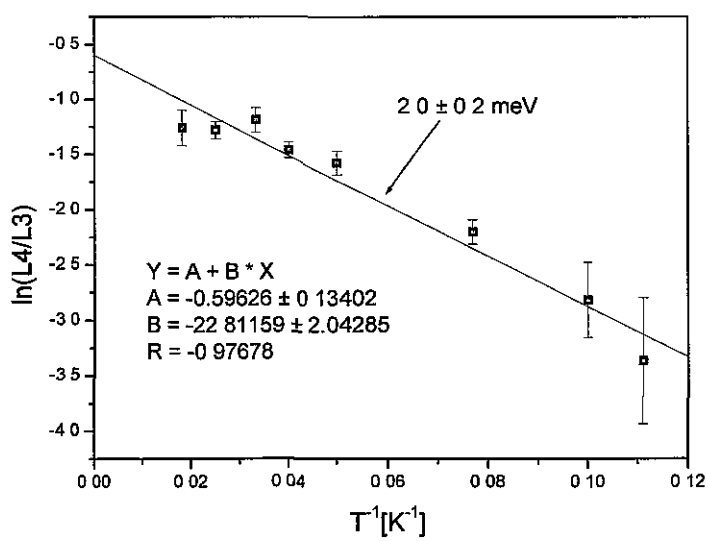

Figure 5.26: Arrhenius plot of the natural log of the ratio between the features L4 and L3 plotted versus inverse temperature.

If these systems were to behave in the same manner as the "split-excited state" model described in Chapter 2, one would expect the energy separation obtained in the Arrhenius plot to match energy separation observed in the PL spectrum. Clearly, this is not the case, so we must consider an alternative energy level diagram for the luminescent centres. The luminescence could have a more complex origin, i.e. the ground state could also be split. Fig. 5.27 shows a schematic diagram of transitions occurring between different excited and ground states.

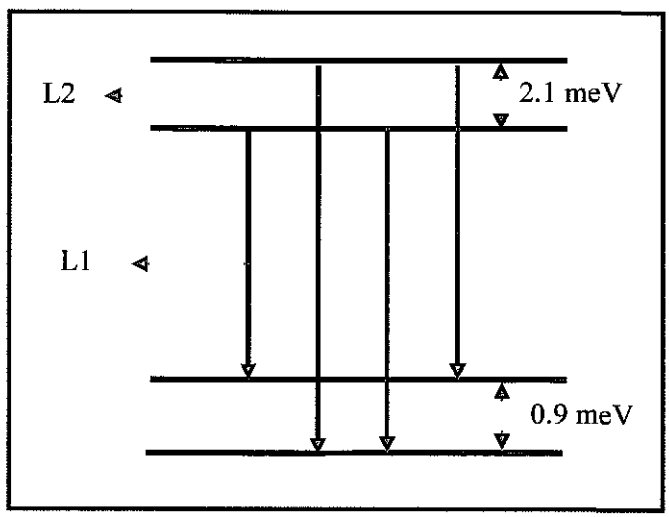

Figure 5.27: Schematic diagram of an alternative energy diagram of the transitions L1 and L2

If this model is correct, there are two forbidden transitions corresponding to the green arrows in Fig. 5.27. If weakly allowed, these features would be seen at approximately 1.7596 and 1.7608 eV in PL spectra. As can be seen in Fig. 5.28, emission lines are not seen at these positions.

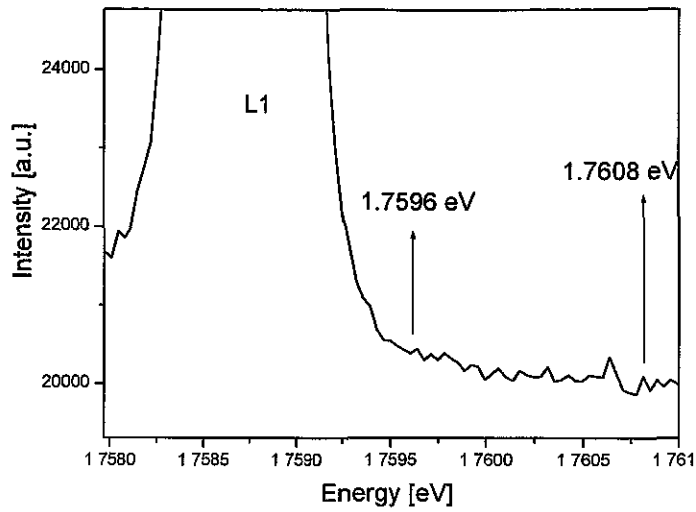

Figure 5 28. Spectrum showing region, marked by an arrow, where a third peak is expected to appear

Similarly for the L3 and L4 system, one might also expect to see weak features corresponding to the green arrows in Fig. 5.29.

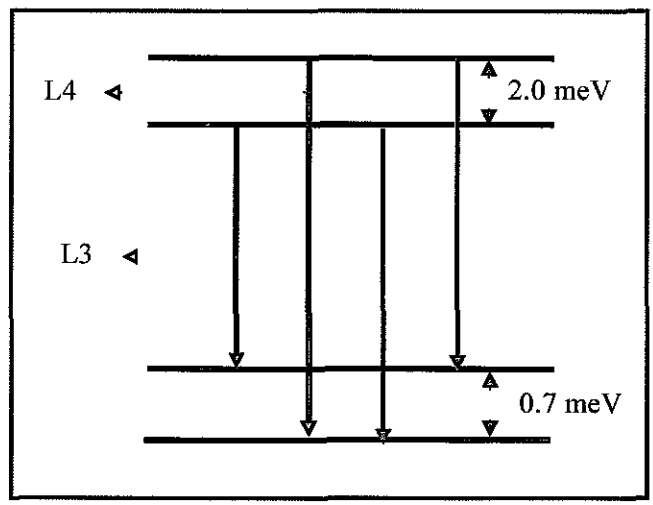

Figure 5.29: Schematic diagram of an alternative energy diagram of the transitions L3 and L4

Figure 5.30 shows the energy position corresponding to the transition marked by the green arrows in Fig. 5.30. Again, there is no obvious emission feature at this energy.

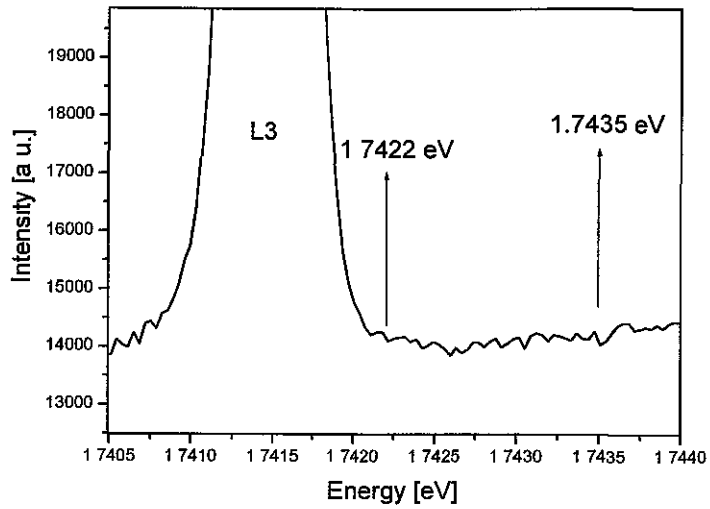

Figure 5.30: Energy position, marked by an arrow, where a third feature is expected to be observed

The absence of any evidence for the "forbidden" transitions means that we need to consider again the matter of the sample temperature. As there is not a large discrepancy between the fitted energy values and those seen in the PL spectra, it is interesting to see what is the difference between the experimental data and fitted data-sets constrained to have slopes equal to the observed energy separations, corresponding to an energy diagram as shown below in Fig. 5.32.

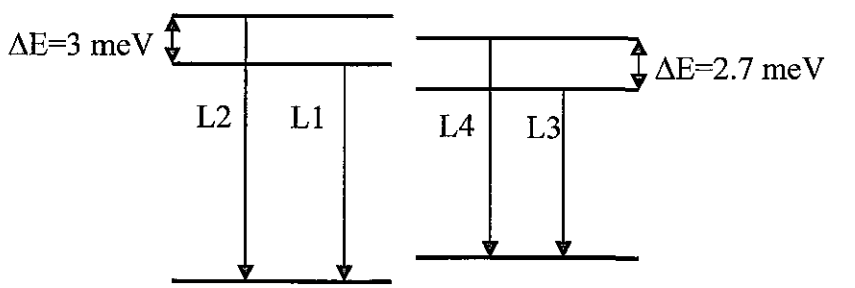

Figure 5.32: Schematic diagram of possible energy diagrams for L2/L1 and L4/L3 doublets

Figures 5.32 and 5.33 compares the data obtained with these constrained fits. The data for L2:L1 are reasonably in line with the fitted data points, except at low temperatures, but the correspondence for L4:L3 is not as good. This could be due overlapping of the TO(Γ)[E_2] phonon of the L1 emission line with L4, which creates

error in the fitting of L4. This can be seen in Appendix A; in general a plot of L2:L1 as a function of laser power is more linear than the corresponding plots for L4:L3.

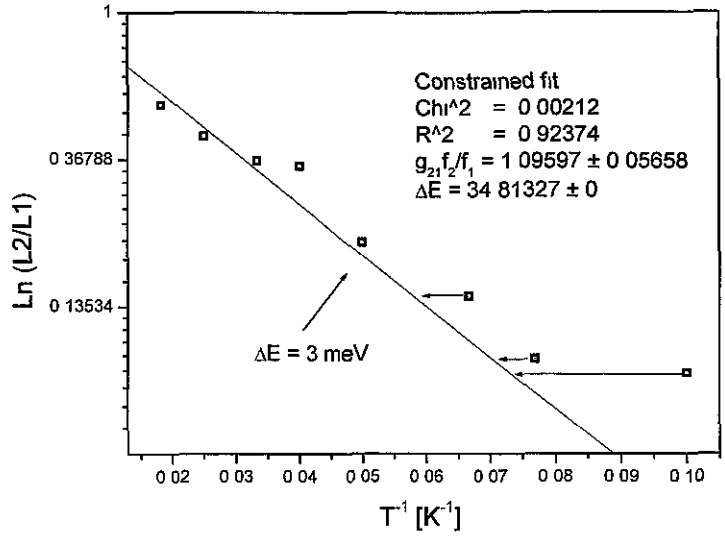

Figure 5.32: Constrained fit with the slope of the line selected to match the spectral separation of the L1 and L2 features. The red arrows indicate the difference in temperature between the nominal temperature and the constrained fit

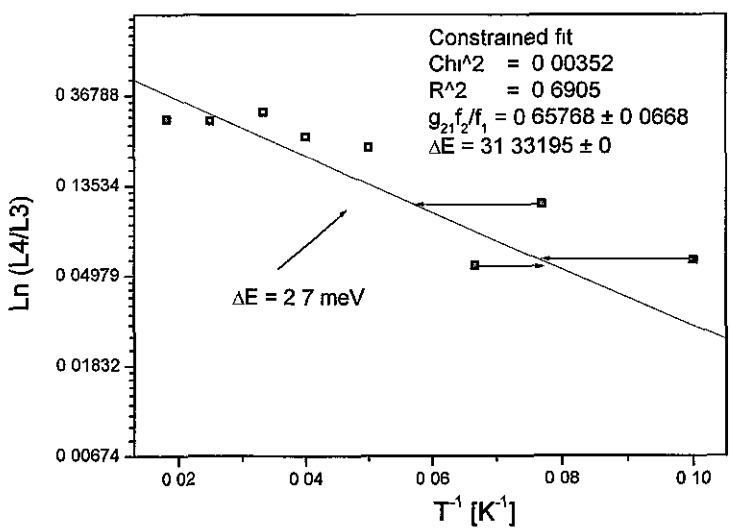

Figure 5.33: Constrained fit with the slope of the line selected to match the spectral separation of the L3 and L4 features

Table 5.2 shows the difference in temperature between the temperature controller reading and that obtained from the constrained fit.

L2/L1		L4/L3	
Data Temperature (K)	Correction from fit (K)	Data Temperature (K)	Correction from fit (K)
10	3.7	10	3.1
13	1.2	13	4.6
15	2.2	15	-2.3

Table 5.2: Table listing the difference between measured sample temperature and the fitted values for temperature, if ΔE is assumed to be equal to the energy separation observed in the PL spectrum

Due to the reasonable agreement of the L2:L1 data with the observed energy separation and the absence of additional structure in the spectra which would suggest a split ground state, it is perhaps more likely that Fig. 5.21 represents the level scheme of these transitions rather than those portrayed in Figs. 5.27 and 5.29. There is a need, therefore, to repeat this study at lower temperatures to provide confirmation. However, this should not impact too much on the temperature dependence data for the line-broadening, line position and deactivation energy, as these parameters only change significantly above 20 K where the laser heating effect is not as significant.

Deactivation energy for the L_i features

We now consider the temperature dependence of the combined L_1 lines. The following graph, Fig. 5.34 shows the sum of the integrated intensities for the higher energy doublet, L1 and L2, as a function of temperature. At 2 K, only the lower energy line, L1, is seen. After an initial slight increase in intensity from 2 to 8 K, there is a decrease in the sum of the intensity of the doublet.

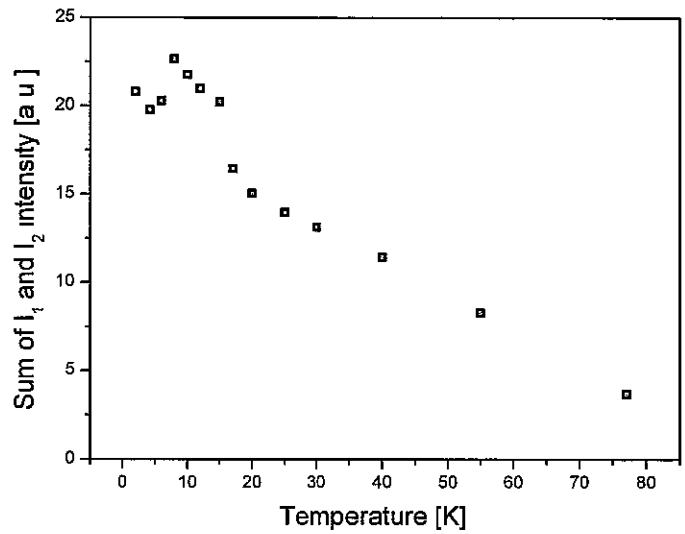

Figure 5.34: Intensity of the sum of L1 and L2 plotted versus temperature. As the intensity maximum is observed at 8 K, only data measured above this temperature is used to model the deactivation energy of this system

The data in Figs. 5.34 were used to model the deactivation energy of the defect. Only the data between 17 and 55 K were used as the integrated intensity of each doublet is decreasing over this temperature range data were normalised to the intensity of the L1/L3 line at 8 K. This normalised intensity was then plotted against inverse temperature and fit to equation 5.1. The result of this fitting process is shown in Fig. 5.35 and a deactivation energy, for the sum of L1 and L2, of 3.9 ± 0.3 meV was found.

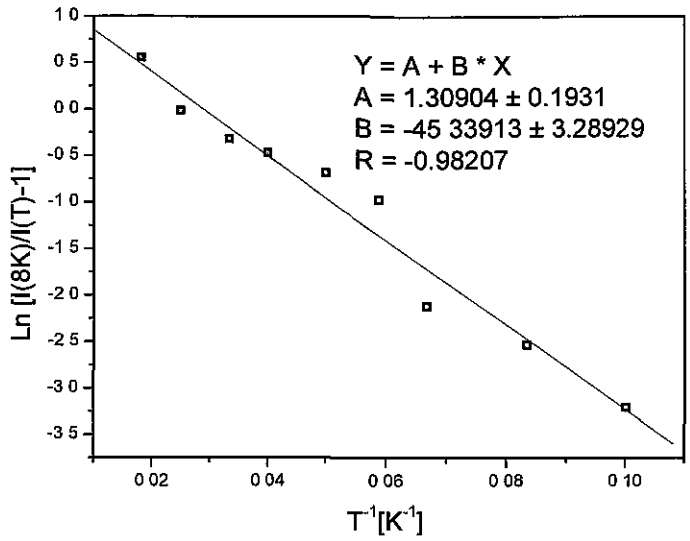

Figure 5.35 *Sum of L1 and L2 for each temperature normalised by the intensity of L1 at T = 8 K. The data were fit using equation 5.3*

The same analysis was performed for the lower energy doublet, and is shown in Figs. 5.36 and 5.37. In this case an activation energy of 3.7 ± 0.3 meV was found to fit the data. As there is quite a large uncertainty in the value of E, within the accuracy of the fit, the deactivation energies for the two doublets could be the same.

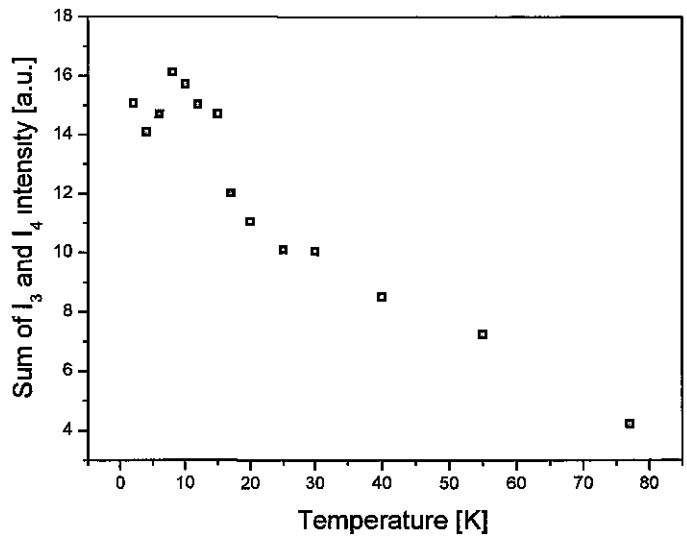

Figure 5.36. *Intensity of the sum of L3 and L4 plotted versus temperature*

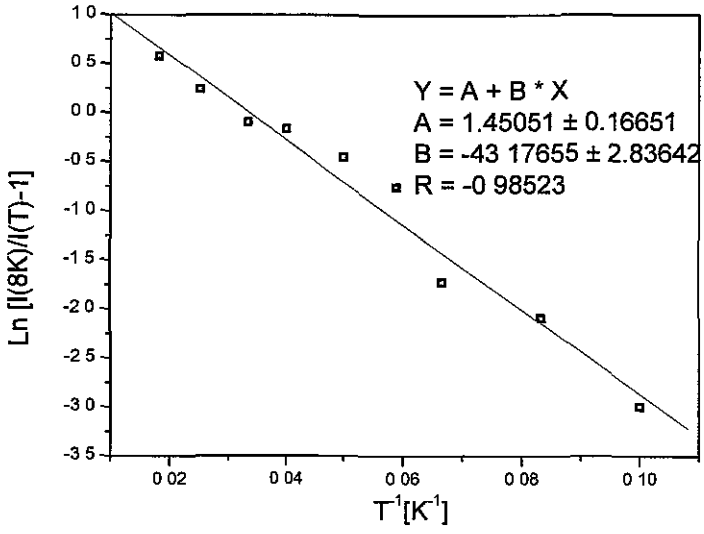

Figure 5.37: Sum of L3 and L4 for each temperature normalised by the intensity of L3 at T = 8 K. The data were fit using equation 5.3

Line shifts/widths of L_i features as a function of temperature

The shift in energy of the emission lines was plotted against sample measurement temperature. For this data, the line positions as measured with the FT system at DCU were used. For the L1 feature, a fit to the shift to lower energy of the peak yielded a phonon energy of 10.0 ± 0.2 meV. The equation used was

$$\Delta\omega = \frac{\alpha \mid s_k \mid^2}{\exp(\hbar\omega / kT) - 1} \qquad \textbf{5.4}$$

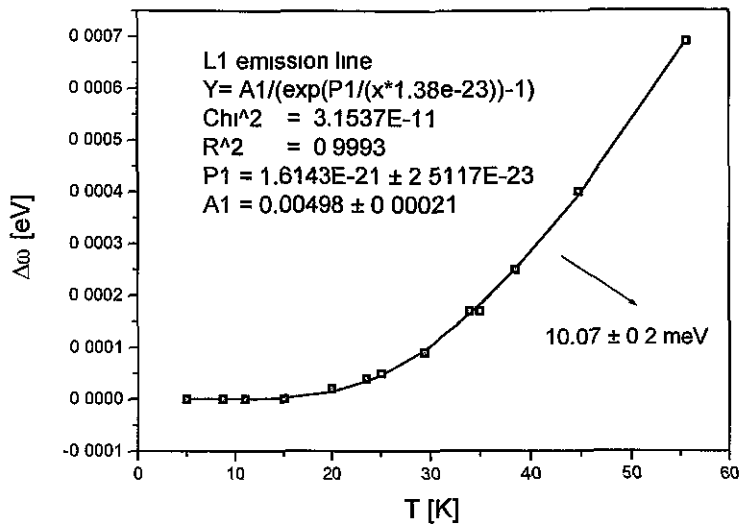

Figure 5.38: Plot of change in peak position of L1 as a function of temperature. phonon energy of 10.0 ± 0.2 meV was found to fit the data

The line broadening of the emission lines L1 and L2 were fit to equation 5.2 from page 77. In this case, a phonon energy of 10.9 ± 0.3 meV was fitted to the L1 data. This data is presented in Fig 5.39. In comparison, the most intense phonon replica of this peak lies at ~ 1.7460 eV, 12.7 meV lower in energy.

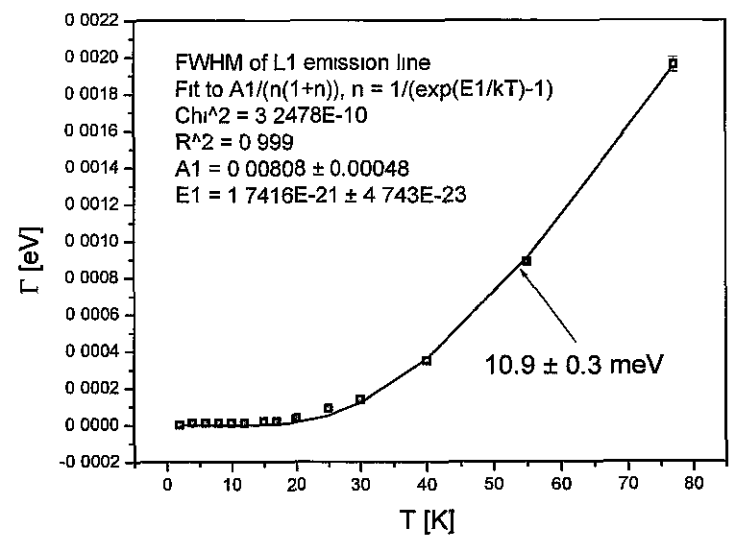

Figure 5.39: FWHM of L1 as a function of temperature; a fit to equation 5.2 resulted in a phonon energy of 10.9 ± 0.3 meV

For L3, a phonon energy of 11.0 ± 0.2 meV was obtained, when the shift in energy of the emission line with increasing sample temperature is examined, while a fit to an energy of 11.1 ± 0.4 meV was found for the broadening of the L3 ZPL.

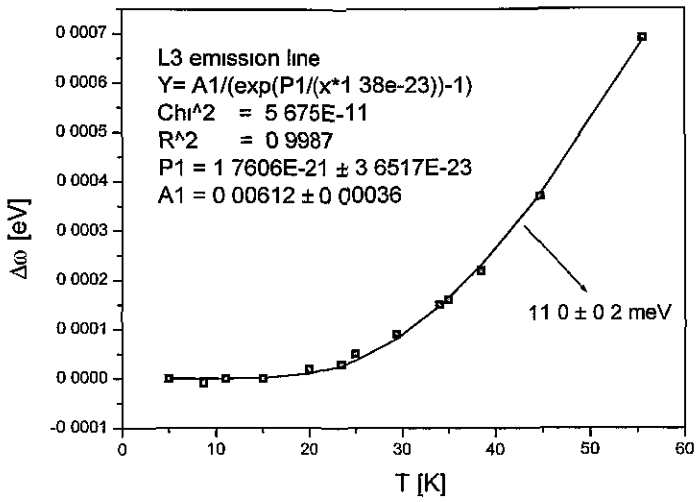

Figure 5.40: Plot of change in peak position of L3 as a function of temperature in comparison to the 2 K energy position. A phonon energy of 11.0 ± 0.2 meV was found to fit the data

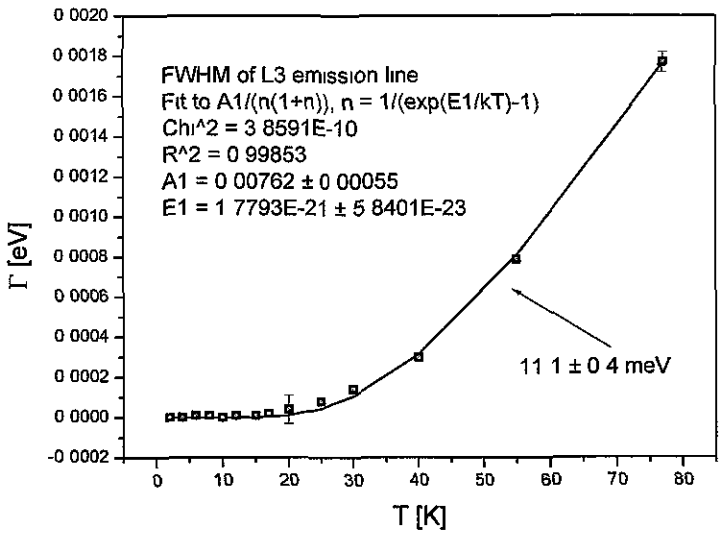

Figure 5.41: FWHM of L3 as a function of temperature; a fit to equation 5.2 resulted in a phonon energy of 11.1 ± 0.4 meV

5.3.2 Temperature dependence of A_i lines

We now consider another set of lines observed in the PL spectrum when excited by 532 nm light. Figure 5.15 is reproduced below in order to indicate the relative position of the A_i and L_i features.

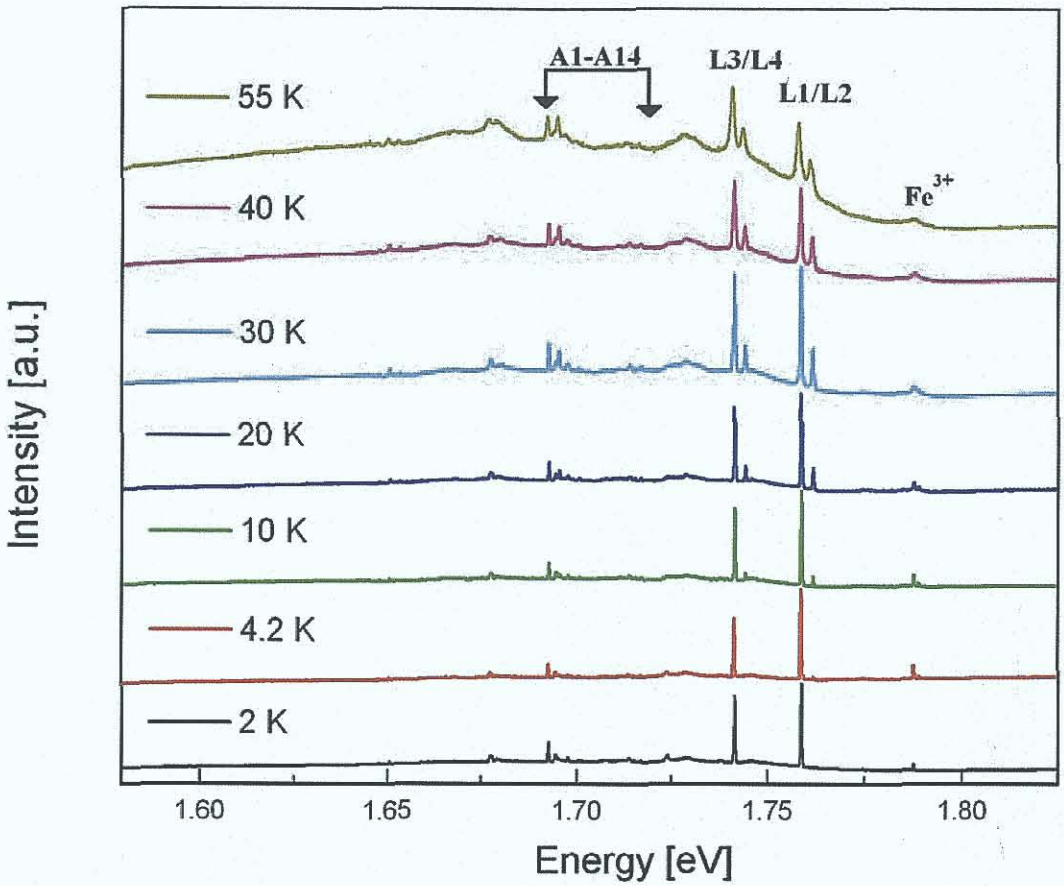

Figure 5.15: Spectra obtained at various measurement temperatures, with an offset included in order to see the detail in the spectra

At lower energy, at 1.6927 and 1.6954 eV, there are two lines that behave in a similar manner to the L1/L2 and L3/L4 doublets. This can be seen in Fig. 5.42; the two features are labelled A1 and A3. The higher energy emission line seen in the 2 K spectrum, A4, appears to have a different origin than the A3 feature and could be a phonon replica of L1 feature, Heitz having observed prominent phonon replicas with a similar energy in Fe and V doped ZnO [4]. Phonon replicas of the A_i emission features are observed 15 meV towards lower energy. The most intense phonon replica is marked with an arrow, and appears to be related to the A1 line. An extra phonon can be seen in the 20 K scan, P3, relating to the A3 line.

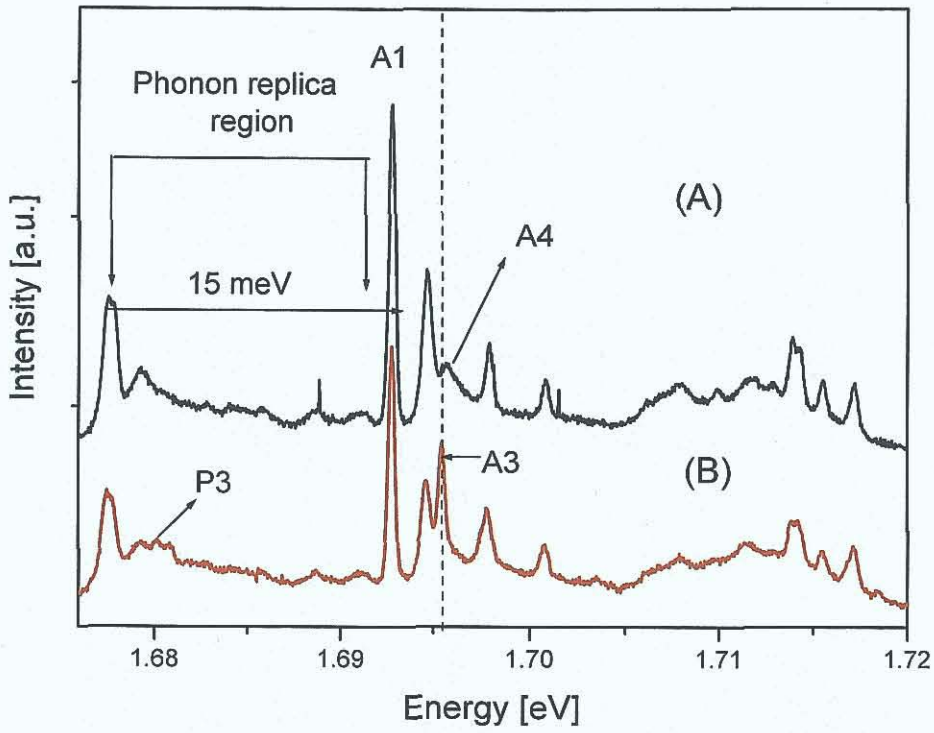

Figure 5.42 *(A) Spectrum measured at 2 K, (B) spectrum measured at 20 K. The region at lower energy, bordered by arrows, seems to contain phonon replicas of the sharper emission lines observed 15 meV higher in energy. The feature labelled A3 grows more intense with increasing temperature relative to the feature labelled A1*

In order to see the changes occurring in the spectra obtained as the sample temperature is increased from 2 K, the two spectra shown in Fig. 5.43 are overlaid. The labels in black text indicate spectral features not observed at 2 K, but seen at higher temperatures, while the blue labels are used to name the other emission lines. The most striking difference between the two spectra is that the intensity of A3 emission line increases markedly in comparison to the other features. The feature marked A5 is seen as a shoulder of the A6 emission line. This could be caused by line broadening; however, as seen in Fig. 5.43, the other emission lines do not seem to broaden as significantly as the temperature is raised from 2 to 20 K.

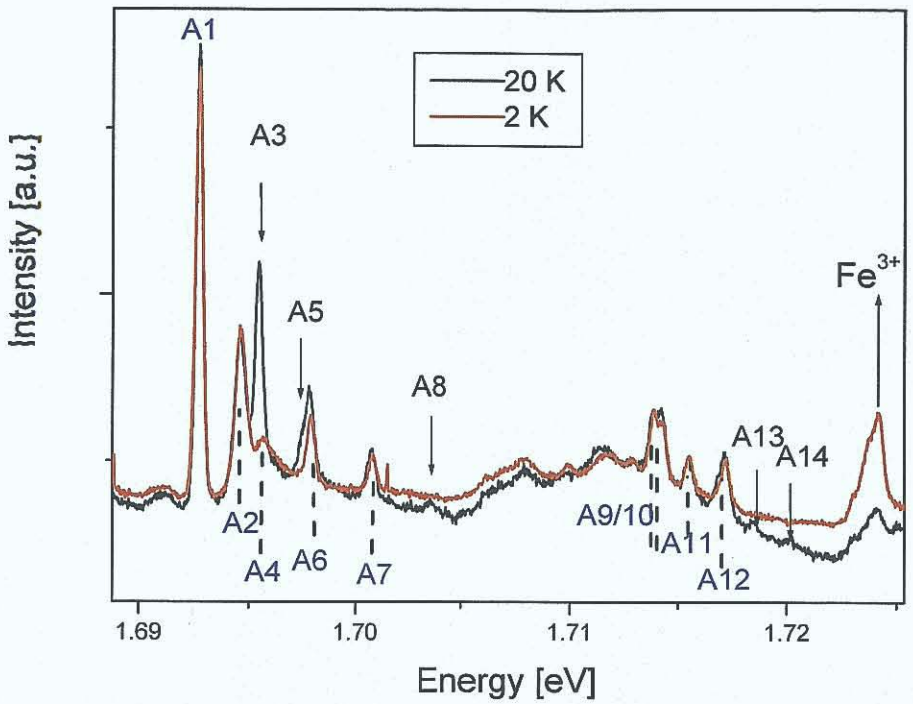

Figure 5.43: Overlapping spectra measured at 20 K (black line) and 2 K (red line). This figure demonstrates the change in the spectra obtained as the temperature is increased. The label Fe^{3+} is used to indicate a reported phonon replica of the Fe^{3+} emission line at higher energy

Table 5.3 gives the energy positions of the emission lines labelled in Fig. 5.43.

Label	Energy (eV)	Label	Energy (eV)
A1	1.6927	A8	1.7035
A2	1.6946	A9	1.7139
A3	1.6954	A10	1.7143
A4	1.6959	A11	1.7155
A5	1.6974	A12	1.7171
A6	1.6979	A13	1.7185
A7	1.7008	A14	1.7202

Table 5.3: Table listing energy positions of some of the sharp emission lines in the range 1.69 to 1.72 eV.

An attempt was made to analyse the features A1 and A3 in the same manner as performed for the L1/L2 and L3/L4 doublets. One of the difficulties found was that the weaker A4 line appears as a broadening of the A3 feature; therefore, it is likely that the intensity of this feature is over-estimated in the fitting procedure. This was compensated for by assuming that the intensity of A4 was temperature independent and subtracting the intensity of A4 at 2 K from the sum of A3 and A4 measured at higher temperatures. Figure 5.44 shows the energy region of interest between 2 and 10 K.

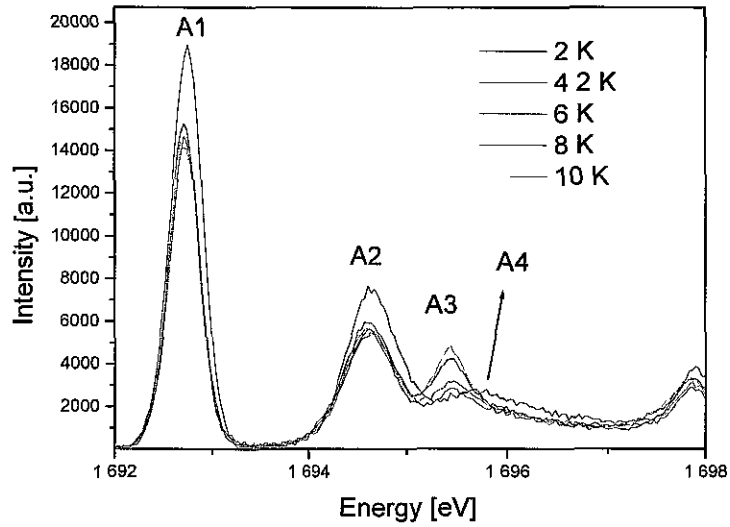

Figure 5.44. PL spectra at 2, 4.2, 6, 8, and 10 K. As can be seen, there appears to be two overlapping emission lines A3/A4 very close in energy

Figure 5.45 shows the fit to the natural log of the ratio of the intensities of the A3 to the intensity of the A1 feature as a function of inverse temperature. A fit to a linear plot gives an activation energy for A3 and A4 relative to A1 of 1.8 ± 0.1 meV, in comparison to the energy separation of 2.7 meV observed in the PL spectra. As in the case for the L_1 doublets, it is possible that the disagreement between the fitted values and the energy separation seen in the PL spectra is a result of laser heating.

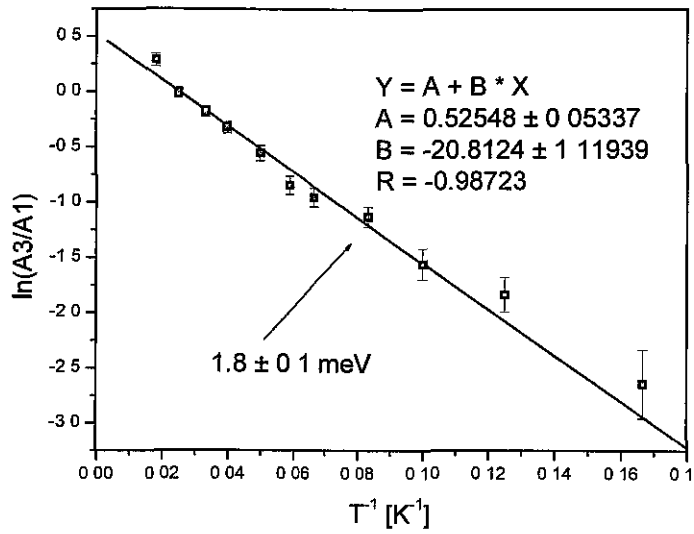

Figure 5.45: Arrhenius fit of the ratio of the intensities of the features A3 and A1 as a function of temperature The relationship between the two lines does not appear to be linear

The shift in energy of the A1 feature was plotted as a function of temperature and fitted using equation 5.4. The fit to equation gave a phonon energy of 16.3 ± 0.5 meV, in comparison to the observed phonon energy of 15.1 meV.

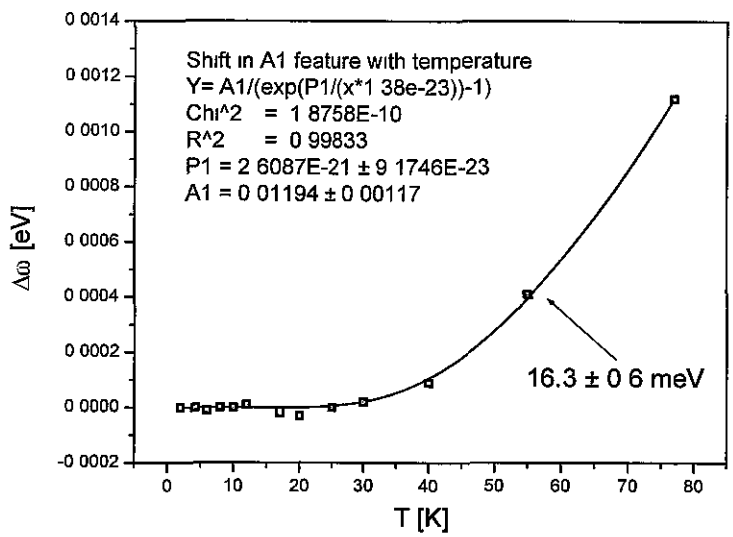

Figure 5.46: Change in energy of the peak position of the A1 feature as a function of temperature. A phonon energy of 16.3 ± 0.5 meV was obtained from this fit

Fitting the broadening of A1 to equation 5.2 yields a value of 11.4 ± 0.8 meV for the phonon energy, which is considerably different to the value found through fitting the shift in energy.

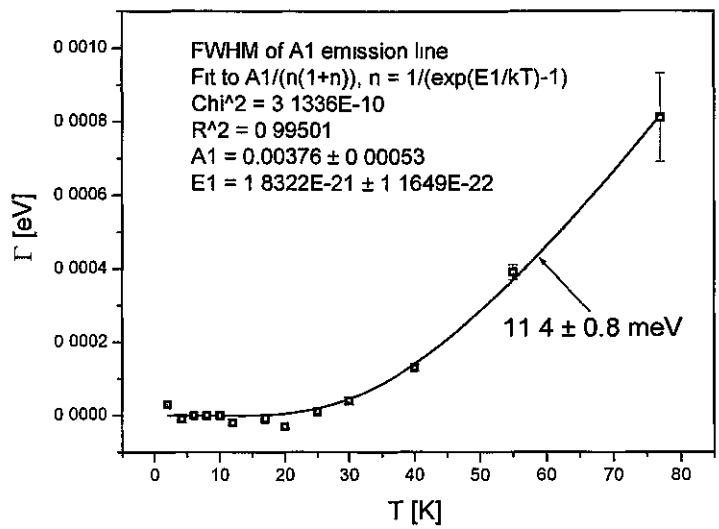

Figure 5.47: Change in FWHM of the A1 line as a function of temperature. A phonon energy of 11.4 ± 0.8 meV was obtained.

5.4 Conclusions

New features in the near IR were observed in single-crystal ZnO obtained from Rubicon Technologies, Inc. As shown in Fig. 5.16, the features observed in the IR are highly dependent on the excitation wavelength. Luminescence from Fe^{3+} defects are seen most strongly with excitation in the blue spectral region, while excitation with green light excites the "unidentified emission" more strongly than the Fe^{3+} emission. The behaviour of the new emission lines as a function temperature was studied. By examining how the intensity ratio between the lower energy line and the weaker higher energy feature varies with temperature, and accounting for laser heating of the samples by examining how this ratio varied with laser power, the difference in energy of the excited state was found to be 2.1 ± 0.2 meV for the first doublet and 2.0 ± 0.2 meV for the second doublet. As these separations are not the same as the energy separations seen in the PL spectra, a more complex defect system than the simplest split excited state to the same ground state could possibly be the case. However, constraining the fit to match the energy separation observed in the

PL spectra results in a close match to the data for the higher energy doublet at all but the lowest temperatures, indicating that the simpler model with transitions from two excited states to a common ground state could still be a good model for this defect system. Deactivation energies between 2.9 and 3.3 meV were found to fit the decrease in intensity of this emission with increasing temperature. At lower energy, another series of sharp emission lines are observed.

The appearance of the absorption features at ~1.88 eV along with the unknown IR emission at slightly lower energies led us to consider that these features could be related. A PLE experiment was performed in order to ascertain whether absorption in the red would lead to increased IR emission. The results of this experiment will be discussed in the next chapter.

References

1. R. S. Anderson, Phys. Rev., **164**, 398 (1967).
2. D. Lovy, Windig 5.5, http://www.unige.ch/sciences/chifi/cpb/windig.html, 21/08/06.
3. Mark A. Campo, Materials Science Engineer, Rubicon Technology, Inc., Private Communication.
4. R. Heitz, A. Hoffmann, I. Broser, Phys. Rev. B., **45**, 8977 (1992).
5. T. Monteiro, C. Boemare, M. J. Soares, E. Rita, E. Alves, J. Appl. Phys., **93**, 8995 (2003).
6. H. J. Schulz and M. Thiede, Phys Rev B, **35**, 18 (1987).
7. G. Davies, Phys. Rep., **146**, 83 (1989).

Chapter 6: Photoluminescence Excitation Experiment on the IR signals in ZnO

6.1 Introduction

Photoluminescence Excitation Spectroscopy (PLE) allows one to ascertain which absorption bands give rise to a particular emission feature. A variable excitation source is scanned typically over an energy range spanning from the band-gap energy of the material to the energy of the emission signal of interest, while a detector monitors the intensity of this emission signal. A sample energy diagram is presented in Fig. 6.1; a PLE spectrum of such a system would show three peaks representing each of the levels providing electrons to the emission level, E_1. The transition between the lowest excited state E_1 and the ground state result in the emission of photons with wavelength λ_0, which is observed in the PL spectrum.

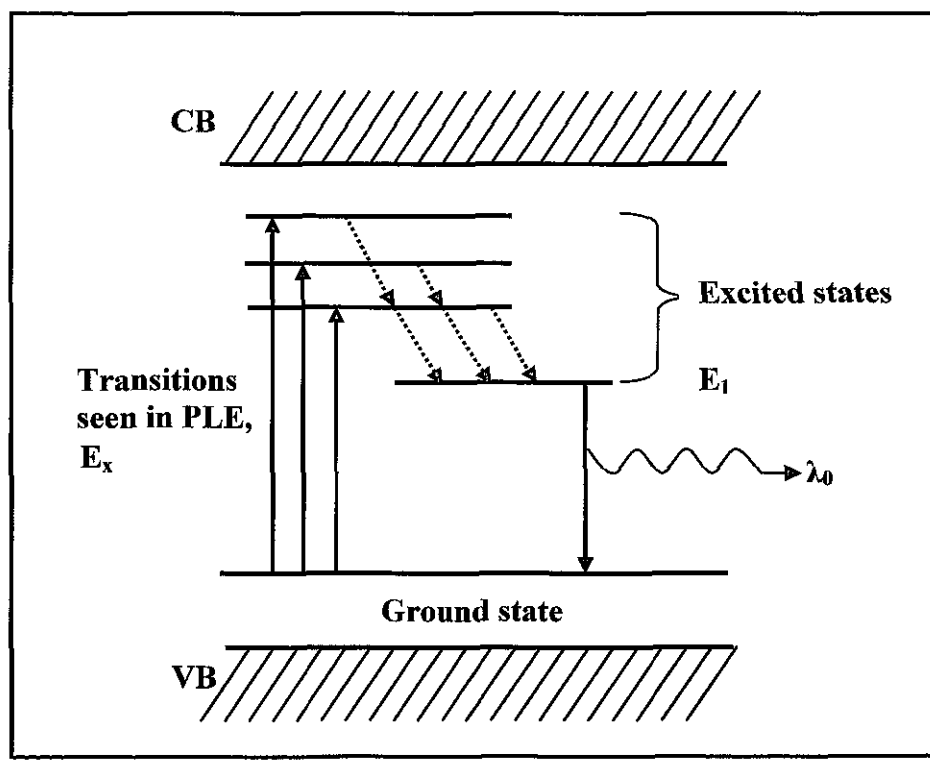

Figure 6.1: Diagram of PLE process. E_x represents the excitation energies that lead to luminescence at λ_0

One of the motivations for embarking on this experiment was to examine whether there is a relationship between the absorption lines in the red and any of the emission

signals in the IR as discussed in the previous chapter. This experiment may also help to separate out the two distinct sharp line signals (the Fe^{3+} emission and the other sharp line emission features) seen in the near IR region. If one signal was found to respond strongly to excitation with light of a particular wavelength, while the other had little response with the same excitation, this would help in distinguishing between the two "sharp" line signals and their respective phonon replicas.

6.2 Experiment Description

For the PLE experiment, an Ealing 150 W Xenon lamp was used as the excitation source. This was dispersed by a Spectra Pro 150 monochromator (Acton Research Corporation), the output of which was focused using lenses onto the sample. This monochromator could be controlled, via a PC, to scan over selected wavelength ranges at various speeds and with various wavelength increments. A Spex 1704 spectrometer was fixed at one of the emission peaks, while a Hamamatsu R3310-02 photomultiplier tube (PMT), operating in photon-counting mode, was used to monitor the variation in intensity of different emission signals as the excitation wavelength was varied. A wide bandpass filter, F1, was placed in front of the detector in order to prevent light from the excitation source from reaching the detector and influencing the PLE results. The filter used (KC15, Altechna) transmits light above ~ 640 nm. The experimental set-up is shown below in Fig. 6.2.

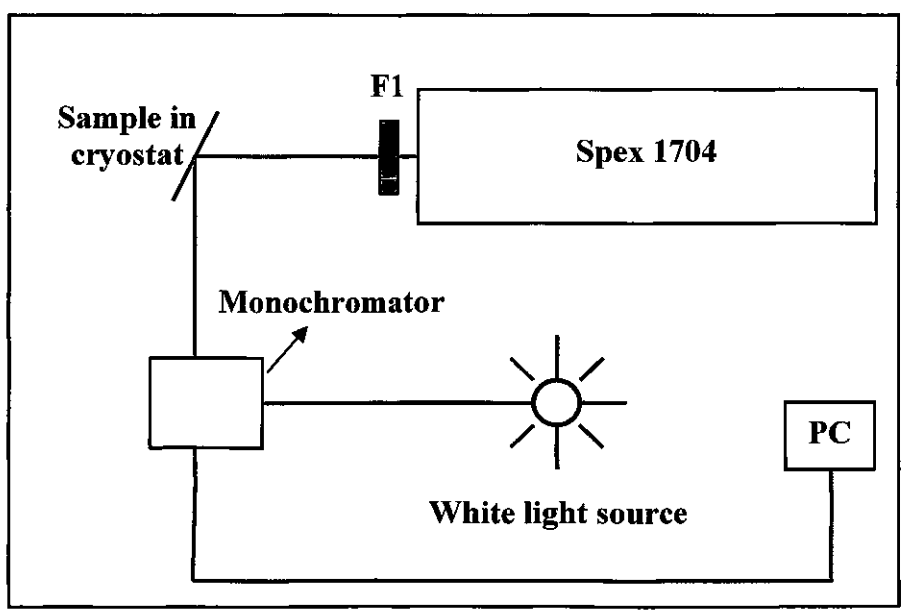

Figure 6.2: Schematic diagram of the experimental set-up used for the PLE experiment

One of the problems that arose during the PLE experiment was the difficulty in distinguishing which excitation energies affected the sharp line luminescence, such as the Fe^{3+} emission and L_1 lines, and which affected the underlying band. In order to overcome this problem, a phase sensitive detection (PSD) experiment was performed in order to attenuate this broad band signal. In Fig. 6.3 (Fig. 5.1 in the previous chapter), a PL spectrum showing the emission lines of interest is presented. As can be seen from this spectrum, the intensity of the underlying band at 10 K is higher than that of the sharp line emission features. Taking the intensity of the band at 1.76 eV, the relative ratios of the band in comparison to the intensities of the peaks at L1, L3 and Fe^{3+} is 1: 0.6: 0.4: 0.07.

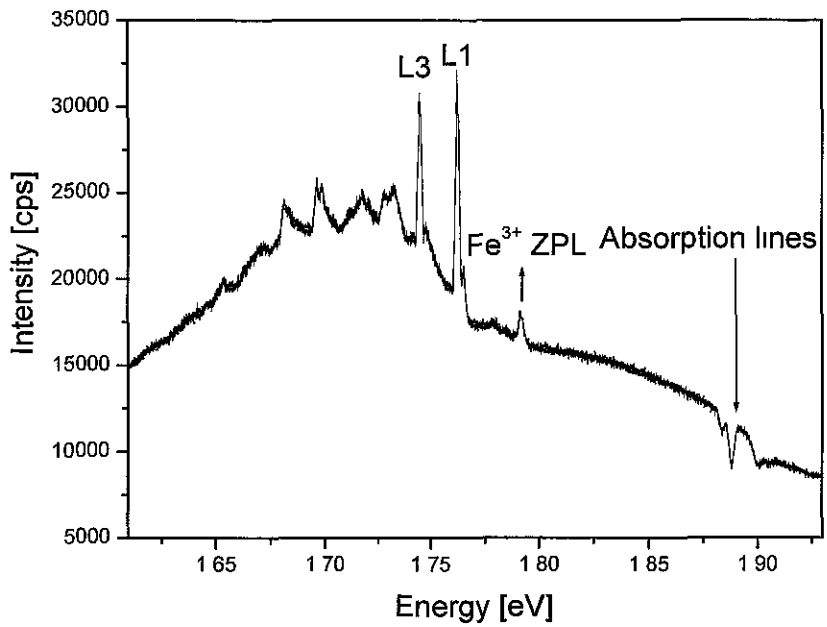

Figure 6.3: *As shown previously in Fig. 5.1, a number of sharp emission lines are observed on top of a broad band, peaking at ~1.7 eV. In order to separate the PLE results for these emission lines from the PLE results of the broad band, a phase-sensitive detection experiment was incorporated into the PLE apparatus*

For the phase-sensitive aspect of the experiment, the excitation source was chopped using a mechanical chopper (Scitec Instruments), and the resultant modulated luminescence signal, monitored by the PMT, was used as an input for a Lock-in-amplifier, LIA (EG&G Princeton Applied Research, model 5101). The chopper frequency was used as the reference signal. Noise is attenuated, as only signals

which have a frequency close to the reference signal will result in a non-zero output [1]. PL features with different radiative decay constants will have different phase relationships with respect to the reference signal. Since the output of the LIA is phase sensitive, only signals with a particular phase with respect to the reference signal will be observed [2]. Using the phase control in the LIA, the phase of the LIA can be varied to discriminate between input signals with different phase relationships, i.e. emission signals with different decay constants, with respect to the reference signal.

The output of the LIA is fed into the voltage input of the SpectrAcq2. The output of the LIA varies from 0-1 V. As the acquisition box can inputs ranging between ±10 V, the spectra acquired using this technique are significantly noisier than the other spectra presented in this chapter. Figure 6.4 shows the experimental set-up used to implement this technique.

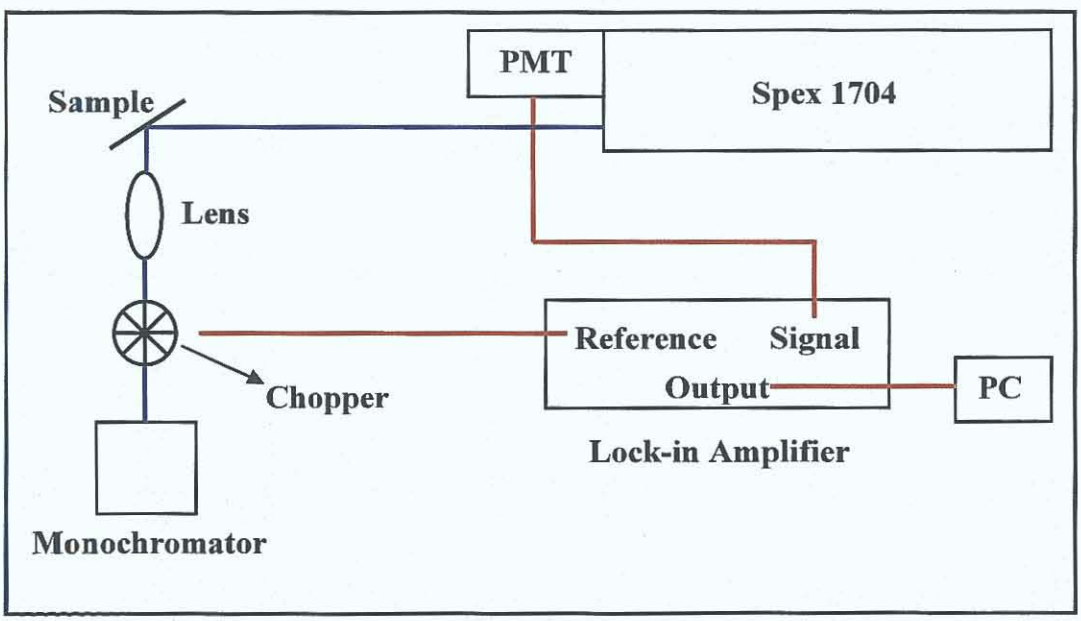

Figure 6.4: Schematic diagram of the experimental set-up for the phase sensitive detection measurements

6.3 Results

6.3.1 Photoluminescence Measurements

Before discussing the PLE data, a brief report on the PL spectra obtained for different excitation energies is provided. Excitation with blue light, 2.8-3.1 eV, led to strong Fe^{3+} emission, while excitation with light of an energy greater than the band-gap energy, resulted in intense luminescence for the broad band and the "unidentified" sharp line emission, L_1 lines. When other excitation wavelengths are used, the ratio between the features varies considerably. Photoluminescence spectra obtained using different excitation energy are presented in Fig. 6.5.

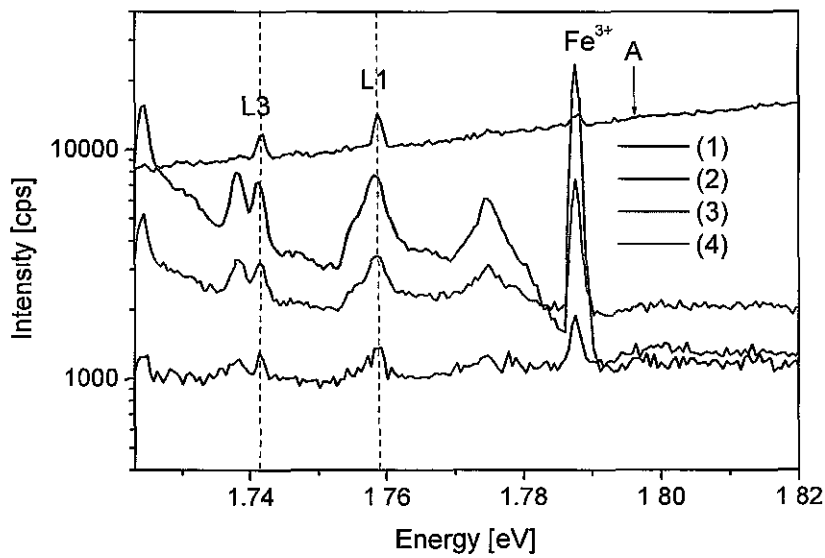

Figure 6.5: PL spectra under (1) 3.33, (2)3.01, (3) 2.70, and (4) 2.48 eV excitation

The various energy positions at which the spectrometer was fixed for the PLE measurements presented here are also indicated in Fig. 6.5. Point A indicates a position on the red band where no sharp lines were found. PLE measurements were taken at this energy in order to help differentiate between signals causing luminescence in the band and signals which cause the sharp line luminescence. The feature marked Fe^{3+} represents the ZPL of the Fe^{3+} emission at 1.7876 eV, while points L1 and L3 indicate the sharp features, observed at 1.7587 and 1.7415 eV respectively. As can be seen from the photoluminescence spectra, phonon replicas of

the Fe^{3+} emission (labelled 3 and 7 in [3]) are more intense than and very close in energy to the features marked L1 and L3 for a range of excitation wavelengths.

6.3.2 Photoluminescence Excitation Measurements

Figure 6.6 shows the spectra obtained, with a sample temperature of 18 K, when the spectrometer is fixed at (1) the ZPL of the Fe emission, (2) L1, and (3) L3, while the excitation energy is varied from 3.5-1.8 eV. With the spectrometer fixed at the energy position coinciding with the Fe^{3+} ZPL, we see that the most intense emission is seen with excitation with light of photon energy of 3.28 eV. Another peak is seen at 2.99 eV along with a shoulder at 2.64 eV. These last two features are also seen in the excitation spectra of the L_1 lines. However, the most intense absorption peak in this case is at a slightly higher energy than in (1), 3.32 eV. No features corresponding to the absorption features at 1.880 and 1.884 eV are seen in the excitation spectra of any of these emission lines.

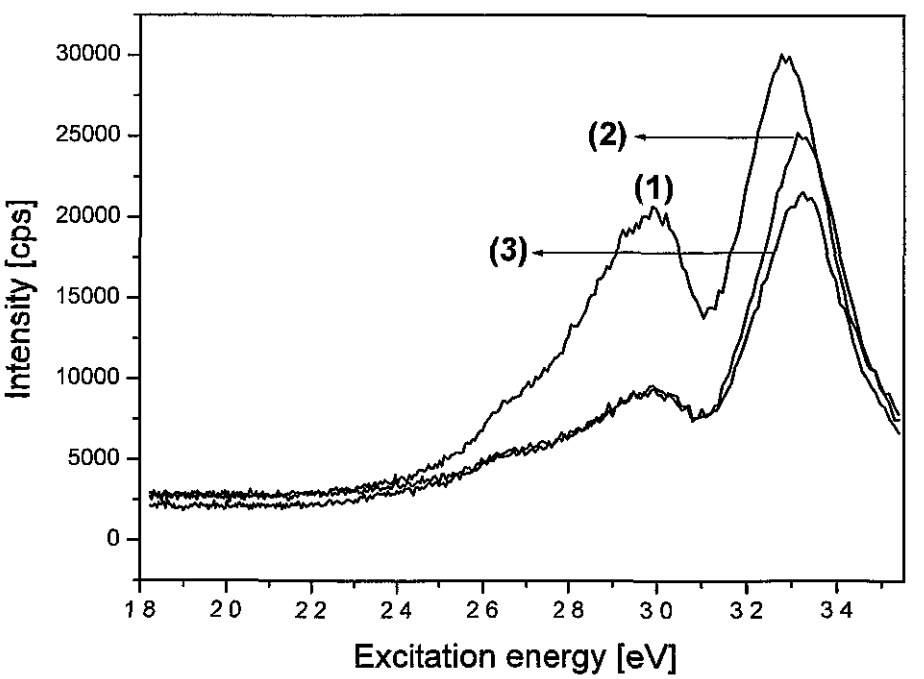

Figure 6.6: PLE taken at 18 K showing the PLE spectrum of the features at (1)1.788 eV-the Fe^{3+} ZPL, (2) 1.758 eV-L1 and (3)1.741 eV-L3. As can be seen in spectrum (1) the PLE results for the Fe^{3+} emission show a main peak at 3.28 eV at this temperature

PLE spectra for the same three emission lines taken at 7 K are shown below in Fig. 6.7. The main difference between the 7 and 18 K PLE spectra is that the ~3.01 eV peak for Fe^{3+} is much stronger at lower temperature. For L1 and L3, we see that the most intense peak is observed at 3.33 eV, with another peak at 3.03 and the same shoulder at 2.66 eV.

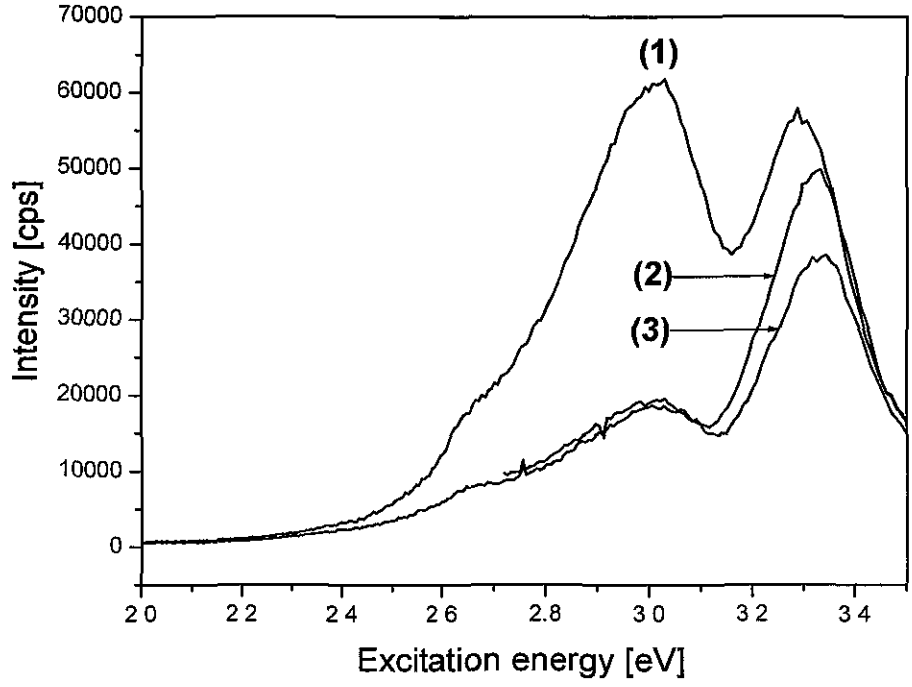

Figure 6.7 *PLE taken at 7 K showing the PLE spectrum of the features at (1)1 788 eV-the Fe^{3+} ZPL, (2) 1.758 eV-L1 and (3)1.741 eV-L3*

Figure 6.8 compares the PLE spectrum of the band, monitored at 1.8 eV as indicated in Fig. 6.5, with the spectrum of the Fe^{3+} ZPL. The main peaks seen in the excitation spectrum of the band (spectrum 2) are at 3.32 and 2.64 eV. The appearance of these peaks in the two spectra leads to the conclusion that these absorption energies increase the underlying band intensity rather than the sharp line emission intensity.

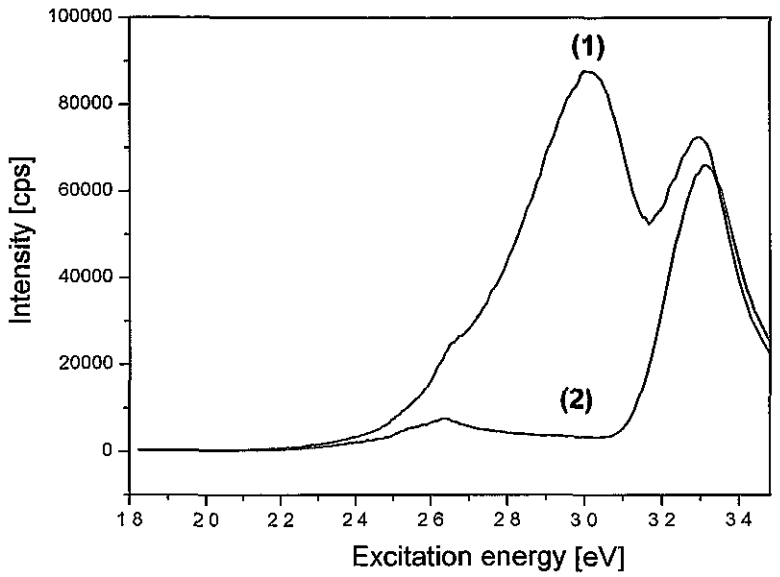

Figure 6.8: *PLE of (1) the ZPL of Fe emission and (2) broad underling band at 7K. The prominent 3.01 eV peak, seen in the excitation spectrum of the Fe^{3+} emission is not observed in the excitation spectrum of the band*

6.3.3 Phase Sensitive Detection Measurements

A phase sensitive detection experiment was incorporated into the existing experimental set-up, in order to attenuate the effect of the broad band luminescence. In Fig. 6.9, spectrum (1) shows the PL spectra obtained without phase sensitive detection. Here three signals can be seen on the uppermost spectrum, that of a broad red band, which peaks at 1.86 eV, the Fe^{3+} feature and the lines L1 and L3. Below this is a spectrum obtained using PSD with the phase adjusted to eliminate the broad underlying band. The resultant spectrum is a combination of the two sharp line signals. These two signals could not be separated out from each other, suggesting that they have similar decay constants. As a result, while it was relatively easy to obtain PLE spectra for the Fe^{3+} emission with the band removed by PSD, the effects of the phonon replicas of the Fe^{3+} emission could not be removed from the PLE spectrum of L1 and L3.

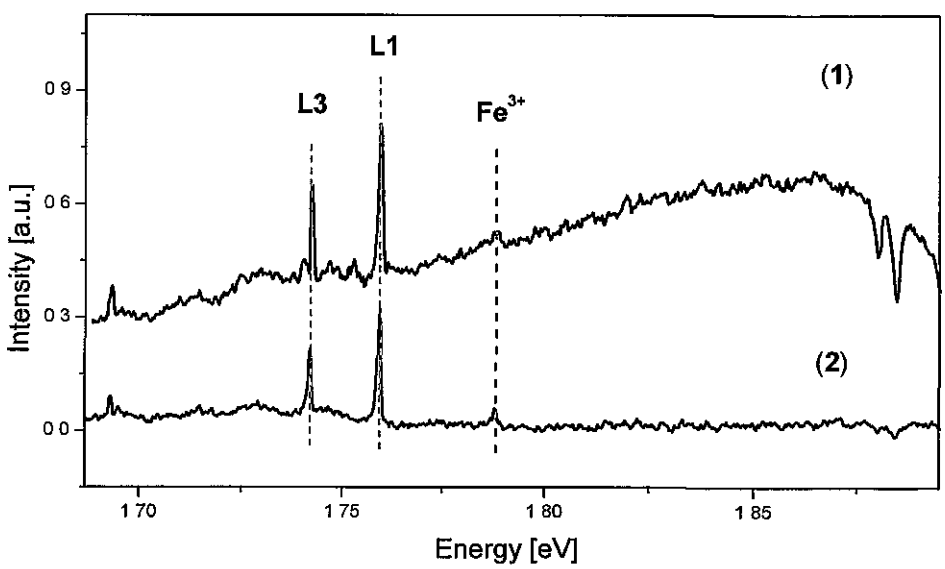

Figure 6.9: PL spectra obtained under excitation with the 532 nm line of a frequency-doubled Nd:YAG laser with spectrum (1) showing the sharp emission lines and the broad underlying band, and (2) showing the spectrum obtained after selecting the phase in such a way as to remove the band.

Figure 6.10 shows PLE spectra with the spectrometer fixed at the energy coinciding with the Fe^{3+} ZPL. The spectrum in red shows the results obtained using the LIA and choosing the phase condition that removes the underlying band, while the black

spectrum shows the PLE spectrum of both the sharp line emission and the broad band. When the band is not detected, the absorption peak at 3.3 eV is not observed. However, the absorption peak at 3 eV is seen, suggesting that the Fe^{3+} emission is excited by the absorption of energy at 3 eV but not with energy greater than the band-gap energy.

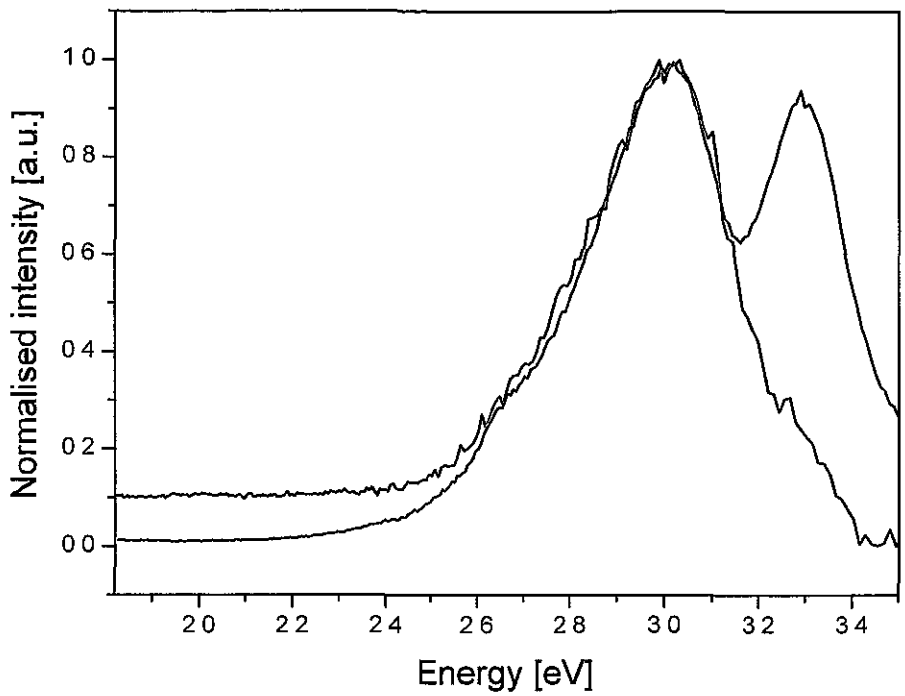

Figure 6.10: PLE spectrum with spectrometer fixed at Fe^{3+} ZPL emission peak at 7 K. The spectrum in red shows the excitation spectrum obtained with the phase chosen to reject the broad band luminescence, while the spectrum in black shows the spectrum obtained with the detector monitoring both the sharp emission feature and the underling band

Figure 6.11 shows the temperature dependence of the PLE on the Fe^{3+} peak at 1.7876 eV, with the band removed by phase sensitive detection. As can be seen, increasing the temperature causes a sharp reduction in signal.

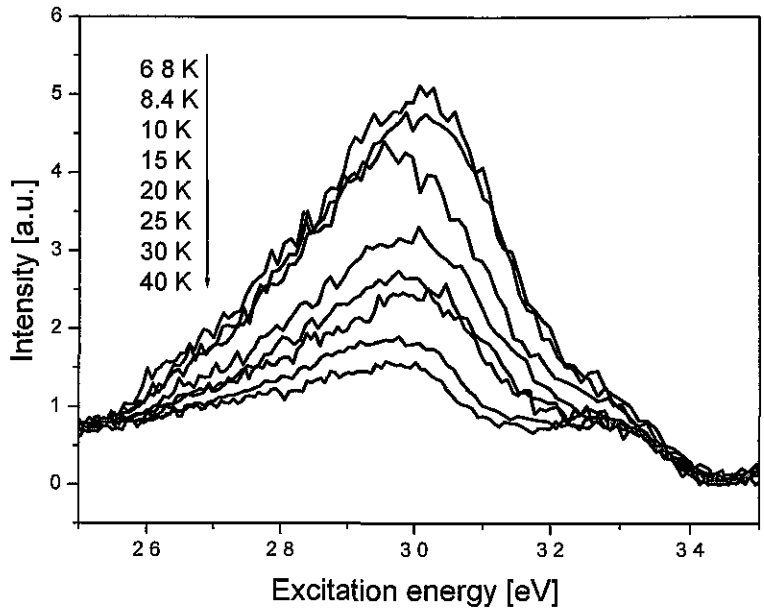

Figure 6.11: Temperature dependence of the PLE signal for the Fe^{3+} emission. A sharp decrease in the intensity of the excitation signal is observed as the temperature is increased

The maximum intensity of the PLE peak was recorded at each temperature and plotted against temperature. The data was fit using equation 6.1, and a value of 2.8 ± 0.2 meV was obtained for the deactivation energy, E_1.

$$\ln\left(\frac{I_{\max}}{I(T)}-1\right)=\ln C_2-\frac{E_1}{k_B T} \qquad \textbf{6.1}$$

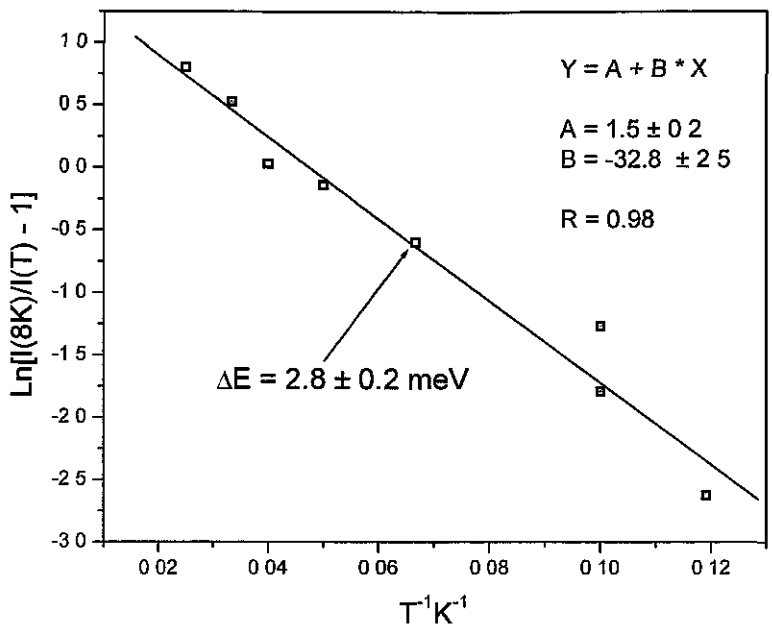

Figure 6.12: Plot of peak intensity against temperature. A value of 2.8 ± 0.2 meV was found to fit the data

The deactivation energy obtained for the excited state at ~3.01 eV is very low; a large drop in intensity is seen in the excitation spectra with a moderate increase in temperature. One of the possible reasons for this is that the lifetime of the corresponding luminescent feature is changing with increased temperature, the phase setting of the LIA being unchanged as the temperature is increased. Time resolved measurements performed by Heitz *et al.* [3] observed a decay constant of 25.2 ms. It is not entirely clear at what temperature these measurements were performed, but all the measurements in this work were made at either 1.8 or 4.2 K. Measurements of the decay constant were also made by Monteiro *et al.* [4] at 14 K. Here, the transient response of the Fe^{3+} emission could be fit to a bi-exponential decay of 1.4 and 23 ms.

In order to ensure that a change in lifetime of the Fe^{3+} transition is not the cause of the observed rapid decrease in intensity with respect to increased sample temperature in Figs. 6.11 and 6.12, these data were compared to PLE data as a function of temperature. These spectra show absorption energies that excite both the broad band and the Fe^{3+} feature over a temperature range 8 to 55 K and have not been normalised. The spectra in Fig. 6.13 were taken over several days, and as there could have been slight changes in sample orientation, lamp output power and the alignment

of the source, focusing lenses, etc. between measurements, there is considerable variation in the spectra. For example, the PLE intensity at 10 K for the lower energy peak at 3 eV, which we know from the PSD measurements is Fe^{3+} rather than band related, is significantly more intense than the corresponding peak at 8 K. This conflicts with data seen from PL studies which shows that the luminescence signal decreases with increasing temperature.

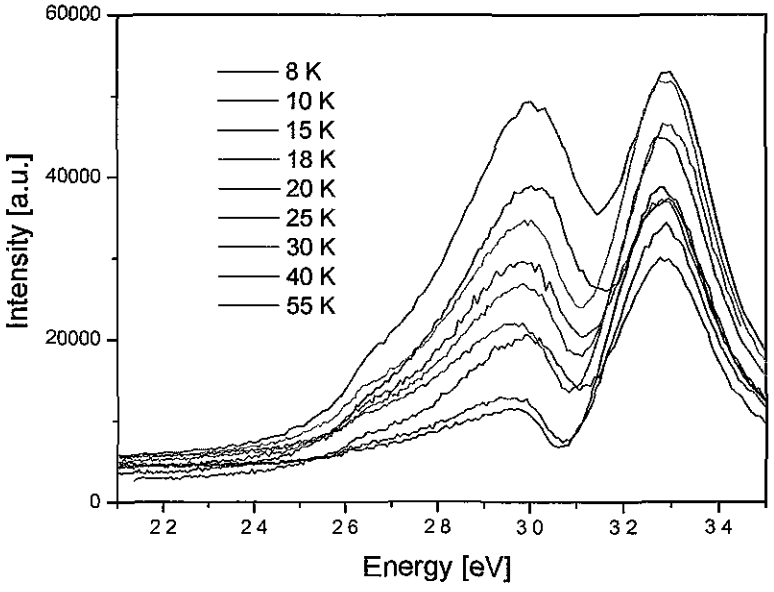

Figure 6.13: PLE spectra with the spectrum fixed at the energy coinciding with the position of the Fe^{3+} ZPL over a range of sample temperatures from 8 – 55 K

To take account of such variations, the data were normalised to the intensity at ~3.3 eV, as shown in Fig. 6.14. Using this normalisation, the data appear to follow the expected trend with temperature. As can be seen from these spectra, the absorption energy corresponding to the band exciting the Fe^{3+} defect decreases in intensity more quickly than the levels contributing to the broad band luminescence. The results of the fit of the band at 3 eV to equation 6.1 is shown in Fig. 6.15. A deactivation energy of 3.8 ± 0.1 meV was obtained which is in good agreement with the value obtained in Fig. 6.12, lending doubt to the concern that the lifetime of the transition changes significantly over the studied temperature range.

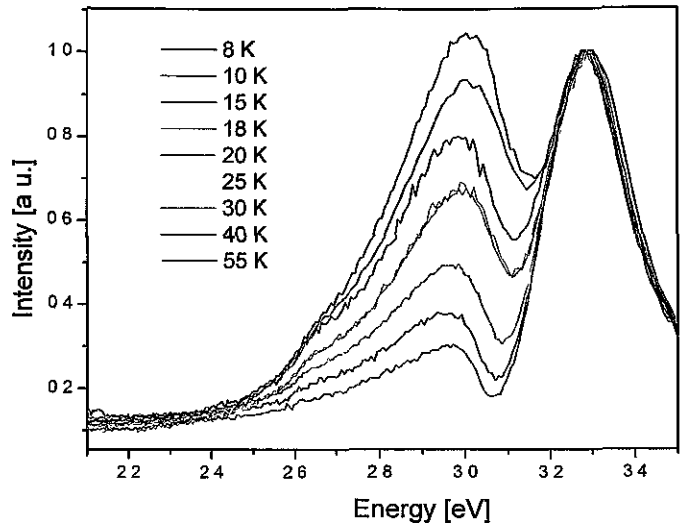

Figure 6.14: Excitation spectra of the band and Fe^{3+} feature normalised to the above band-gap absorption intensity at 3.30 eV

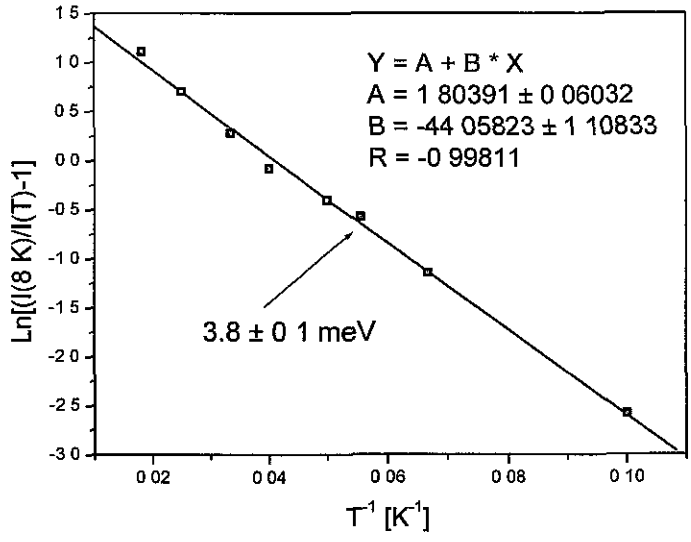

Figure 6.15: Behaviour of integrated intensity of the band peaking at 3 eV with increasing temperature and fit to equation 6.1

6.3.4 Modelling the Fe^{3+} emission

The excitation of this defect was attributed to an energy transfer of holes with an Fe^{2+} ion, the holes being photo-generated from a deep acceptor with an ionisation energy greater than 2.25 eV [3], analogous to the case of Fe^{3+} in ZnS [5]. In ZnS, excitation with light of energy 1.174 eV changes the charge state of Cu from Cu^{2+} to Cu^{+} leaving a hole in an excited state close to the VB edge; excitation with light greater than 1.28 eV creates the Cu^{+} centre along with a hole in the valence band. This hole can then become trapped at an Fe^{2+} site, changing the charge site from 2^{+} to 3^{+}. A similar mechanism has been suggested for ZnO: Fe^{3+} [3], although the acceptor, A, in this case has not been identified. Overall, the process can be described by the following:

$$Fe^{2+} + A^{0} + \hbar\omega_{blue} \rightarrow Fe^{2+} + A^{-} + h_{VB}$$
$$\rightarrow Fe^{3+}\left({}^{4}T_{1}(G)\right) + A^{-}$$
$$\rightarrow Fe^{3+}\left({}^{6}A_{1}(S)\right) + A^{-} + \hbar\omega_{red}$$
$$\rightarrow Fe^{2+} + A^{0}$$

The final state requires the transfer of an electron back to the Fe^{3+} ion to recreate the Fe^{2+} initial state. These processes are illustrated in the following energy level diagram where $*Fe^{3+}$ indicates an excited state of Fe^{3+}.

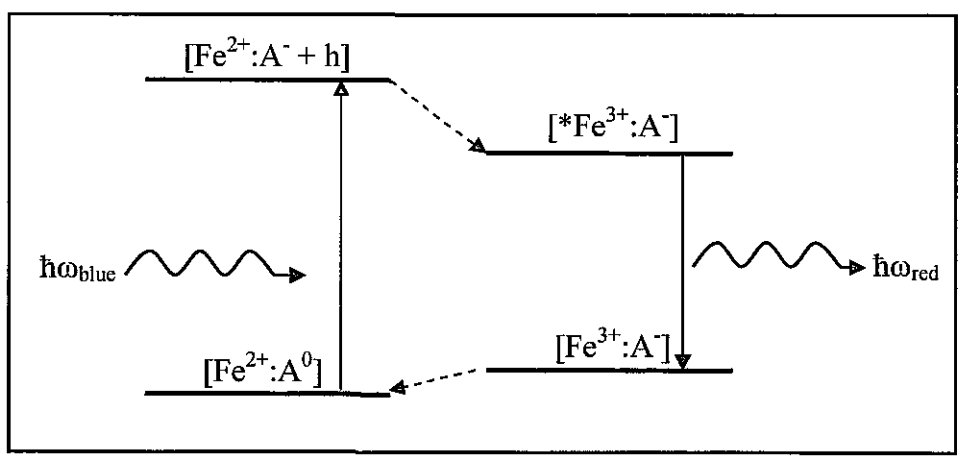

Figure 6.16: Schematic diagram of a possible PLE mechanism

This schematic energy level cannot be considered as definitive given the sparse data available at this time. The [Fe^{3+}: A^{-}] state could lie lower or higher in energy than [Fe^{2+}:A^{0}]. If [Fe^{3+}: A^{-}] is lower, then PL excited via the [Fe^{2+}:A^{0}] to [$*Fe^{3+}$: A^{-}]

process should increase with temperature. However, if [Fe^{3+}:A^-] lies above [Fe^{2+}:A^0], and PL is excited only via the [Fe^{2+}:A^0] to [*Fe^{3+}: A^-] process, then the PL intensity should decrease as temperature is raised due to the reduction of the [Fe^{2+}:A^0] initial state population. However, there may also be direct excitation from [Fe^{3+}:A^-] to [*Fe^{3+}:A^-] and PL resulting from such an excitation process would increase with temperature if the [Fe^{3+}:A^-] population increased (assuming no other temperature dependence effects are at play).

We now consider possible candidate acceptor impurities/defects for processes such as those illustrated above. Known deep acceptors in ZnO include Li, Ag, Cu, Zn-vacancies and O-interstitials. The Li acceptor is thought to have an acceptor level at ~0.8 eV above the valence band [6]. Zwingel observed that the decrease in intensity of the yellow Li-related band coincided with an increase in the Fe^{3+} EPR signal and attributed this to the release of holes bound to the substitutional Li acceptor being trapped at an Fe^{2+} centre. Kanai [7] reported a deep acceptor level at 0.23 eV below the conduction band for Ag through admittance spectroscopy measurements, while Dingle *et al.* calculated an energy level for the (Cu^+, h) level at 0.45 eV above the valence band [8]. Recent LDA calculations performed by Janotti and Van de Walle [9] place the Zn vacancy levels ε(0/-) and ε(-/2-) at 0.11 and 0.51 eV above the valence band maximum, respectively. If the Jahn-Teller distortion is similar to that observed for V_{Zn}^- in ZnSe, this would place the ε(-/2-) level at approximately 0.9 eV above the valence band. This Jahn-Teller effect causes a hole to be located on one of the surrounding O-atoms, which then relaxes towards the vacancy, lowering the energy of the vacancy. Similar results were obtained in an earlier study by Kohan *et al.* [10]; here, the ε(0/-) and ε(-/2-) levels for the Zn vacancy were found to lie at approximately 0.3 and 0.8 eV above the valence band, respectively. For the O_i, Janotti and Van de Walle found that only the interstitial on an octahedral site formed a stable acceptor level. The transitions ε(0/-) and ε(-/2-) were found to have levels at 0.57 and 1.18 eV above the VB, respectively, which compares well to the values of 0.4 and 1.1 eV calculated by Kohan *et al.* for oxygen rich material. Figure 6.17 shows the position of energy levels of various acceptors in the band-gap of ZnO.

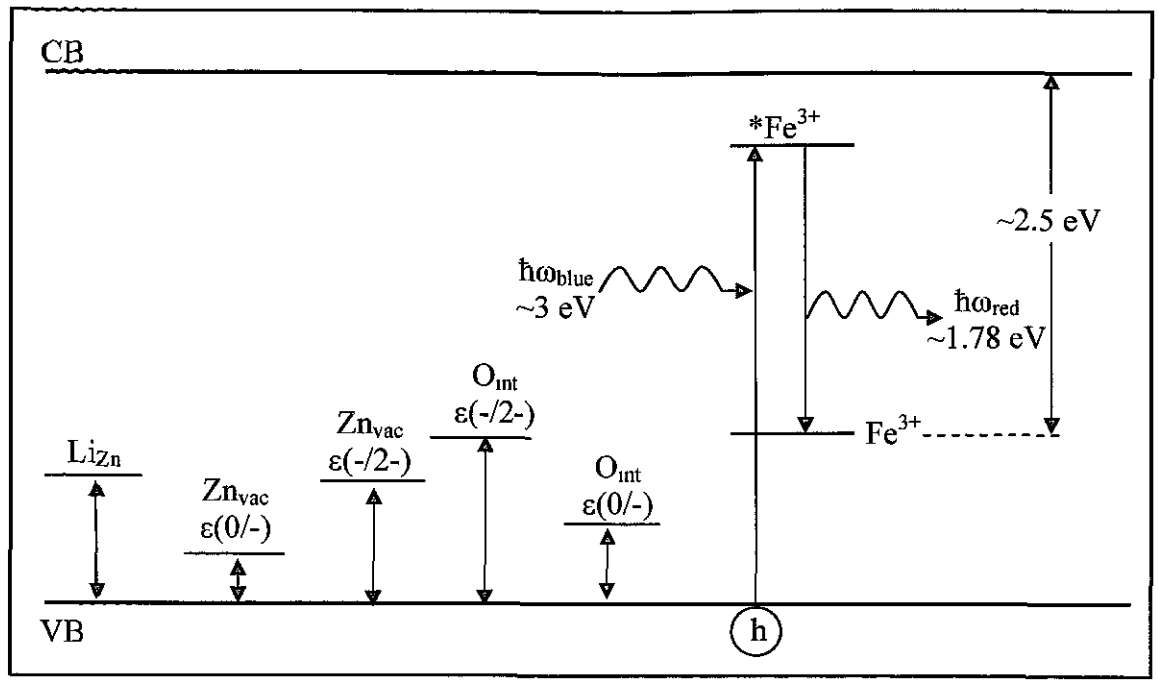

Figure 6.17: Schematic diagram of position in the band-gap of various acceptor levels in ZnO along with a possible placing of the ground and excited states of the Fe^{3+} defect

We have included on the extreme right of Fig. 6.17 a possible placing of the Fe^{3+} ground and excited states. The excited state $*Fe^{3+}$ is placed ~3eV above the VB edge, corresponding to the energy of the blue light of the PLE maximum. The Fe^{3+} ground state then lies ~2.5 eV below the CB edge. We note that this energy corresponds to the threshold of the PLE spectrum, which could be due to direct electron excitation from Fe^{3+} into the CB, which subsequently leads to PL emission. This means that the PLE spectrum could be produced by a superposition of charge transfer processes and direct excitation of the Fe^{3+} ions.

Regarding possible acceptors involved in this, we note that Li is a possible contaminant in the Rubicon samples as they are hydrothermally grown; however, similar PLE spectra were reported by Heitz *et al.* [3] and Monteiro *et al.* [4] in vapour phase grown ZnO. Li is not generally an impurity associated with this growth method. It is possible that Li could be introduced through the annealing process in [4], but the samples used in [3] contained Fe as an unintentional contaminant. It is

probably unlikely, therefore, that Li is the acceptor involved in this hole transfer excitation mechanism.

6.3.5 PLE of L1/L3

While PSD can successfully be used to discriminate between the Fe^{3+} emission and the underlying band, similar spectra could not be obtained for the emission signals L1 and L3 due to the difficulty in separating this emission from the phonon replicas of the Fe^{3+} emission under particular excitation conditions. Even with PSD, PLE spectra would show the excitation energies leading to emission of the Fe^{3+} defect and the "unidentified defect". In order to overcome this problem, two techniques were used to ascertain the response of the emission features at L1 and L3 to different excitation energies.

Technique 1

For the first experiment, PL measurements were taken at the same temperature as the PLE scans in order to determine the ratio between the intensity of the ZPL of the Fe^{3+} emission and its phonon replica at the particular temperature in question. The excitation energy used was 3 eV, and the results presented in Fig. 6.11 show that the intensity of the Fe^{3+} emission is high under this excitation. The PLE spectrum for the Fe^{3+} ZPL was then normalised by this ratio, and this normalised spectrum was then subtracted from the PLE spectra of the features L1 and L3. For example, the PL spectrum at 18 K, shown in Fig. 6.18, shows that the ratio between the Fe^{3+} ZPL and its phonon replica at L1 is 2.12:1. The PLE spectrum of the Fe^{3+} emission was divided by 2.12, and subtracted from the PLE scan with the spectrometer fixed at L1. Figure 6.19 shows the spectra acquired using this technique for L1 and L3. This is obviously not an ideal way to do this but the results obtained seem to mirror what is seen in the PL spectra. A baseline indicating zero intensity is drawn in this figure. These spectra show the PLE results for the emission lines L1 and L3.

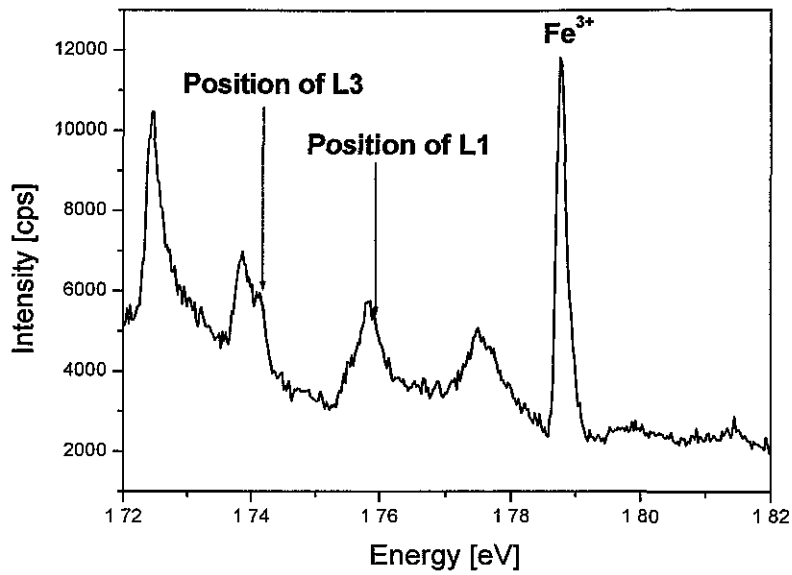

Figure 6 18: PL spectrum at 18 K with excitation with light of photon energy 3.02 eV. The relative intensity of the Fe^{3+} ZPL to the intensity at the energy positions corresponding to L1 and L3 are 2.12 and 2.10 respectively

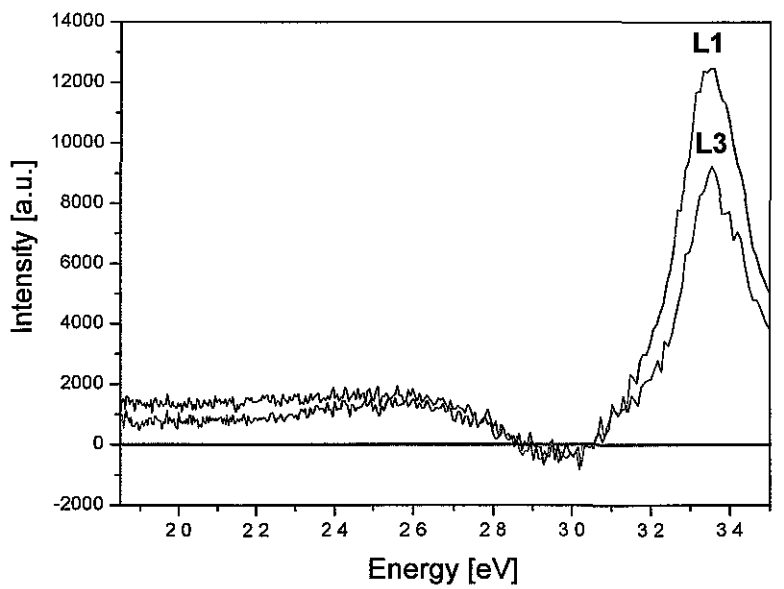

Figure 6.19: Spectra showing the PLE spectrum obtained after subtracting the effects of the Fe^{3+} phonon replicas. A line representing a zero count reading is drawn

Technique 2

The next technique involved taking PL measurements over a range of excitation energies from 3.5 to 2.3 eV, and calculating the intensity of the L3 and L1 lines. The method used to determine the intensity involved removing a baseline, to nullify the effect of the underlying band intensity, and fitting a Lorentzian to calculate the area under the lines L1 and L3.

In order to check whether this technique is valid, the same analysis was done for the Fe^{3+} emission and compared with the results obtained from the phase sensitive detection measurements described in the previous section. The results for this analysis are shown in Fig. 6.20. Here, spectrum (1) shows the PLE results for Fe^{3+} emission obtained with PSD, while spectrum (2) shows the results of a plot of the integrated intensity of the emission line versus excitation wavelength. The PL data were taken with a greater resolution than the PSD measurements as the signal-to-noise was poor for the PSD measurements. The effect of this is seen with the narrower linewidth of the band peaking at 3.02 eV in spectrum (2).

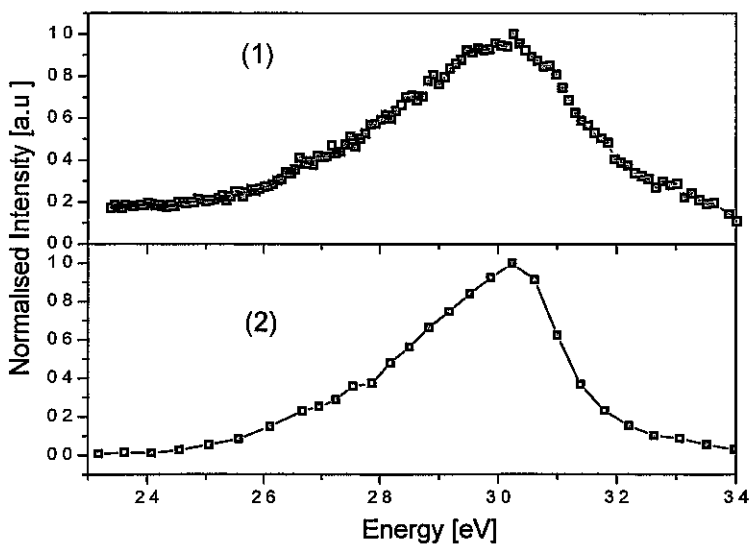

Figure 6.20: Comparison between PLE results using (1) PSD and (2) PL on the Fe^{3+} emission

A sample of some of the PL results used to construct the data plotted in Fig. 6.20 is shown below in Fig. 6.21.

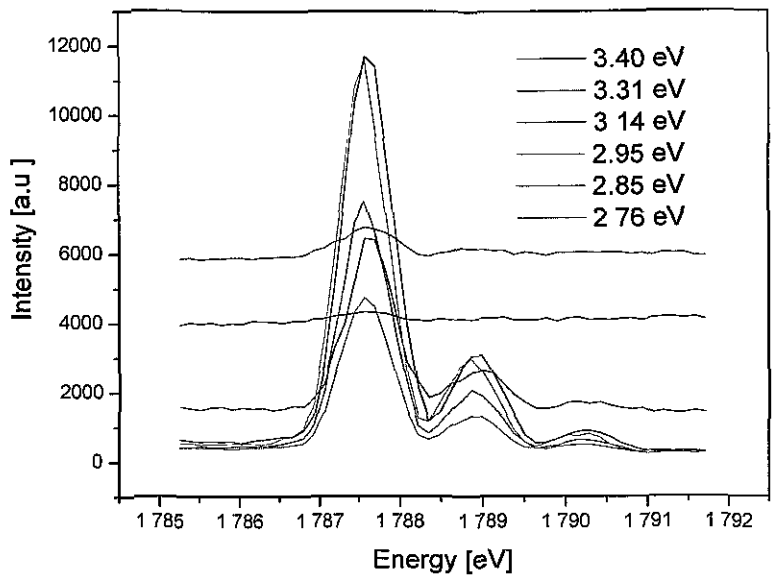

Figure 6.21. PL spectra for a variety of excitation energies at 13 K over an energy range encompassing the Fe^{3+} ZPL

As there was good agreement between the PLE results for the Fe^{3+} emission acquired by the technique of integration and those obtained through PLE/PSD, it was decided to attempt to analyse the excitation spectrum of the emission features L1 and L3 in the same way. Figure 6.22 shows the results obtained. A peak signal is seen between 3.35 and 3.4 eV. For excitation between 2.6 and 3.25 eV, the luminescence related to L1/L3 could not be distinguished from phonon replicas of the Fe^{3+} emission. These emission features become apparent, though weak, for excitation in the range 2.3 to 2.6 eV.

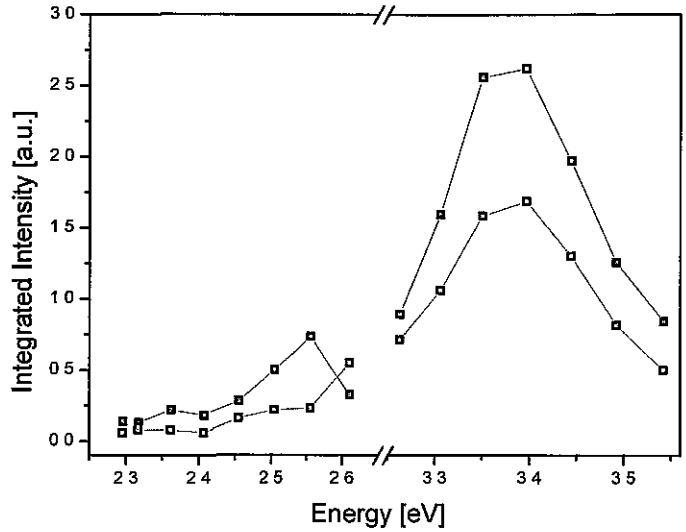

Figure 6 22: Spectra showing effect of changing the excitation energy has on the PL intensities. The x-axis shows the excitation energy, while the y-axis shows the integrated feature of L1 (in black) and L3 (in red)

Figure 6.23 shows the PL spectra obtained for excitation energies ranging from 3.5 to 2.3 eV. With excitation energies less than 3.4 eV, the intensity of both the broad band and the emission lines L1 and L3 decrease.

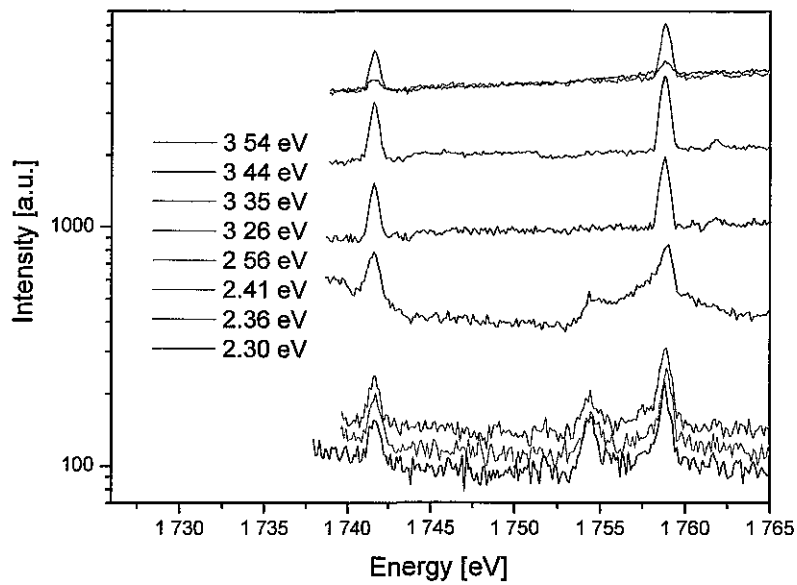

Figure 6.23: PL spectra for a variety of excitation energies at 13 K

Figure 6.24 further shows the difficulty in measuring the integrated intensities of L1/L3 over the range 2.3 to 2.6 eV. The upper spectrum shows the strong response of the Fe^{3+} defect to excitation with light of photon energy 3.1 eV. The lower spectrum shows a smaller range and compares the spectra obtained under excitation of 3.1 and 3.35 eV. The data here have been scaled so that the two spectra overlap in order to show how close in energy the features L1/L3 are to the phonon replicas of the Fe^{3+} defect.

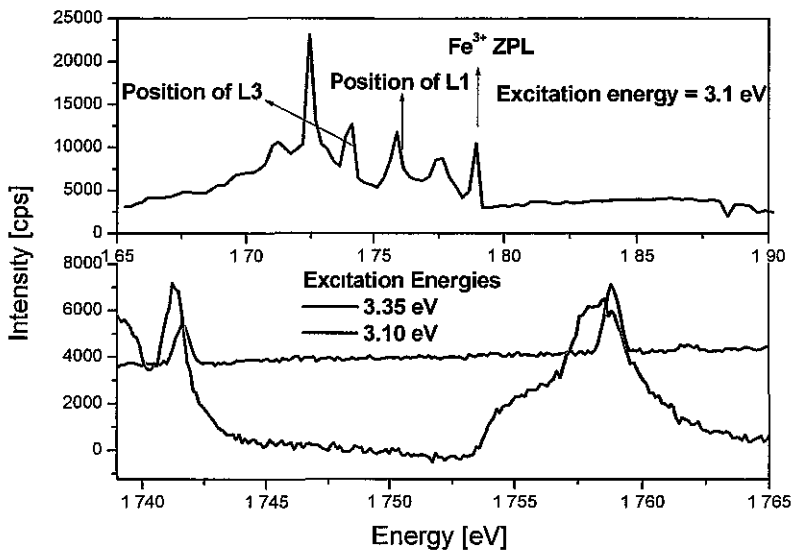

Figure 6 24: Upper spectrum: PL scan excited with light of photon energy 3.1 eV. Lower spectrum: Comparison between PL spectra obtained using different excitation energies. As can be seen, L1 and L3 cannot be resolved from phonon replicas under excitation with light of photon energy 3.1 eV

6.4 Conclusions

No obvious relationship between the absorption lines in the red and any of the IR emission signals could be found through the photoluminescence excitation measurements. The results show that the absorption energies that strongly affect the three emission signals in the IR are very different. PLE spectra of the Fe^{3+} emission show an increase in emission as the excitation energy is reduced from above band-gap light to a peak response at 3.02 eV. The broad band emission and the features L1 and L3 show a peak response with above band-gap illumination. A PSD experiment

was incorporated with PLE in order to distinguish between the PLE spectra of the underlying broad band and the Fe^{3+} emission. These results show that the PLE peak at 3.5 eV, as seen in the spectra taken without PSD, contributes to the band rather than this emission. Attempts to decipher the excited states of the emission features L1 and L2 were made through manual subtraction of the contributions of the Fe^{3+} phonon replicas, and also examination of the PL intensities at various excitation energies. Although, the data are crude they give an indication of the excitation energies contributing to this emission. Further work with samples without Fe contamination would help in understanding the properties of this defect.

References

1. B. Lawless, Fundamental Analog Electronics ((Prentice Hall, London-New York, 1997), Chapter 51, 256.
2. B. Henderson and G. F. Imbusch, Optical Spectroscopy of Inorganic Solids (Clarendon Press, Oxford, 1989), Chapter 6, 264.
3. R. Heitz, A. Hoffmann, I. Broser, Phys. Rev. B., **45**, 8977 (1992).
4. T. Monteiro, C. Boemare, M. J. Soares, E. Rita, E. Alves, J. Appl. Phys., **93**, 8995 (2003).
5. A. Hoffman, R. Heitz, I. Broser, Phys. Rev. B, **41**, 5806 (1990).
6. D. Zwingel, J. Lumin., **5**, 385 (1972).
7. Y. Kanai, Jap. J. Appl. Phys., **30**, 2021 (1999).
8. R. Dingle, Phys. Rev. Lett., **23**, 579 (1969).
9. A. Janotti, C. G. Van de Walle, J. Crys. Gr., **287**, 58 (2006).
10. A. F. Kohan, G. Ceder, D. Morgan, C. G. Van de Walle, Phys. Rev. B, **61**, 15019 (2000).

Chapter 7: Damage-related emission lines in ^{107}Cd- and ^{7}Be-implanted samples

7.1 Introduction

Implantations of ^{107}Cd and ^{7}Be isotopes were also performed. Both these elements are isoelectronic if substituting for Zn. Isoelectronic dopants may act as donors or acceptors if there is a difference in the electronegativities between the dopant and the host atom. If the dopant is more electronegative it can act as an acceptor; if less, a donor [1]. Lattice distortion caused by differences in covalent radius is also thought to play a role as only dopants which have significantly larger or smaller covalent radii in comparison to the host atom have resulted in an optical signal [2]. Only two studies have shown optically active isoelectronic impurities which substitute for the cation [3, 4]. Agne *et al.* [3] observed luminescence in Hg doped ZnO which appeared similar to spectra related to isoelectronic impurities reported for other materials, while Seong *et al.* [4] observed bound exciton emission lines related to isoelectronic Ca, Ba and Sr in ZnTe. Table 7.1 shows electronegativities and covalent radii for Zn, Cd, and Be and those elements in [3, 4] taken from [5]. As the covalent radius of Cd is the same as Hg, where an isoelectronic state is observed in ZnO, and the difference between the covalent radius for Be and Zn is even greater, it was decided to implant these isotopes to see if any optical emission related to these elements could be observed.

The daughter products of both of these isotopes are also potential acceptors, though both are believed to have energy states deep in the band gap of ZnO with Ag having an energy level 0.23 eV below the conduction band [6] and Li having an energy level of approximately 0.8 eV above the valence band [7]. A particular problem with both Ag and Li doping is that these elements are believed to favour a site other than a Zn-substitutional site, with Li taking an interstitial site [7] and Ag found to be located at large displacements from the Zn-site from emission channelling measurements [8]. Wahl *et al.* [8] suggested that the deep acceptor level formed by Ag could be related to a complex with this defect rather than a simple substitutional acceptor, while Zwingel [7] suggested that equal concentrations of substitutional and interstitial Li

were formed along with a second Li acceptor, $(Li_iLi_sO)^-$, with a concentration of ~1% of the total Li concentration, to explain the observed change in conductivity as a function of Li concentration. As the recoil energy of the daughter products is low, it is likely that they should form substitutional defects if the mother isotopes do.

Element	Electronegativity (Pauling Scale)	Covalent Radius (nm)	
Zn	1.65	0.131	
Cd	1.69	0.148	TW
Be	1.57	0.106	TW
Hg	2.00	0.148	[3]
Ca	1.00	0.106	[4]
Sr	0.95	0.127	[4]
Ba	0.89	0.143	[4]

Table 7.1: Electronegativity and covalent radii values for implanted ions and those observed to act as isoelectronic dopants in the literature

For both implantations, a series of emission lines were found to lie between the donor bound exciton region and the two-electron satellite (TES) region, with some of these features occurring in both samples. These features are similar to acceptor and isoelectronic pair spectra reported in the literature for other semiconductors [9, 10]. These signals did not change in intensity with the decay of the implanted species, suggesting that they are related to some form of implantation damage. It is possible that these emission features are a common feature in implanted material; they have a much lower intensity than surrounding signals and this region was only examined carefully after the observance of an optical signal that appeared to increase in intensity as Cd decayed to Ag in a previous implantation experiment. An attempt was made to determine the origin of these lines by modelling them as a series of acceptor (donor) pair lines following the model developed by Eaves and Halliday for the KP lines in GaAs [10].

7.2 Experimental Details

^{7}Be which decays to ^{7}Li with a half-life of 53.2 days was implanted into single crystal ZnO. The implantation energy was 60 keV, while the dose was approximately 1×10^{12} cm^{-2}. As the half-life of the Be isotope was long, this sample was measured in DCU. The sample was annealed at 1073 K in 0.5 bar of O_2 in order to remove implantation damage. No signals which could be correlated with the concentration of ^{7}Be, or the daughter product ^{7}Li, were observed. As there was a delay between implantation at CERN and annealing the sample at DCU, and also as the sample was stored at room temperatures, out-diffusion of the implanted ions is a possibility for this experiment. However, the sample was still radioactive on arrival at DCU and over the measurement period of six months.

^{107}Cd was implanted with a dose of 5×10^{11} cm^{-2} into three samples from different suppliers over two beam runs. The ZnO crystals used were from Eagle-Pitcher, Rubicon and Cermet. This isotope decays via β^- decay to stable ^{107}Ag with a half-life of 6.5 hours. The samples were annealed in the same manner as the ^{7}Be-implanted samples. PL measurements were made over a number of half-lives, with the sample temperature kept below 77 K between measurements and a measurement temperature of 1.6 K.

7.3 Results

7.3.1 Damage-related emission lines in ^{107}Cd- and ^{7}Be-implanted samples

The damage-related emission lines are very closely spaced; between 3.337 and 3.351 eV, about twenty emission lines can be seen in the ^{107}Cd sample, while about eighteen can be seen in the ^{7}Be sample. Some of these lines are very weak and overlap with other lines, so this is a conservative estimate on the number of observed features.

Figure 7.1 shows a spectrum of these signals for both samples. The feature marked DD is the deep donor feature discussed in Chapter 3, while the α1 at 3.3367(4) eV feature is present in un-implanted samples, and has not, to my knowledge, been reported in the literature.

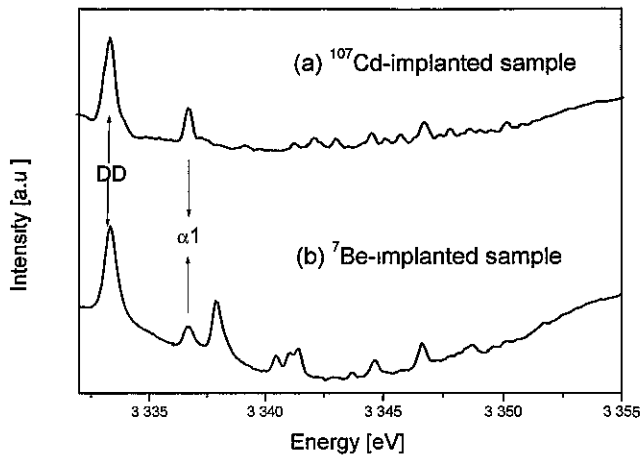

Figure 7.1: (a) Spectrum of ^{107}Cd-implanted sample, (b) spectrum of ^{7}Be-implanted sample.

The energy positions of these features are listed below in Table 7.2.

Be		Cd	
Energy Position (eV)		Energy Position (eV)	
3.3509	3.3433	3.3393	3.3475
3.3502	3.3424	3.3399	3.348
3.3497	3.3416	3.3415	3.3485
3.3489	3.3413	3.3423	3.3488
3.3487	3.3406	3.3432	3.3492
3.3483	3.3381	3.3444	3.3497
3.3479		3.3447	3.3501
3.3474		3.3453	3.3503
3.3469		3.3459	3.3510
3.3458		3.3462	3.3514
3.3449		3.3465	3.3516
3.3439		3.3469	3.3520

Table 7.2: Energy positions of damage related emission lines in Cd and Be-implanted samples

Figure 7.2 shows the two spectra on the same scale. As can be seen, several of these signals are apparent in the two spectra, with particularly good agreement on the high energy side. The slight energy shifts seen in this region could be due, perhaps, to slightly different levels of strain in the two samples. At the low energy side, there are a number of notable differences in the spectra, the most striking of which is the emission line at 3.3381(4) eV, apparent only in the ^{7}Be implanted sample, which is at least four times greater in intensity than any of the other signals.

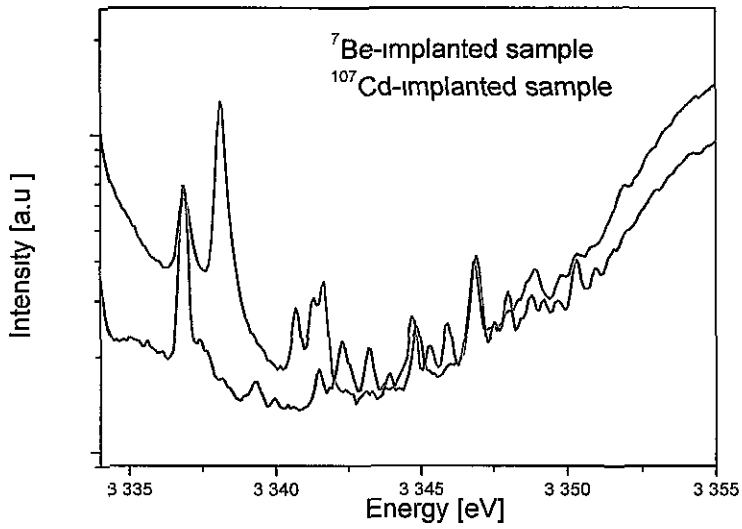

Figure 7.2: Spectra showing the PL spectrum for both implanted samples on the same intensity scale. As can be seen a number of the lines coincide in energy The most significant differences occur on the low energy side, with the most intense line at 3.3381 eV in the ^{7}Be-implanted sample

Figure 7.3 shows the spectra obtained over a temperature range 5.5 to 30 K. At temperatures greater than 15 K very little structure can be seen; the background light intensity also reduces substantially with increasing temperature. There appears to be a change in the relative intensities between some of the emission lines when the temperature is raised from 5.5 to 8 K, e.g. between α1 and the higher energy feature beside it, and also between the next three higher energy lines, marked by blue arrows; however, there does not appear to be any noticeable trend when these differences are examined in the other spectra.

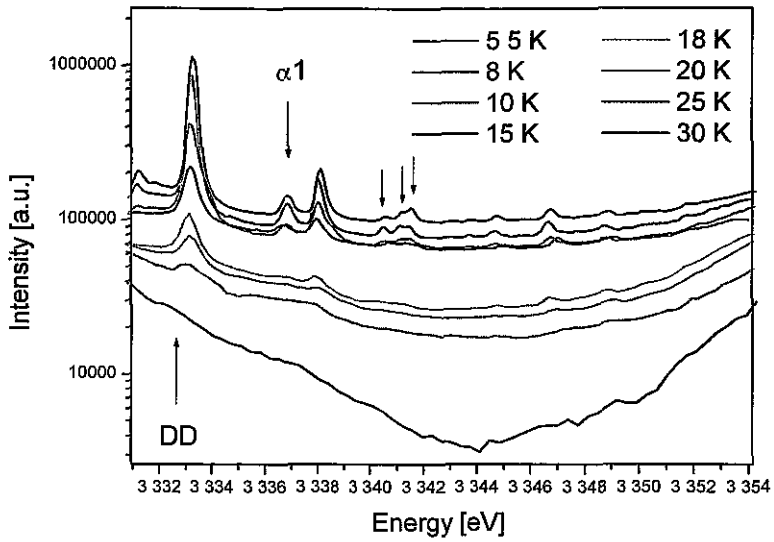

Figure 7.3: Spectra obtained as a function of temperature from 5.5 to 30 K

The possibility that these features were related to donor-acceptor pair lines was considered. However, for DAP spectra, one would expect to see a greater density of lines towards lower energy, as the difference between the Coulomb energies is proportional to the inverse separation between the donor and acceptor. This does not appear to be the case in the spectra presented here; the emission lines appear closer together at higher energy. In this way the spectra appear more similar to the KP lines in GaAs first reported by Künzel and Ploog [11], and later identified as recombination at pairs of acceptors [12]. Section 7.3.2 discusses a model developed by Eaves and Halliday [10] in fitting the observed energies of these features to an empirical model.

7.3.2 Acceptor (Donor) Pair model

Sharp closely spaced lines, known as the KP lines, are observed in MBE grown GaAs, and have been shown to be due to recombination at pairs of acceptors [12]. The lowest energy line was attributed to exciton recombination at a pair of neighbouring acceptors, while lines at higher energy are due to pairs that are further apart. This seems to follow the trend seen in the spectra presented in this work; the emission lines appear to be closer at the higher energy side. Figure 7.4 shows the spectrum presented in [10], with the notation as used therein. The data were scanned using the data digitizer Windig 2.5 [13].

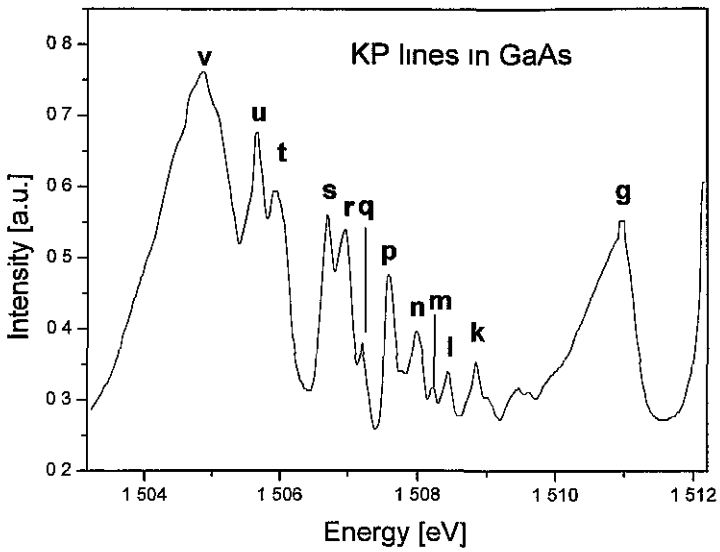

Figure 7.4. Spectrum from [10] of the KP lines

In comparison to the KP lines, the observed emission lines in ZnO are broader and further apart. As the interatomic separation in GaAs is less than in ZnO, 2.45 Å in GaAs in comparison to 3.249 Å (a-direction) and 5.204 Å (c-direction) in ZnO, it is possible that closer spaced emission lines should be observed in GaAs for this reason.

Eaves *et al.* observed that the peak positions of the KP lines could be correlated with the first number of pair separations for a type II spectrum as given by Wiley and Seman [14]. A type I spectrum involves defects occupying equivalent lattice sites, whereas for a type II spectrum the defect pair occupy inequivalent lattice sites. The feature, v, was attributed to next nearest pairs; u and t were attributed to pairs corresponding to the second shell; s, r, and q to the third radial shell, and g to an infinitely separated pair. The splitting of u, t and s, r, q was attributed to J-J interaction. They used an empirical model to derive the observed spectrum.

$$E(r) = E_{\text{inf}} - \alpha \exp^{-(r/a)^2} - \beta r^2 \exp^{-r/b} \qquad \textbf{7.1}$$

where E_∞ is the energy of the distant-pair peak, r is the pair separation and α, β, a and b are fitting values.

Later worked by Skolnick *et al.* [15] showed polarization differences in some of the KP lines, suggesting that the simple model used by Eaves and Halliday was not entirely correct; 47 separate emission lines were observed with the lowest energy emission lines, including v, u, t in Fig. 7.4, being polarised parallel to the (110) direction, while the higher energy lines, excluding g, being polarised parallel to the $(1\bar{1}0)$ direction. No polarisation behaviour was seen with g. Skolnick suggested that this behaviour was consistent with an acceptor pair model with the emission lines polarised parallel to the $(1\bar{1}0)$ direction related to acceptor pairs at increasing separation and line g related to an isolated acceptor. This polarisation behaviour also suggested a type I spectrum with the defects incorporated preferentially along the (110) axis. As the model developed by Eaves and Halliday [10] does not account for this preferential incorporation and considers a type II rather than a type I spectrum, it is unlikely to be of much use in describing the PL signals seen in this work. However, an interesting result is observed when the energies of the peak positions observed in this work are plotted against the pair separation as tabulated by Wiley and Seman [14] for materials which crystallise in the wurtzite structure. Figures 7.5-8 show the plots of the energy position of the damage-related emission lines observed in the PL spectrum of ^{7}Be and ^{107}Cd-implanted samples as a function of pair separation corresponding to a Type I and Type II pair spectra. All the data show a linear relationship, with slightly better fits obtained when a type I model is used for the Be data and a type II model for the Cd data. This could be simply a coincidence as this relationship is not observed in other materials where pair spectra are observed.

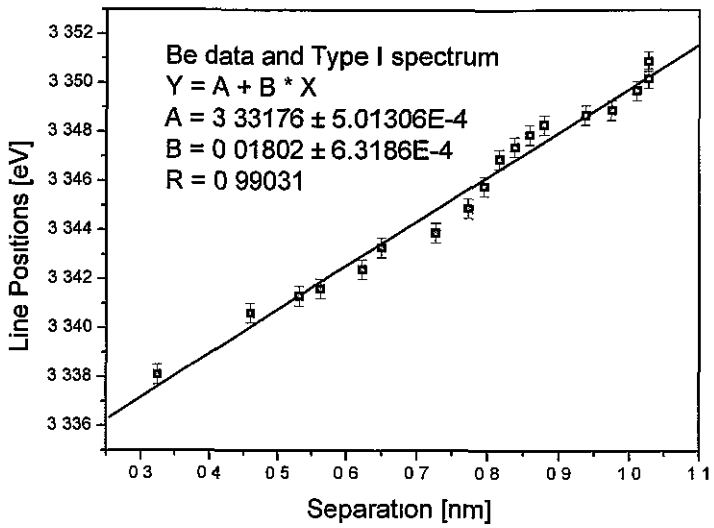

Figure 7.5: *Plot of energy position of damage-related emission lines observed in the PL spectrum of ^{7}Be-implanted ZnO as a function of pair separation corresponding to a Type I pair spectrum*

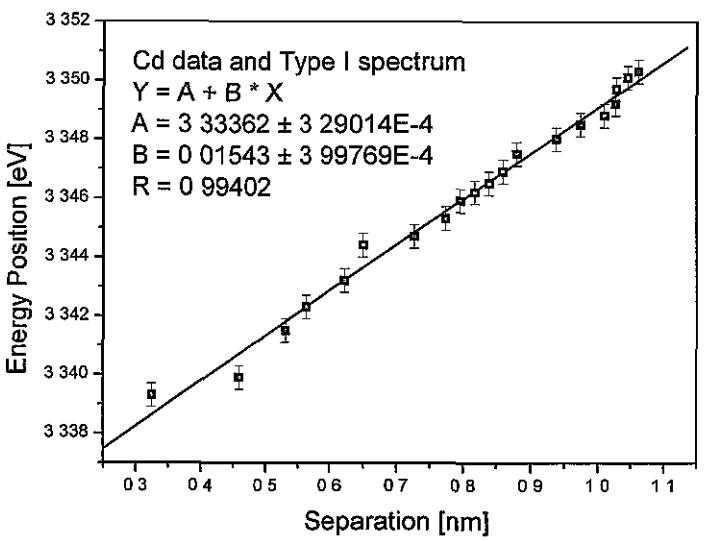

Figure 7.6: *Plot of energy position of damage-related emission lines observed in the PL spectrum of ^{107}Cd-implanted ZnO as a function of pair separation corresponding to a Type I pair spectrum*

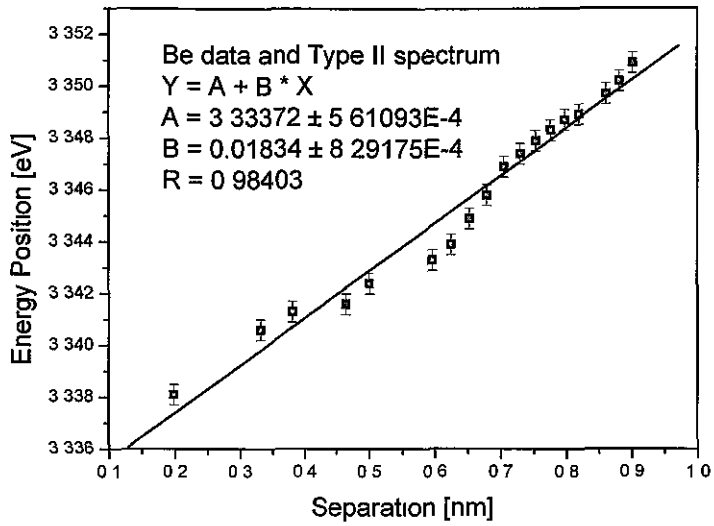

Figure 7.7: Plot of energy position of damage-related emission lines observed in the PL spectrum of ^{7}Be-implanted ZnO as a function of pair separation corresponding to a Type II pair spectrum

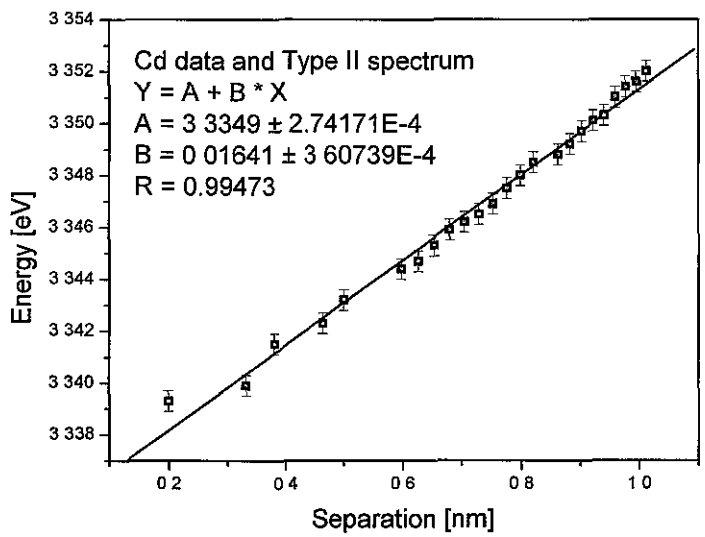

Figure 7.8: Plot of energy position of damage-related emission lines observed in the PL spectrum of ^{107}Cd-implanted ZnO as a function of pair separation corresponding to a Type II pair spectrum

Table 7.3 shows the radii used to calculate the pair separations, s^2 is from Wiley and Seman [14], the product of s and the lattice constant a gives the pair separations, R. A value of 3.249 Å is used for the lattice constant [16].

Type I				Type II			
s^2	R (nm)	s^2	R (nm)	s^2	R (nm)	s^2	R (nm)
1	0 325	7.333	0 880	0 375	0 199	5 708	0 776
2	0 459	8 333	0 938	1.042	0.332	6 042	0.799
2.667	0 531	9	0 975	1 375	0 381	6 375	0 820
3	0 563	9 667	1.010	2.042	0 464	7 04	0.862
3 667	0 622	10	1 027	2 375	0 501	7.375	0.882
4	0 650	10	1 027	3 375	0.597	7 708	0.902
5	0 726	10 333	1 044	3 708	0 626	8 042	0.921
5 667	0 773	10 667	1 061	4.042	0 653	8 375	0 940
6	0 796	11	1 078	4 375	0.680	8.708	0 959
6 333	0 818	11.333	1 094	4 708	0 705	9 042	0 977
6 667	0 839	11 667	1 110	5 042	0 730	9 375	0 995
7	0.860	12	1 125	5 375	0 753	9 708	1 012

Table 7.3: s^2 values as listed by Wiley and Seman, the pair separation is then calculated by multiplying s by the lattice constant a

7.4 Conclusions

More work is needed in order to clarify the nature of these features. The relatively low intensity of these features and their presence in only two samples is a barrier to many experiments. Annealing in different atmospheres should be undertaken to examine if the intensity increases. Further work with implantations with various atoms should confirm whether these features occur due to damage alone.

References

1. J. J. Hopfield, D. G. Thomas, R. T. Lynch, Phys. Rev. Lett., **17**, 312 (1966).
2. A. M. Stoneham, Theory of defects in solids: electronic structure of defects in insulators and semiconductors, (Oxford University Press, 2001, Oxford), Chapter 24.
3. Th. Agne, M. Dietrich, J. Hamann, S. Lany, H. Wolf, Th. Wichert, ISOLDE Collaboration, Appl. Phys. Lett., **82**, 3448 (2003).
4. M. J. Seong, I. Miothowski, A. K. Ramdas, Phys. Rev. B, **59**, 12911 (1999).
5. Lange's Handbook of Chemistry (15^{th} edition), edited by J. A. Dean (McGraw-Hill, 1999, London-New York); electronegativity values, Table 4.29; covalent radii values, Table 4.5.3.
6. Y. Kanai, Jap. J. Appl. Phys., **30**, 2021 (1999).
7. D. Zwingel, J. Lumin., **5**, 385 (1972).
8. U. Wahl, E. Rita, J. G. Correia, T. Agne, E. Alves, J. C. Soares, The ISOLDE Collaboration, Superlattices and Microstructures, **39**, 229 (2006).
9. D. G. Thomas, J. J. Hopfield, Phys. Rev., **150**, 680 (1966).
10. L. Eaves, D. P. Halliday, J. Phys. C: Solid State Phys., **17**, L705 (1984).
11. H. Künzel, K. Ploog, Appl. Phys. Lett., **37**, 416 (1980).
12. M. S. Skolnick, D. P. Halliday, C. W. Tu, Phys. Rev. B, **38**, 4165 (1988).
13. D. Lovy, Windig 5.5, http://www.unige.ch/sciences/chifi/cpb/windig.html, 21/08/06.
14. J. D. Wiley, J. A. Seman, The Bell System Technical Journal, **49**, 355 (1970).
15. M. S. Skolnick, T. D. Harris, C. W. Tu, T. M. Brennan, M. D. Sturge, Appl. Phys. Lett., **46**, 427 (1985).
16. H. Karzel, W. Potzel, M. Köfferlein, W. Schiessl, M. Steiner, U. Hiler, G. M. Kalvius, D. W. Mitchell, T. P. Das, P. Blaha, K. Schwarz, M. P. Pasternak, Phys. Rev. B, **53**, 11425 (1996).

Chapter 8: Conclusions and Further Work

8.1 Conclusions

In this thesis, radioactive isotope implantations were performed in order to investigate the effects that potential donors and acceptors have on the photoluminescence spectrum of ZnO. In Chapter 3, a signal related to a Ga donor was observed in the band-edge region in a ^{73}Ga-implanted sample; one due to a neutral donor, and one to an ionized donor. A signal at lower energy was found to correlate to the concentration of Ge, the daughter product. For the second implantation of ^{72}Zn, the neutral Ga related emission line was also found to follow the expected Ga-concentration in the sample, once the effects of isobaric contamination were accounted for. A broad red band, similar to a band seen previously in electron-irradiated ZnO, was found to increase in intensity. This was attributed to damage caused by the large recoil energy of ^{72}Ge, one of the decay products.

In Chapter 4, the effects of implantations of radioactive isotopes of Cu and Ni were studied, the emphasis being on their connection with the structured green band. The structured green band was found to increase in cases where the daughter product had a large recoil energy. As the magnitude of the recoil energy in all cases was sufficient to displace a Zn-atom but not enough to displace an O-atom, this structured green band was attributed to the creation of Zn-vacancies. Annealing studies further support this hypothesis, as a structured green band is observed after annealing in an O-atmosphere.

Chapter 5 concerned emission features in the near IR that have not, to my knowledge, been reported in the literature. The behaviour of these features as a function of temperature is discussed.

In Chapter 6 the results of a photoluminescence excitation experiment on these defects were reported. Due to Fe contamination in the sample, it was not possible to separate out the absorption energies feeding into the level related to the "new" defects and those affecting the Fe^{3+} emission. An attempt to resolve this was made

by performing PL measurements over an energy range 2.3-3.5 eV, and by subtracting the contribution of the Fe^{3+} phonon replicas from the PLE scans. From these measurements, it appears that excitation with light of phonon energy ranging in energy from 3.5 to ~3.25 eV leads to strong emission for these emission features.

Chapter 7 concerned a series of emission lines observed in ZnO implanted with ^{7}Be and ^{107}Cd. As these features remain constant in intensity as the concentration of the implanted isotope and the related daughter isotope vary in concentration, it is believed that these features are related to some form of implantation damage. Attempts were made to fit these emission lines to pairs of defects/impurities. A strong characteristic of these lines is that there is more structure at higher rather than lower energy and this favours defect pairs rather than DAP as the source of the lines.

8.2 Further Work

Regarding the Ga/Zn implantations, a series of Ge-implantations followed by electrical measurements would allow us to see whether Ge on a Zn-site acts as a double donor in ZnO. For the Cu/Ni results, further examination is needed to ensure that it is the structured green band that is affected by recoil damage, rather than some other underlying band. This could be resolved, if there is a sufficient difference in the life-times of the two bands, by performing either a time-resolved or phase-sensitive detection measurement. The relative ratios of the two bands could be determined after annealing and after a number of half-lives of the implanted species. The band exhibiting the greatest change could then be assigned to the creation of vacancies. Another difficulty with the assignment of the band to Zn-vacancies, rather than substitutional Cu, arises from the results presented by Dingle, where two ZPLs were observed with an intensity ratio equal to the natural abundance of two Cu isotopes. The possibility that these ZPLs were unrelated to the structured green band should be considered. In order to check this, measurements are planned to monitor the intensity of the ZPL region, with high resolution measurements, as well as the intensity of the structured band. This should allow the relationship between the ZPL and the broad band to be determined. For the series of emission lines observed in the near IR (the A_1 and L_1 features), Zeeman measurements might allow us to complete the details of the energy levels involved and thereby to identify the chemical nature

of these features. Material without Fe^{3+} contamination would enable the excited states of these defects to be examined more thoroughly. Photoluminescence studies of ZnO from Goodwill appear to show these emission lines as well as the Ni absorption lines, but not the Fe^{3+} signals. Zeeman measurements might also aid in identification of the damage-related emission features. Such measurements could determine whether these features are donor, acceptor or donor-acceptor pair in nature. Time resolved measurements could also provide such information.

Appendix A

The spectral features described in Chapter 5 showed a strong laser heating effect at low temperatures. This was believed to impact strongly on the ratio between the doublets L1/L2 and L3/L4. In order to compensate for these effects, spectra were taken at a number of laser excitation powers and the ratio between the doublets was plotted as a function of laser power. The dependence on this ratio was assumed to be a linear function of laser power and temperature, and the intercept of each plot was assumed to correspond to the ratio at zero laser power, with no sample heating. Each doublet was assumed to arise from transitions from two excited states to a common ground level and the model used was as described in Chapter 2. Shown below are the graphs used to generate the values for the Arrhenius plots.

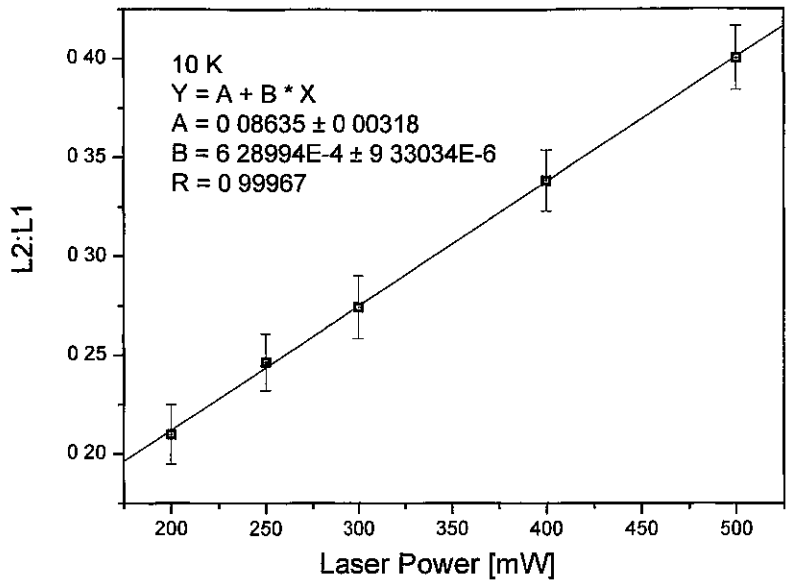

Figure A.1. Ratio between L2 and L1 as a function of laser power at 10 K

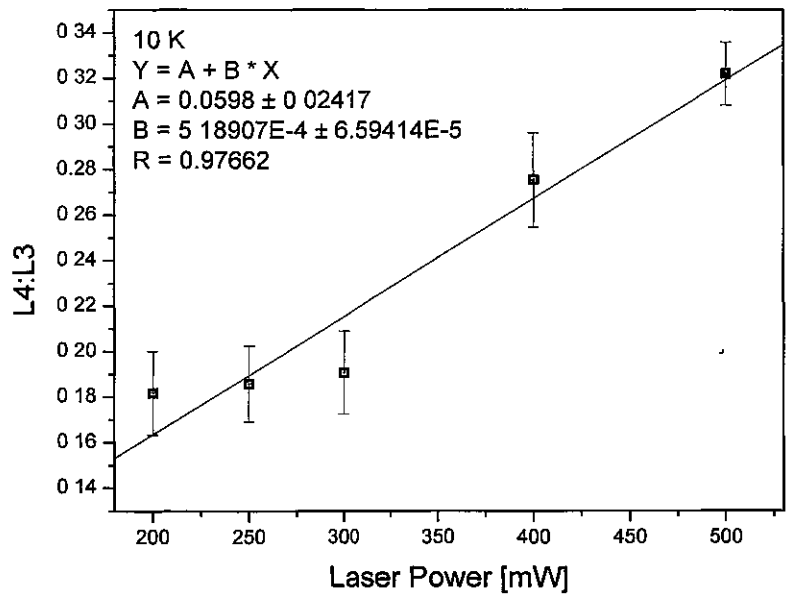

Figure A.2: Ratio between L4 and L3 as a function of laser power at 10 K

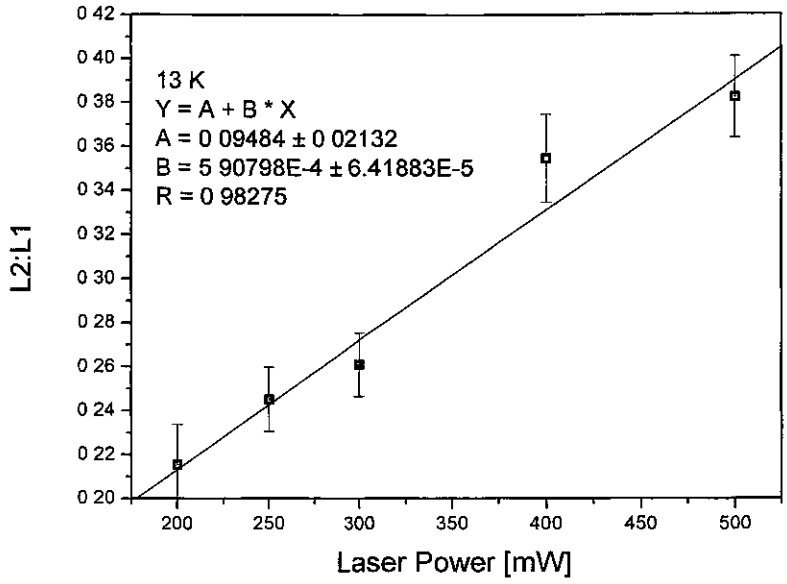

Figure A.3 Ratio between L2 and L1 as a function of laser power at 13 K

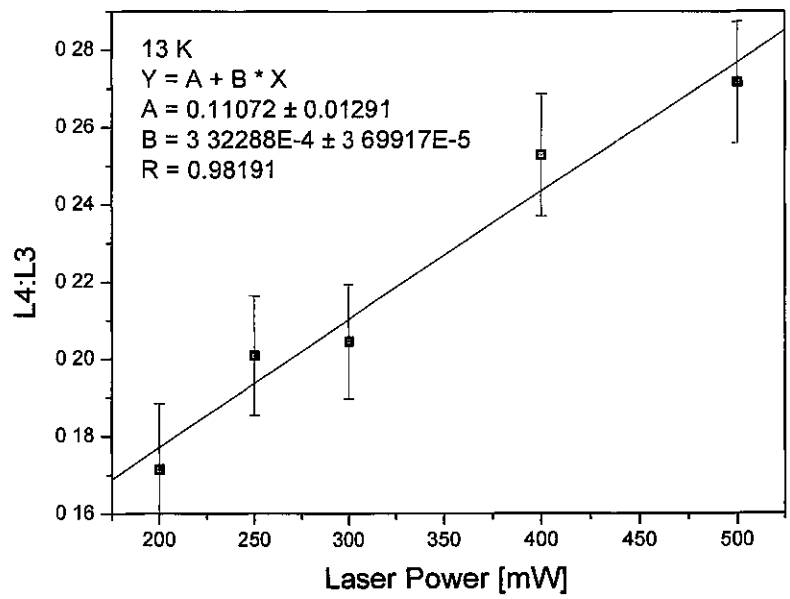

Figure A.4: Ratio between L4 and L3 as a function of laser power at 13 K

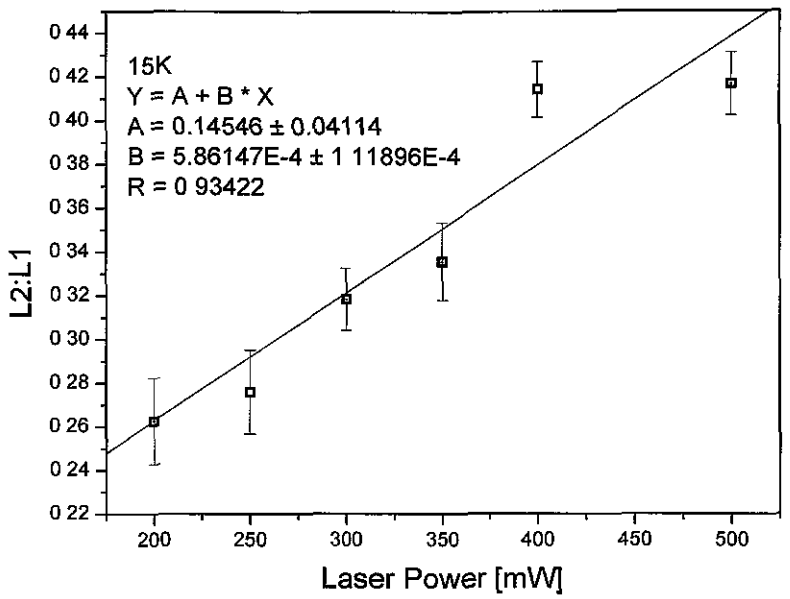

Figure A.5: Ratio between L2 and L1 as a function of laser power at 15 K

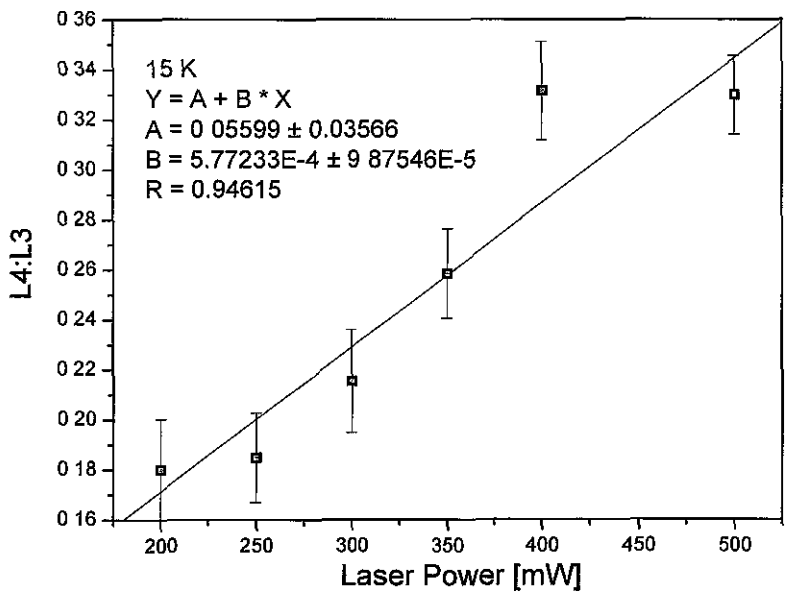

Figure A.6: Ratio between L4 and L3 as a function of laser power at 15 K

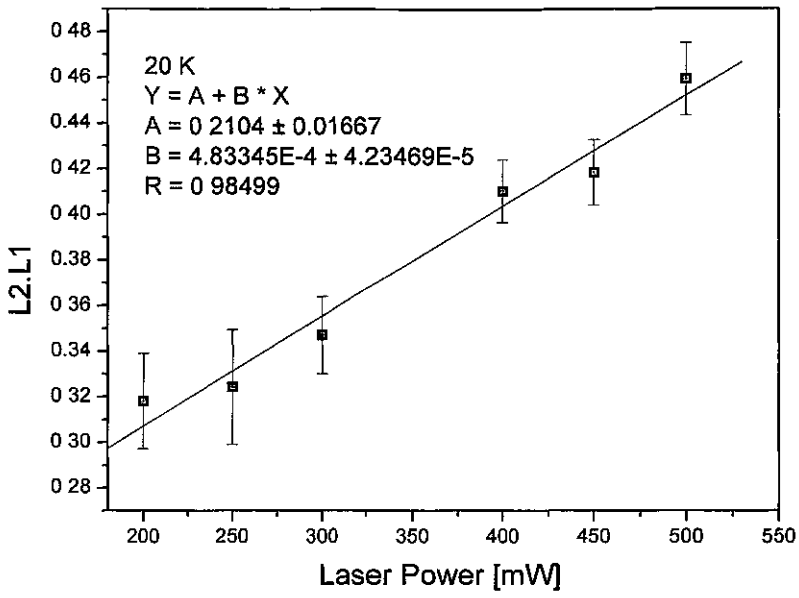

Figure A.7: Ratio between L2 and L1 as a function of laser power at 20 K

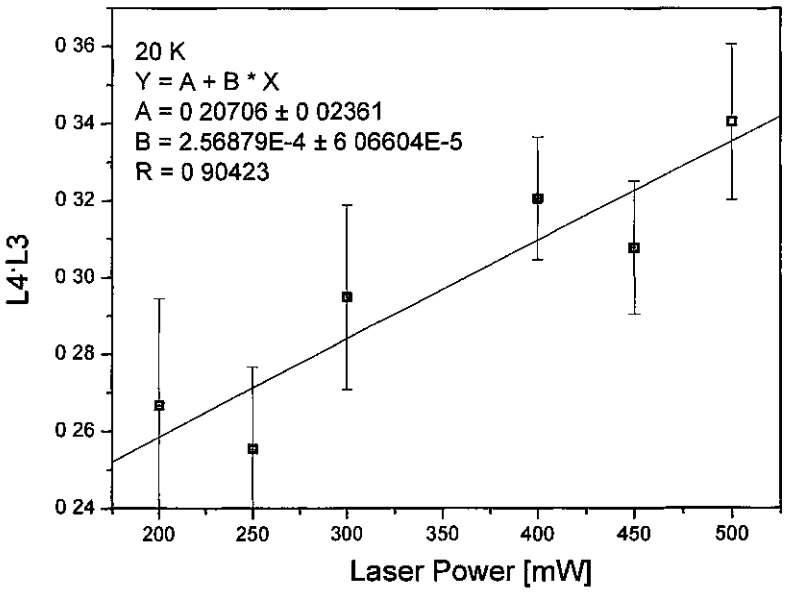

Figure A.8: Ratio between L4 and L3 as a function of laser power at 20 K

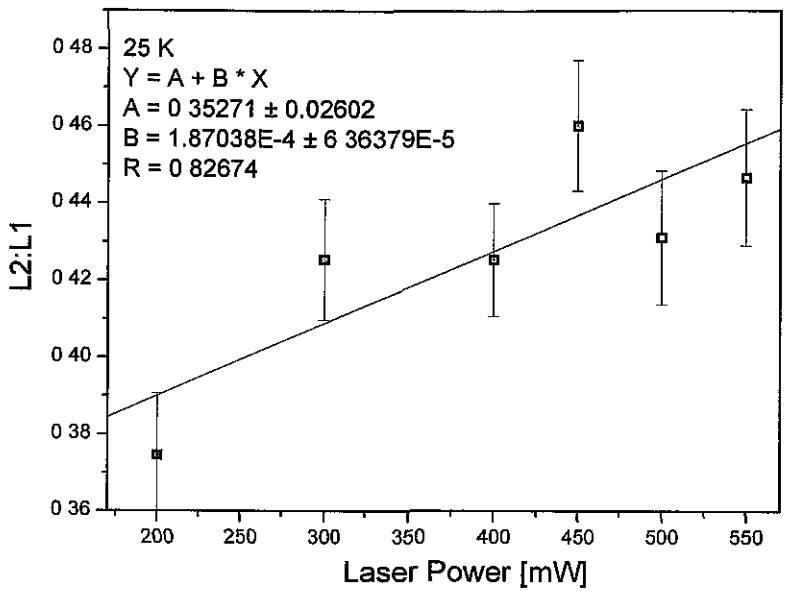

Figure A.9: Ratio between L2 and L1 as a function of laser power at 25 K

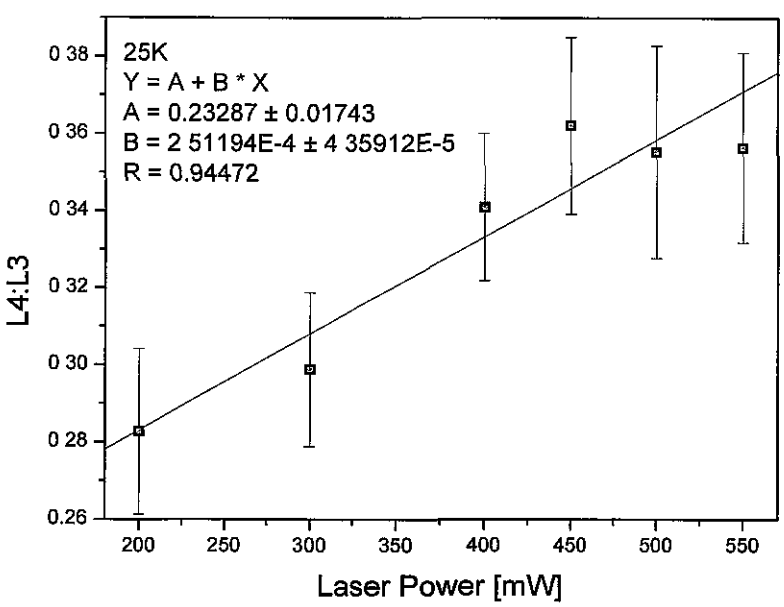

Figure A.10: Ratio between L4 and L3 as a function of laser power at 25 K

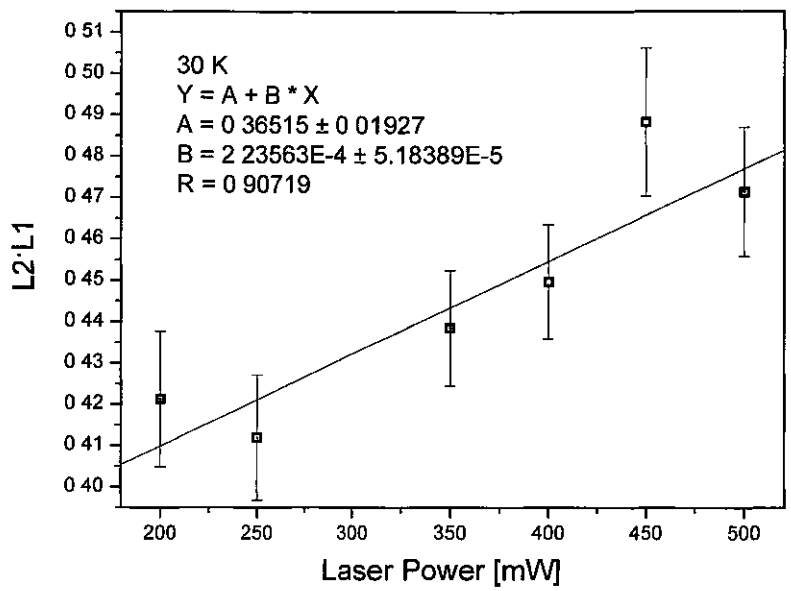

Figure A.11: Ratio between L2 and L1 as a function of laser power at 30 K

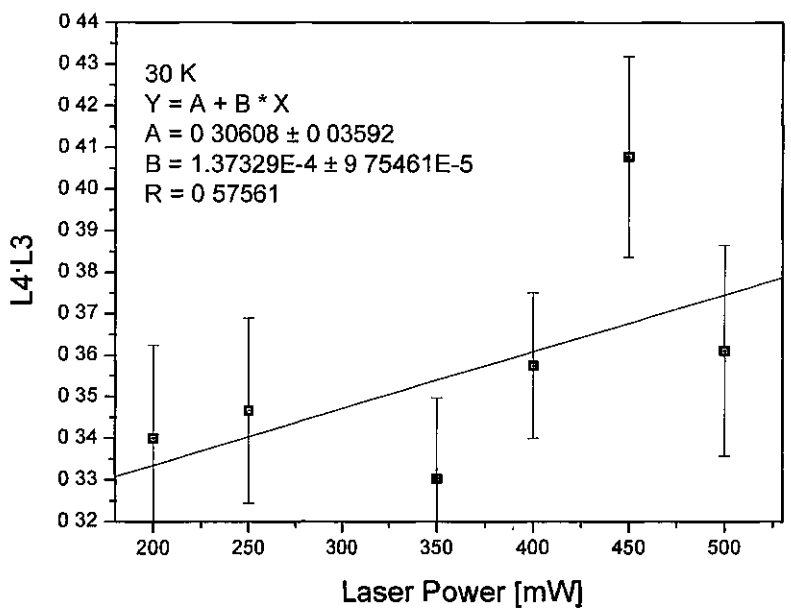

Figure A.12· Ratio between L4 and L3 as a function of laser power at 30 K

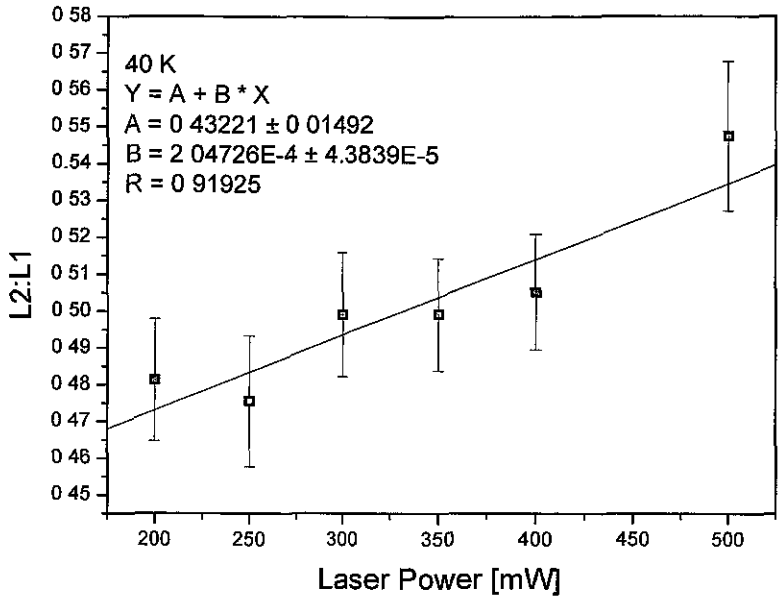

Figure A.13: Ratio between L2 and L1 as a function of laser power at 40 K

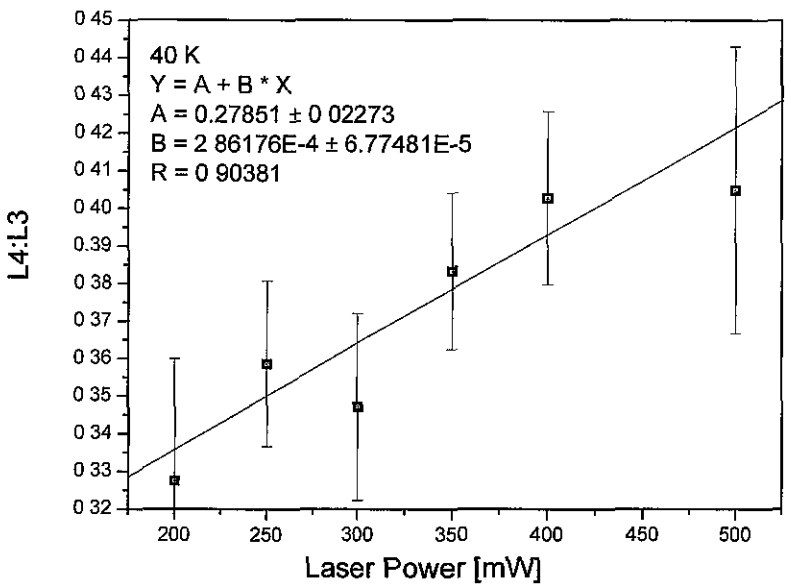

Figure A.14: Ratio between L4 and L3 as a function of laser power at 40 K

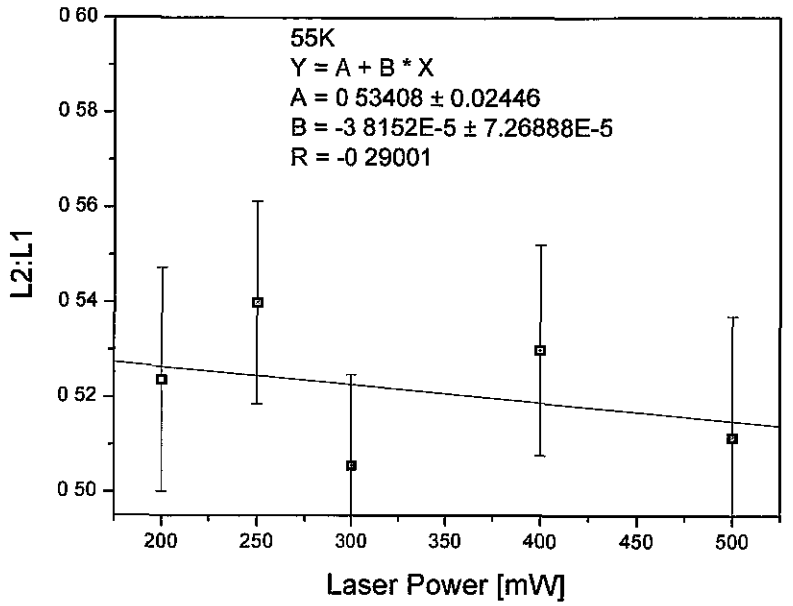

Figure A.15: Ratio between L2 and L1 as a function of laser power at 55K

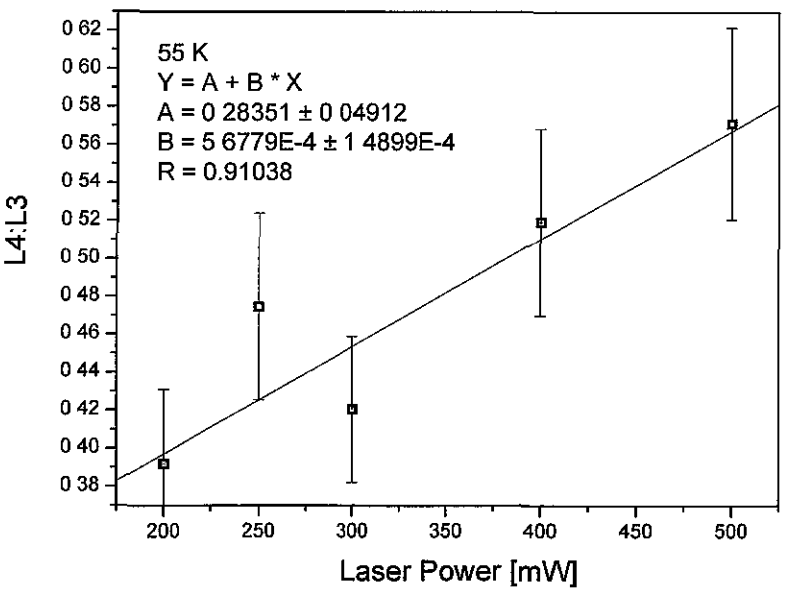

Figure A.16: Ratio between L4 and L3 as a function of laser power at 55K